UNIVERSITÀ DEGLI STUDI DI TRIESTE

UNIVERSITÀ DEGLI STUDI DI TRIESTE

DIPARTIMENTO DI FISICA

XXXVI CICLO DEL DOTTORATO DI RICERCA IN FISICA

Cavity Control of Phase Transitions and Nonlinearities in Quantum Materials

Settore scientifico-disciplinare: **FIS/03**

Dottoranda:
Shahla Yasmin Mathengattil

Coordinatore :
Prof. Francesco Longo

Supervisore:
Prof. Daniele Fausti

ANNO ACCADEMICO 2022/2023

ABSTRACT

The possibility of engineering the light-matter coupling with optical cavities has recently emerged as a new path to manipulate the collective properties of quantum materials. In this doctoral thesis, we explore the effect of light matter coupling inside a cavity on the complex materials $CuGeO_3$, 1T-TaS_2 and $SrTiO_3$ through terahertz spectroscopy. In order to exploit the light matter interaction in cavity confined system, we built a terahertz Fabry-Pérot resonator that can couple with low energy excitations and subsequently affect the collective behaviours in complex materials. The capability of the setup to tune the cavity fundamental mode at the cryogenic temperatures makes it highly versatile to study a wide range of quantum materials. Firstly, we will show the signatures of vibrational strong coupling in the normal phase of a spin-peierls compound $CuGeO_3$ and the charge density wave(CDW) material 1T-TaS_2 when embedded inside a resonant terahertz cavity. Observation of Rabi splitting indicates hybridization between material excitations and fundamental mode of the cavity in the strong coupling regime. Notably, for 1T-TaS_2, we reveal a multimode vibrational coupling scenario arising from the coupling between the fundamental cavity mode and multiple charge density wave phonon modes in the dielectric phase of the material. We will then investigate the first order metal-to-insulator phase transition of the CDW material 1T-TaS_2 inside a cavity. We unveil that the effective phase transition temperature can be controlled by tuning the cavity frequency and mirror alignment pointing to a scenario in which the cavity can filter the heat load on sample from the electromagnetic environment in a Purcell-like mechanism. Finally, we will discuss the cavity mediated nonlinear reponses in a paraelectric material $SrTiO_3$. The findings suggest that the nonlinearities likely associated with the soft phonon mode, are enhanced within the cavity's electromagnetic environment hence unveiling the potential to achieve the anharmonic regime of quantum materials without the need for intense lasers.

TABLE OF CONTENTS

1

INTRODUCTION

"Light and matter are both single entities, and the apparent duality arises in the limitations of our language"- Werner Heisenberg (on Quantum Mechanics, 1930). As Heisenberg observed, Albert Einstein's interpretation of photoelectric effect[1] and quantum theory of light have been groundbreaking in our understanding of light matter interactions. The discovery that light is quantized into discrete packets of energy called photons fundamentally changed our understanding of electromagnetic radiation and established the foundation of quantum mechanics. Quantum mechanics have been successful in explaining chemistry and various properties of materials. However, Maxwell's theory of electricity and magnetism required significant modifications according to the fundamentals of quantum mechanics in order to understand light matter interaction. So, quantum electrodynamics(QED) has been formulated by physicists like Feynman in 1929 providing a comprehensive framework for explaining interaction between light and matter.

Quantum electrodynamics(QED) is the theory of electromagnetic interaction of photons and charged particles. QED has been called "the jewel of physics" because the theory has been extremely accurate in predicting the anomalous magnetic moment of the electron, and the Lamb shift of the energy levels of hydrogen[2, 3]. The QED theory could explain wide range of phenomena, from scattering to absorption and emission of light by atoms surviving more experimental scrutiny than any other physical theory[4]. Overtime, it has developed as a basis of all other field theories, which together with general relativity form the fundamental core of contemporary physics. The ordinary QED can be extended to more complex and controlled environments, giving rise to the field of cavity QED(cQED).

In the early times, spontaneous transitions seemed uncontrollable and irreversible, much like the emission of photons in to far-field by an excited atom. However, recent advances in the field have made it possible to control the rate of these transitions or even reverse them entirely. This has been achieved by placing an atom in a small box with reflecting walls constraining the wavelength of photons that can be emitted or absorbed. This idea is the basis of Cavity Quantum Electrodynamics(cQED). In quantum optics, cavity refers to a resonator for electromagnetic radiation. So, the boundary conditions imposed by the cavity in the local environment influences the spatial and spectral properties of the electromagnetic field and hence the atom field interaction significantly.

The history of cQED dates back to 1940s, when Edward M. Purcell reported the changes in the spontaneous emission rate of nuclear magnetic transitions at radio frequency for a spin system coupled to a resonant electrical circuit[5]. He showed that the rate of spontaneous emission is enhanced by a factor of $3Q\lambda^3/4\pi^2V$, where Q is the quality factor, λ is the wavelength and V is the volume of the resonator. This enhancement, known as the Purcell effect, originates from the modification of the local density of states (LDOS) available for the radiated photon by the resonant circuit, compared to the LDOS in free space. The same principle applies to an atom inside an optical cavity, where the cavity modifies the photonic environment, thereby altering the emission characteristics of the atom. This specific scenario falls within what is known as the weak-coupling regime. Within this regime, both spontaneous emission enhancement[6] and inhibition[7] for an atom in a cavity was experimentally demonstrated.

However, cavity QED experiments have now evolved in to higher and higher atom-cavity coupling placing them in the regime of 'strong coupling'. In this regime, light matter interaction is characterised by periodic exchange of energy between the atom and the enclosing cavity. The strong light matter interaction has been first reported for a single Rydberg atom in a microwave cavity[8]. Since then, several experiments have been published in which the strong coupling between atom and a single cavity mode is exploited[9–13]. In order to achieve strong light matter coupling regime, the coherent interaction between the light and matter has to overwhelm the incoherent dissipative processes. So, the system must combine large coupling with longer lifetimes for both material excitation and cavity. This ensures that the emitted photon remains trapped inside the cavity to be reabsorbed again by the material. Hence, the spontaneous emission is a reversible process in the strong coupling regime. When an excitation in the material is coupled to a resonant cavity mode it undergoes Rabi oscillations which is a result of back and forth energy exchange between the cavity and the material excitation at a well defined frequency (the Rabi frequency). The light matter interaction in a strongly coupled system is significant enough to result in the phenomena called Rabi splitting, where new light matter hybrid states called polaritons are formed.

Strong light matter coupling has been widely demonstrated in chemical systems like isolated atomic and molecular systems[11, 9, 14–16] and the studies have been recently extended also to organic and inorganic semiconductor excitons[17–19], phonons[20–27], or magnons[28]. In addition to this, recent years have seen efforts focused on exploiting these strong light-matter interactions to alter the material properties by embedding materials into cavities. Confining light in to smaller volume using optical cavities enhances light matter coupling resulting in new states where quantum fluctuations of light and matter modify the material properties. In this approach, new phases can be achieved in materials in its ground state without driving the system out of equilibrium using intense lasers.

Numerous theoretical proposals and experimental demonstrations have been reported on the cavity control of collective phenomena in quantum materials. The theoretical frameworks propose enhanced superconductivity through cavity-mediated electron pairing[29–34], cavity control of the competing order between charge density wave and superconducting phases[35], cavity control of excitons[36], enhanced ferroelectricity[37–40], and cavity control of magnetic order[41]. Experimental demonstrations have reported that coupling with the cavity can change the magneto transport in two dimensional materials[42],

suppress the topological protection of the integer quantum Hall effect[43], or even modify the critical temperatures and the magnetic order in conventional and unconventional superconductors[44, 45].

Outline of the Thesis

The goal of this thesis is to transform some of the previously mentioned theoretical frameworks to an efficient experimental tool for tailoring material properties through light matter interaction. The research aims to uncover new dimensions in the behavior of quantum materials under the influence of confined electromagnetic fields, potentially leading to novel functionalities and applications.

To explore light matter interaction, a specially developed tunable cryogenic cavity and terahertz spectroscopy were employed. The built cavity assembly has been proven to be efficient in tuning the cavity resonance, at cryogenic temperatures enabling targeting the excitations in the materials we want to couple with. Terahertz spectroscopy provides an efficient mean to probe the dynamic responses of the light matter hybrid system.

The structure of this thesis is as follows:

- Chapter 2 provides a comprehensive overview of the theoretical foundations and experimental techniques related to light-matter interactions in optical cavities. It covers basic principles of the Fabry-Perot optical cavities and a general framework of the weak-coupling regime(Purcell effect) and the strong-coupling regime.
- Chapter 3 has been focused on giving a general introduction to ferroelectricity and the soft mode dynamics across the ferroelectric phase transition. The chapter also gives a detailed explanation on the mechanism behind the quantum paraelectric state in incipient ferroelectrics like $SrTiO_3$ and the research frameworks that has reported induced ferroelectricity in $SrTiO_3$ using subtle external perturbations. The purpose of this chapter is to offer an insight into the significance of the soft mode in driving the ferroelectric state and its role in the nonlinear responses of $SrTiO_3$, which are reported in the chapter 7 of this thesis.
- Chapter 4 is dedicated to providing a detailed description and characterization of the experimental setups that has been employed in this thesis. These setups include a tunable cryogenic terahertz cavity, a broadband terahertz time-domain spectrometer for the characterization of light-matter hybrids, and a nonlinear terahertz spectrometer to study the nonlinear responses.
- Chapter 5 presents the experimental findings of strong light-matter coupling in $CuGeO_3$ and charge density wave(CDW) material 1T-TaS_2. In the first section, We demonstrate vibrational strong coupling in a $CuGeO_3$ sample at low temperatures providing the evolution of the strong coupling features in the terahertz pulses. In addition, the thermal evolution of the vibro-polaritons have been also mapped. The second section focuses on examining the multimode vibrational coupling within the dielectric phase of charge density wave(CDW) material 1T-TaS_2 resulting from the cavity mediated hybridization of CDW phonons in the material. The evolution of the

multimode polaritons across the insulator to metal transition has been tracked to map the influence of free carriers on the splitting between polaritons.

- Chapter 6 provides experimental evidences for the impact of cavity electrodynamics on the first order metal insulator phase transition in CDW material 1T-TaS_2. We will show that the effective critical temperature of the metal to insulator phase transition can be controlled by changing the resonant frequency of the cavity and the alignment of the cavity mirrors. We highlight that the reversible control of metal-to-insulator phase transition can be achieved in 1T-TaS_2 by tuning the fundamental mode of the cavity at a fixed temperature. We propose two scenarios to elucidate the cavity-mediated effect. The first scenario is derived from the renormalization in the free energy of the metallic phase, while the second scenario explores the possibility of cavity mediated change in the actual temperature of the sample.

- Chapter 7 focuses on investigating the nonlinear responses of $SrTiO_3$ inside an optical cavity. The studies show a nonlinear absorption-like feature is enhanced when the sample is embedded inside an optical cavity. The thermal evolution of the spectral features implies that the nonlinearity can be possibly linked to the anharmonicity of the soft phonon mode. The findings highlight that the effect can be attributed either to cavity induced field enhancement of resonant frequencies or to the modification of anharmonic soft mode potential by the vacuum fluctuations inside the cavity, facilitating the emergence of nonlinearity even at lower field strengths.

2

Light Matter Interaction in Optical Cavities

Cavity quantum electrodynamics is based on the interaction between the matter and confined modes of the electromagnetic field which can be realized within the optical cavities[46, 47]. Optical cavities confine light spatially and temporally and this creates quantized field as a set of harmonic oscillators[48]. In the simplest configuration, a cavity can be understood with a set of boundary conditions that reflect light back and forth, whose density of states is different with respect to the one in free space, leading to an enhanced light-matter interaction with respect to the one observed in vacuum.

In this chapter, we present the characteristics of the optical cavities, specifically focusing on the case of co-planar Fabry-Perot optical cavities which are the one employed in the work presented in this thesis. After a brief introduction on the Fabry-Perot resonator, we give a theoretical description on weak and strong coupling regime of light matter interaction inside optical cavity.

2.1 Fabry-Perot Optical Cavities

The simplest form of optical cavity refered as Fabry Perot cavity contains an arrangement of two plane mirrors facing one another forming a standing electromagnetic wave inside the resonator[48–50]. The plane mirrors are arranged parallel to each other so that light bounces back and forth between the mirrors, thereby forming a standing wave. If the light entering through one of the partially transmissive mirror is in resonance with the cavity, it combines constructively after each round trip and hence gives maximum transmission at the output of the cavity. In resonance conditions, (assuming there is no light penetration in to the cavity mirrors) the cavity length can be written as the integer multiple of half wavelengths as,

$$L_{cav} = m\left(\frac{\lambda}{2n}\right) \tag{2.1}$$

where, λ is the wavelength of the light, n is the refractive index of the material inside the cavity and m is the integer. The standing waves which can be realized within a Fabry-Perot resonators are depicted in Figure 2.1 for different multiples of the mode index m.

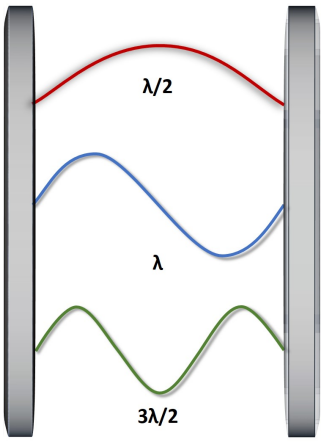

Fig. 2.1 **Standing Waves in a Fabry Perot Cavity.** a) Structure of a Fabry–Perot cavity. The cavity length is equal to an integer number of intracavity half wavelengths (λ/2)

The optical cavity employed in this thesis doesn't have perfect boundaries, so the energy of the confined electromagnetic field leak in to the environment. This results in the cavity modes to decay in time. The trapping efficieny or the dissipation of the cavity (through absorption, scattering or leakage through the mirrors) is quantified using quality factor(Q)[51]:

$$Q = \frac{\omega_c}{\Delta\omega_c} \tag{2.2}$$

where ω_c and $\Delta\omega_c$ are the frequency and the linewidth(full width of half maximum((FWHM)) of the fundamental cavity mode. The quality factor of the cavity can be improved by increasing the reflectivity of the cavity mirrors. However, the most widely used Fabry Perot cavities based on metallic mirrors have a very low quality factor(10-100), which is limited by the intrinsic reflectivity of the metals and by large mode volumes[49]. Very high Q values($\sim 10^{11}$) can be achieved by using super-mirrors with extremely low losses[52]. In addition, silica microspheres with whispering gallery resonator modes have been reported to be exhibiting quality factors around 10^{10}[53, 54].

For a plane wave incident on the input mirror of the cavity, the reflected and transmitted field can be written in terms of mirror reflectivity(R) as,

$$\frac{E_{ref}}{E_{inc}} = -\sqrt{R} \tag{2.3}$$

$$\frac{E_{trans}}{E_{inc}} = \sqrt{1-R} \tag{2.4}$$

The incident field, E_{inc} can be written as a plane wave, $E_{inc} = E_0 e^{-i\omega t}$. For the wavelength λ, the input field propagating through the cavity from the input mirror to the end mirror will acquire a phase component $\delta_0 = \frac{2\pi n L_{cav}}{\lambda}$, where we have denoted with L_{cav} the cavity length and with n the refractive index of the medium within the resonator. Assuming that

the reflecting surfaces of both the mirrors are identical, the field after the second mirror, i.e. the first transmitted field of the cavity can be expressed as,

$$E_1 = (1-R)E_0 e^{-i(\omega t - \delta_0)} \tag{2.5}$$

where, $\kappa = 2\pi n/\lambda$.

If a wave is reflected twice inside the cavity before being transmitted its amplitude can be written as,

$$E_2 = (1-R)RE_0 e^{-i(\omega t - \delta_0)} e^{i2\delta} \tag{2.6}$$

2δ is the phase shift accumulated due to the round trip inside the cavity. We can take similar consideration for the other waves that are reflected multiple times inside the cavity. Considering that number of transmitted waves contributing to the total transmitted field to be infinitely large the total transmitted field of the cavity can be calculated by using an infinite geometric series,

$$\begin{aligned} E_T &= E_1 + E_2 + E_3 + ... \\ &= E_0(1-R)e^{-i(\omega t - \delta_0)}(1 + Re^{i2\delta_0} + R^2 e^{i4\delta + ...}) \\ &= E_0 \frac{(1-R)e^{-i(\omega t - \delta_0)}}{1 - Re^{i2\delta}} \end{aligned} \tag{2.7}$$

From the above formula, the transmitted intensity can be written in terms of incident intensity.

$$\begin{aligned} I_T &= I_0 \frac{(1-R)^2}{1 + R^2 - 2R\cos 2\delta} \\ &= I_0 \frac{(1-R)^2}{1 + R^2 - 2R + 2R(1 - \cos 2\delta)} \\ &= I_0 \frac{(1-R)^2}{(1-R)^2 + 4R\sin^2 \delta} \\ &= \frac{I_0}{1 + F\sin^2 \delta} \end{aligned} \tag{2.8}$$

where $F = \frac{4R}{(1-R)^2}$ is called coefficient of finesse[51] and for normal incidence $\delta = \frac{2\pi n L_{cav}}{\lambda}$.

From this, we realize that the transmitted intensity is a periodic function of δ and maximum intensity I_0 is achieved when $\delta = p\pi$, p is an integer. Hence, the Fabry Perot transmission is modulated along the wavelength according to this condition. Figure 2.2 shows the transmitted intensity as a function of δ. The peaks correspond to the resonances of the cavity.

2.1.1 Parameters of a Fabry Perot Cavity

Free Spectral Range

As we mentioned before, the cavity resonates when the length of the cavity is an integer number of half wavelengths. The resonance frequency of the cavity can be expressed in terms of cavity length as[50, 51],

$$f_c = \frac{nc}{2L_{cav}} \tag{2.9}$$

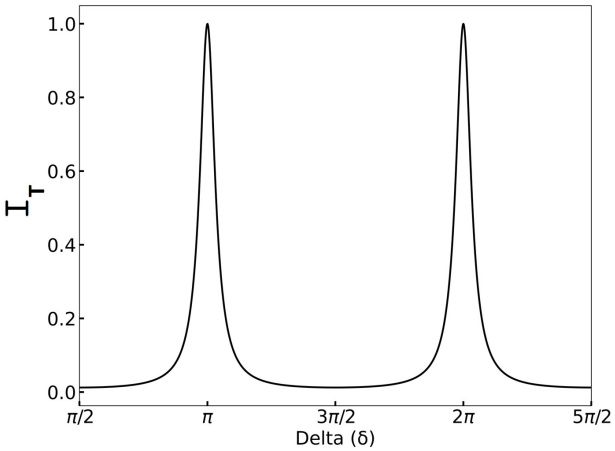

Fig. 2.2 **Transmission of a Fabry Perot Cavity** a) Transmission intensity of the cavity as a function of phase, δ

Figure 2.3 shows the transmitted intensity as a function of frequency and the peaks are associated to the resonances of the cavity. The difference between adjascent resonances are called Free Spectral Range(FSR)(Figure 2.3).

$$FSR = f_c(n+1) - f_c(n) = C/2L \tag{2.10}$$

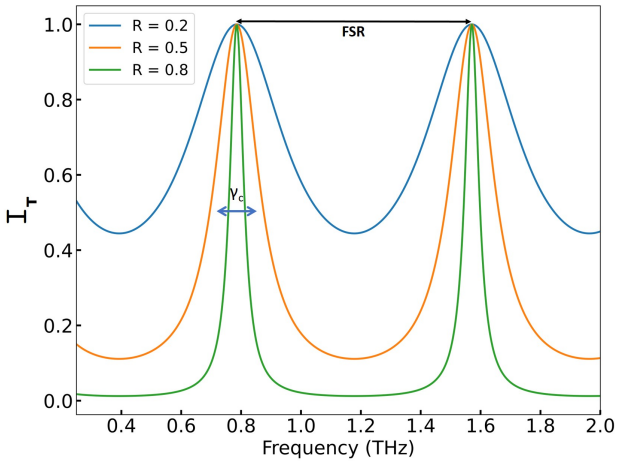

Fig. 2.3 **Fabry Perot Parameters.** a) Transmission intensity of the cavity as a function of frequency for different mirror reflectivities. Free spectral range(FSR) is a measure of sharpness of the transmission peaks.

Finesse

Finesse is related to the number of round trip a photon make before decaying inside the cavity through scattering, absorption or transmission through the mirror. Finesse of the

cavity is defined as[50, 51],

$$\mathcal{F} = \frac{FSR}{\gamma_c} = \frac{\pi}{\delta_c} \tag{2.11}$$

where γ_c and δ_c are the linewidth of the resonance peak in terms of frequency and phase shift respectively. γ_c can be calculated from the full width half maximum of the resonance peak, FWHM. The γ_c can be obtained by substituting in to Equation 2.8 for a transmitted intensity which is half of the peak value,

$$\frac{1}{2}I_0 = \frac{I_0}{1 + F\sin^2(\frac{1}{2}\delta_c)} \tag{2.12}$$

Since $\delta_c << \pi$, we can use the approximation $\sin(\frac{1}{2}\delta_c) \approx \frac{1}{2}\delta_c$ to obtain,

$$\delta_c = \frac{2}{\sqrt{F}} = \frac{(1-R)}{\sqrt{R}} \tag{2.13}$$

and Finesse,

$$\mathcal{F} = \frac{\pi}{\delta_c} = \frac{\pi\sqrt{R}}{1-R} \tag{2.14}$$

Figure 2.3 shows the transmitted intensity at different mirror reflectivities. It can be noted that the linewidth of the modes reduces with an increase in the mirror reflectivity. Large Finesse also means that the transmission peaks are well-isolated and the light incident on cavity close to one resonance frequency interacts with only one cavity mode.

Quality Factor

The optical field stored within the resonator decays over time. The shape of the decay, as for any underdamped harmonic oscillator, is a decaying exponential with time constant $1/\gamma_c$[50, 51]. For an optical cavity of resonance frequency, ω_c Fourier transform of the cavity Lorentzian can be written as,

$$E(t) \propto \cos(\omega_c t) e^{-\frac{\gamma_c}{2}t} \tag{2.15}$$

and optical period, $T = 2\pi/\omega_c$. Energy, $|E|^2$ will be:

$$|E(t)|^2 \propto (e^{-(\gamma_c/2)t})^2 = e^{-\gamma_c t} \tag{2.16}$$

and the energy density decay over time:

$$-\frac{d}{dt}|E(t)|^2 \propto \gamma_c e^{-\gamma_c t} \tag{2.17}$$

Qulity factor(Q) of a cavity is the number of optical cycles (x 2π) before the stored energy decays to $1/e$ of original value. So, the quality factor can be written as the ratio of energy stored and energy lost per cycle.

$$Q = 2\pi \frac{|E(t)|^2}{-\frac{d}{dt}|E(t)|^2 \cdot T} = \frac{2\pi}{\gamma_c \cdot T} = \frac{\omega_c}{\gamma_c} \tag{2.18}$$

The Finesse and the Quality factor are related by,

$$\frac{\mathcal{F}}{Q} = \frac{FSR}{\omega_c} \tag{2.19}$$

It can be noted that, if one changes the resonant frequency of the cavity(resonator's round-trip length) while keeping the losses per round trip constant, the Finesse stays constant, while the Q factor increases. The latter reflects that it will take more time for the optical field to decay.

2.2 Weak-Coupling Regime: Purcell Effect

The light and matter has been treated as different entities and were described by their own properties before the development of quantum mechanics. Since the onset of quantum physics, spontaneous emission, which has been regarded as a fundamental property of the matter has emerged as a property of emitter-vacuum system rather than of an isolated emitter[55]. The modification of the density of states by placing the radiating atom near a metallic structure has been first predicted by Edward Purcell[5, 56]. Therefore, the emission rate of the matter can be enhanced or suppressed by its surrounding electromagnetic environment due to the so called Purcell effect for example, by placing the emitter in a cavity.

2.2.1 Emission in Freespace

Spontaneous emission of an emitter with two electronic level can be referred as a jump of the electron from an excited state to ground state accompanied by the emission of a photon. This process can be associated to the coupling between the emitter and the electromagnetic field. The radiation field can be described as an infinite set of harmonic oscillators with a ground state of zero point energy, $\hbar\omega/2$ associated to the quantum fluctuations[57]. The vacuum electric field can be defined as[55],

$$E_{vac} = \sqrt{\frac{\hbar\omega}{2\epsilon_0 V}} \tag{2.20}$$

where, ϵ_0 is the permittivity of free space, V is the size of an arbitrary quantization volume and ω is the mode frequency. The coupling between the emitter and the field is quantified using rate of energy exchange between emitter and the field, referred to as Rabi frequency of the vacuum, Ω_{vac}[55]:

$$\Omega_{vac} = \vec{D} \cdot \vec{E}_{vac}/\hbar \tag{2.21}$$

here, D is the matrix element of the electric dipole of the emitter between the two levels. The scalar product confirms the importance of relative orientation between the dipole moment and the electric field[58, 59]. The mode density($\rho_{vac}(\omega)$), defined as the no of modes per unit frequency interval can be calculated by the expression $\rho_{vac}(\omega) = \omega^2 V/\pi^2 c^3$. The

probability of photon emission per unit time(τ_{vac}) is given by Fermi's "golden rule"[55, 5]:

$$\tau_{vac} = 2\pi\Omega_{vac}^2 \frac{\rho_{vac}(\omega)}{3} = \frac{\omega^3}{3\pi\hbar c^3} \frac{|D|^2}{\epsilon_0} \tag{2.22}$$

In the free space, emitter can radiate into any mode that satisfies the conservation of energy and momentum. So, the exponential decay of the emitter is an irreversible process due to the continuum of field modes resonantly coupled to the emitter.

2.2.2 Resonant Cavity Emission

The mode structure of the vacuum field is significantly modified inside a cavity. If an emitter is embedded at the center of an optical cavity resonant with the photon energy the emission rate will be enhanced compared to the one of free space. Because, since the cavity has finite volume, the allowed standing wave patterns are spatially confined, increasing effectively the density of states. If the cavity is off-resonant the set of states associated with it will not be relevant for the emitter resulting in an inhibited emission[7]. Hence, resonant cavity acts as a spectral filter and leads to an increase in the local density of photonic states at the emitter's position, thereby enhancing the emission rate[60]. Figure 2.4 shows the spontaneous emission dynamics of InGaAs quantum dots (QDs) in a photonic-crystal nanocavity. The QDs exhibit faster decay in a resonant cavity (which enhances the density of states that the QDs can decay to) and more slowly in an off- resonant cavity (which shields the QD from the environment)[61, 15].

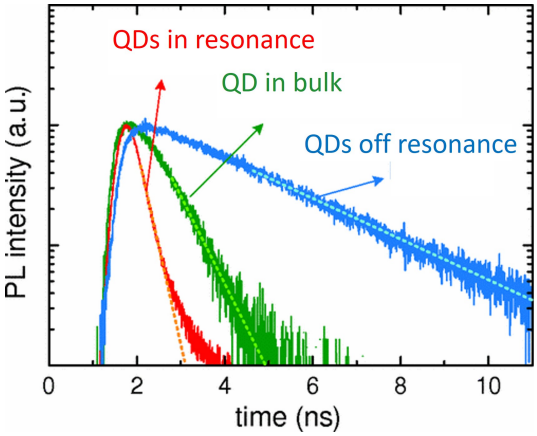

Fig. 2.4 **Purcell effect in quantum dots (QDs) embedded inside a photonic-crystal nanocavity.** a) Time- resolved micro- photoluminescence intensities of InGaAs QDs on resonance with the cavity, off resonance and in bulk without any cavity.[61, 15]

The behaviour of an emitter inside cavity is determined by the ratio of Rabi frequency of the emitter in vacuum to the linewidth of the cavity($\Delta\omega_c$). The cavity linewidth is essentially the density of modes "seen" by the emitter in the cavity or inverse of the lifetime of a photon in the cavity. The linewidth of the cavity is related to the dissipations through the cavity mirrors. So, it can be defined using the Quality factor, $Q = \omega/\Delta\omega_c$. In a low Q-cavity, the emitter undergoes an emission in an enhanced rate. The radiative rate inside a cavity of

volume V can be calculated as[62, 55]:

$$\tau_{cav} \approxeq \tau_{vac} \frac{Q\lambda^3}{V} \tag{2.23}$$

The emission rate is increased by a ratio of $\frac{Q\lambda^3}{V}$ inside cavity.

These effects inside the cavity are characteristics of the weak coupling regime, which is the case in which photon is not reabsorbed by the emitter as they are lost in to the far-field much faster than the emitter can interact with the cavity. However, the spontaneous emission becomes reversible when the energy exchange between the emitter and the field dominates the dissipative processes in the system, which is referred as strong coupling regime. This will be detailed in the next section.

2.3 Strong-Coupling Cavity QED

If the resonant interaction between the confined electromagnetic field and matter is strong enough the energy exchange between the light and the matter become reversible. In this regime, dubbed strong light matter coupling, not only the radiative decay rates are affected as in the weak coupling regime, but also new energy levels are formed in the system. The formation of the two new hybrid states separated in energy is known as Rabi splitting[63]. The first experimental demonstration in this direction was strong exciton-photon coupling in 1975[64]. The phenomena was first theoretically explained by the Jaynes Cummings model [65] which describes the single emitter coupled to a single cavity mode.

2.3.1 Coupled Harmonic Oscillator Model

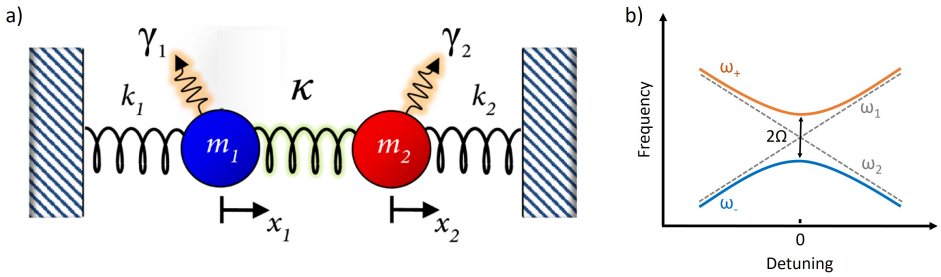

Fig. 2.5 **Coupled Harmonic Oscillator Model for Strong Coupling.** a) Two coupled harmonic oscillators. $\gamma_{1,2}$ are the loss rates, $\sqrt{\frac{k_{1,2}}{m_{1,2}}}$ are the eigen frequencies of the bare oscillators, κ is the coupling spring constant, $x_{1,2}$ are the displacements from equilibrium[66]. b) Anti-crossing behaviour of two coupled classical oscillators

The strong light matter interaction can be described by the behaviour of a two coupled harmonic oscillators like the one shown in Figure 2.5a[66]. When the oscillators are strongly coupled, they exchange energy periodically and the system behaves like a single entity instead of two independent oscillators. This results in the changes in energy spectrum of the system(Figure 2.5b). In the classical analogy, the two damped harmonic oscillators that are

coupled together can be written as:

$$\begin{aligned}\ddot{x}_1 + \gamma_1\dot{x}_1 + \omega_1^2 x_1 - \Omega^2 x_2) = 0\\ \ddot{x}_2 + \gamma_2\dot{x}_2 + \omega_2^2 x_2 - \Omega^2 x_1) = 0\end{aligned} \tag{2.24}$$

x_j (j = 1, 2) is the displacement from equilibrium of the j^{th} oscillator, which has an uncoupled eigen frequency $\omega_j = \sqrt{k_j/m_j}$ and a loss rate γ_j. Solving for ω, we obtain the normal mode frequencies $\omega_\pm$:

$$\omega_\pm = \frac{1}{2}\left(\omega_1 + \omega_2 \pm \sqrt{(\omega_1 - \omega_2)^2 + 4\Omega^2}\right) \tag{2.25}$$

where ω_+ and ω_- are the two new frequencies of the system, and Ω is the frequency splitting. At resonance, when $\omega_1 = \omega_2 = \omega$ the new frequencies become $\omega_\pm = \omega \pm \Omega$(Figure 2.5b).

Quantum Picture

The 'zero point' energy or vacuum fluctuations cannot be explained using classical description. Hence, the ultra-strong coupling regime cannot be described using classical picture, i.e. when the lower polariton becomes the ground state[15]. In cavity quantum electrodynamics(cQED), the simplest system consisting of a single emitter placed inside the cavity is well described by Jaynes Cummings Hamiltonian[65]. Here, the energy of the coupled system can be written as the sum of dipole, electric field and the dipole field interaction within the rotating frame approximation[49],

$$\begin{aligned}\hat{H}_{JC} &= \hat{H}_{mat} + \hat{H}_{cav} + \hat{H}_{int}\\ &= \frac{1}{2}\hbar\omega_0\hat{\sigma}_\sigma^\dagger + \hbar\omega_c(\hat{a}^\dagger\hat{a} + \frac{1}{2}) + \hbar g_0(\hat{a}^\dagger\hat{\sigma} + \hat{a}\hat{\sigma}^\dagger)\end{aligned} \tag{2.26}$$

where σ and $\sigma^\dagger$ are the raising and lowering operator acting on the two-level dipolar system respectively, $\hat{a}^\dagger$ and $\hat{a}$ are annihilation and creation operators of the electromagnetic field, ω_0 and ω_c are the transition frequencies of the dipole and the cavity and g_0 is the light matter coupling strength. $\hat{a}^\dagger\hat{\sigma}$ corresponds to the material excitation from the ground state to the excited state and and the annihilation of a photon in the cavity($\hat{a}\hat{\sigma}^\dagger$ is the reverse process).

Jaynes-Cummings model can be extended for many emitter case using the Dicke or Tavis-Cummings Hamiltonian[67, 68]. Solution for the Hamiltonian can be reduced to an equivalent system comprising a giant oscillator coupled to the electromagnetic field of the cavity with the use of Holstein– Primakoff transformation[69].

$$\hat{H} = \hbar\sum_{i=1}^{N}\omega_0\hat{\sigma}_i^\dagger\hat{\sigma}_i + \hbar\omega_c\hat{a}^\dagger\hat{a} + \hbar g\sum_{i=1}^{N}(\hat{a}^\dagger\hat{\sigma} + \hat{a}\hat{\sigma}^\dagger) \tag{2.27}$$

where $g = g_0\sqrt{N}$ is the collective coupling strength which reveals that the coupling strength can be enhanced by a factor of $\sqrt{N}$ in the collective coupling.

Diagonalization of the Jaynes-Cummings Hamiltonian using Hopfield-Bogoliubov method yields two light matter hybrid eigen states of the system called polaritonic states

or Polaritons[70] and a set of N-1 dark states[1] of material excitations at the energy ω_0 of the bare dipoles. Lower and upper polaritons(LP and UP) can be written as the linear combination of light and matter as,

$$|UP\rangle = \alpha \sum_{i=1}^{N} |e_i, 0\rangle + \beta |g, 1\rangle \tag{2.28}$$

$$|LP\rangle = \beta \sum_{i=1}^{N} |e_i, 0\rangle + \alpha |g, 1\rangle \tag{2.29}$$

where, $|g\rangle$ and $|e\rangle$ are the ground state and excited state of the matter respectively and $|0\rangle$ and $|1\rangle$ are the Fock states of the cavity. $|\alpha|^2$ and $|\beta|^2$ are the Hopfield coefficients describing the optical and material character of each of the polaritons[49]. The splitting between the upper and lower polariton is called vacuum Rabi splitting(Ω in Figure 2.6a) which can be expressed as a function of coupling strength,g[2]:

$$\hbar\Omega = 2\hbar g = 2d\sqrt{N}\sqrt{\frac{\hbar\omega_c}{2\epsilon_0 V}} \tag{2.30}$$

It can be noted that the coupling between light and matter is dependent on the parameters like transition dipole moment(d), number of emitters(N) and the mode volume(V). Hence, the strong coupling can be achieved only in emitters with high value of d and cavity mode volume(V) has to be made small as possible in order to enhance the coupling strength. However, the decrease in the cavity mode volume is limited to one mode of the electromagnetic field in the case of Fabry Perot cavity. The Jaynes-Cummings model does not include dissipations, therefore does not give the conditions for the transition from the weak coupling to strong coupling limit.

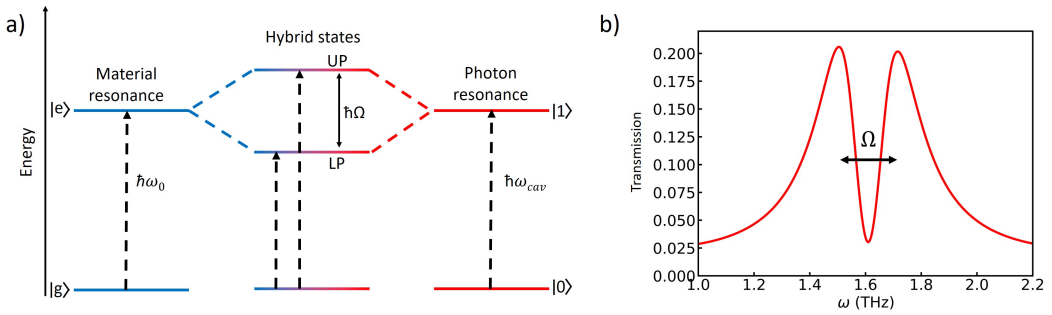

Fig. 2.6 **Light-Matter Strong Coupling inside a Cavity.** a) Energy Diagram of Light-Matter Strong Coupling inside a Cavity. Strong coupling results in the formation of light matter hybrid states LP and UP with a splitting of $\hbar\Omega$ between them b) Splitting of the transmission spectra in to two peaks(LP and UP) when the system is in the resonant condition

[1]The dark states are dipole-forbidden excitations generated through the strong light-matter coupling and hence invisible to linear spectroscopy

[2]we recall that the dipolar coupling between light and matter in Equation 2.21 and vacuum electric field for cavity as $E_{vac} = \sqrt{\frac{\hbar\omega_c}{2\epsilon_0 V}}$

Strong-to-weak coupling transition

The transition of the system from weak coupling to strong coupling regime is governed by the decay rate of the cavity(γ_c), non-resonant decay rate of the material(γ_0) and the coupling strength(g). These parameters of cavity and the material can be measured experimentally in order to understand the nature and strength of light–matter interactions. When $g << (\gamma_0, \gamma_c)$ the system is in the weak coupling regime and when g exceeds the dissipation processes(γ_0, γ_c) the system falls in to the strong coupling regime. The strong coupling regime is characterized by the coherent exchange of energy between light and the matter so that the cavity photon is reabsorbed by the material several times before it is lost to the environment. We note that γ_0 and γ_c are the linewidth of the cavity and excitation in the material respectively. At resonance condition in the strong coupling regime, the transmission linewidth of each peak of the coupled system is $[\gamma_0 + \gamma_c]/2$. The polariton peaks will be spectrally resolvable only when the splitting Ω is wider than this linewidth. So, the strong coupling occurs only when the splitting between the polaritonic states(Figure 2.6b) is larger than the transmission linewidths (full width of half maximum(FWHM)) of the bare cavity(γ_c) and the material resonance(γ_0)[71, 18, 49].

$$\Omega > \frac{\gamma_c + \gamma_0}{2} \tag{2.31}$$

Under conditions of strong coupling, weak optical probing near the cavity resonant frequency reveals two spectral transmission peaks(Figure 2.6b) (where only one existed before corresponding to the cavity mode) giving the energies of new hybrid polaritonic states. However, splitting in the spectra alone cannot fully confirm the strong coupling. Because, the spectra can be split due to the effects in weak coupling regime like inhomogeneous broadening[72], cavity induced transparency[73, 74] and Fano resonance in plasmonic structures[75–77]. In addition to the splitting of the spectra(Figure 2.6b), the strong coupling regime has to be verified from the anti-crossing behaviour of the cavity mode and material excitation which can be visualized by tracking the dispersion of polaritonic states.

The Hamiltonian description of the light-matter interaction within the cavity can be obtained using the Dicke model[78] with a single two-level system, N=1, called Rabi model[79]. The Rabi model can be exploited to fit and extract parameters from transmission measurements by treating the cavity and the material excitation as coupled oscillators[80, 49] with a coupling element $1/2\hbar\Omega$. This method has the advantage to be solvable analytically, yet captures most of the essential underlying physics. The coupling between the cavity photon and the material can be described by a 2 X 2 matrix Hamiltonian:

$$\hbar \begin{pmatrix} \omega_c & \Omega/2 \\ \Omega/2 & \omega_0 \end{pmatrix} \begin{pmatrix} \alpha \\ \beta \end{pmatrix} = E \begin{pmatrix} \alpha \\ \beta \end{pmatrix} \tag{2.32}$$

where ω_c is the cavity frequency, ω_0 is the material excitation and Ω is the Rabi splitting.

Diagonalization of this Hamiltonian gives the eigen values corresponding to the polaritonic states and hence the dispersion of the polaritons.

$$E^{\pm} = \hbar\frac{(\omega_c + \omega_0)}{2} \pm \sqrt{(\hbar\Omega)^2 + (\hbar\omega_c - \hbar\omega_0)^2} \tag{2.33}$$

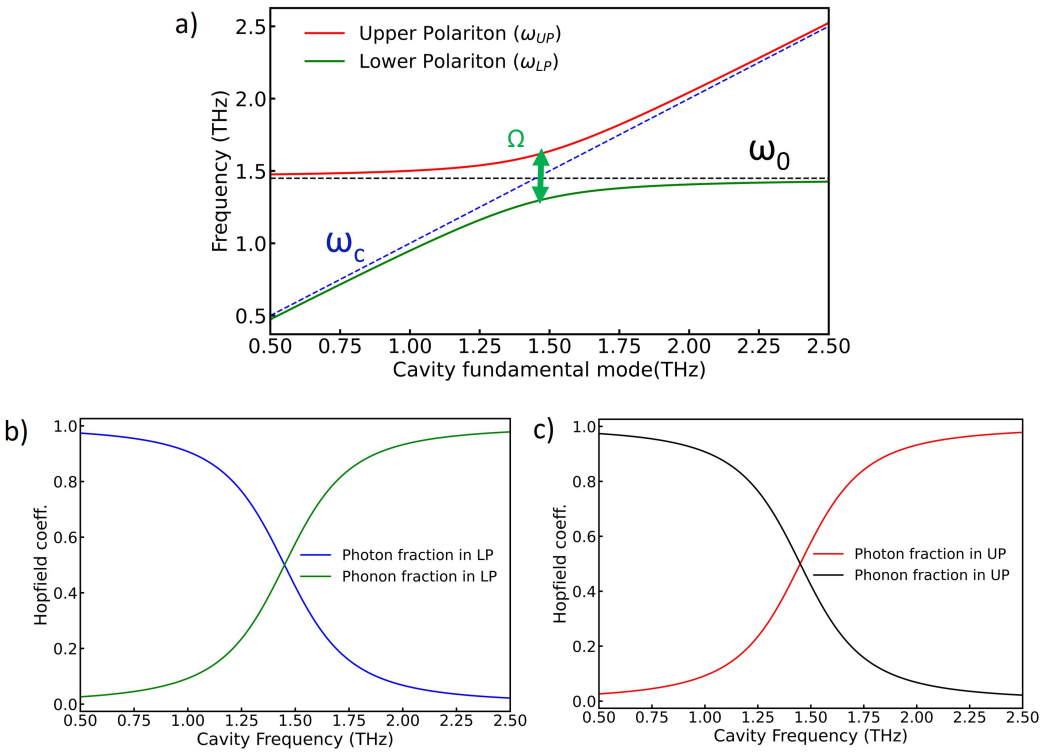

Fig. 2.7 **Dispersion of the Polaritons predicted by Coupled Harmonic Oscillator Model.** a) Upper and lower polaritons plotted as function of the cavity fundamental mode ω_c obtained by the coupled harmonic oscillator model($\omega_0 = 1.45$ THz, g=0.16 THz). The bare cavity(ω_c) and material resonance(ω_0) are shown as dashed lines. b) The photon and material fraction of the b) lower polariton(LP) and c) upper polariton(UP) obtained from the Hopfield coefficients

Furthermore, the Hopfield coefficients corresponding to the photon and material character of the polaritons can be extracted through the eigenvectors.

$$|\alpha|^2 = \frac{1}{2}\left(1 + \frac{\omega_0 - \omega_c}{\sqrt{(\omega_0 - \omega_c)^2 + 4g^2}}\right) \tag{2.34}$$

$$|\beta|^2 = \frac{1}{2}\left(1 - \frac{\omega_0 - \omega_c}{\sqrt{(\omega_0 - \omega_c)^2 + 4g^2}}\right) \tag{2.35}$$

The Figure 2.7a shows the dispersive nature of the polaritons obtained by placing a material with a resonance at 1.45 THz inside an optical cavity($g = 0.16$ THz) using coupled harmonic oscillator model(CHO). The dispersion has been tracked by detuning the cavity frequency. The energy curves diverge from each other at resonance condition. This effect is called anti-crossing, a distinctive feature in the strong coupling regime. The minimum value of energy separation between these two branches determines the Rabi splitting($\Omega = 0.32$ THz). Figure 2.7b and Figure 2.7c shows the extracted ratio between the optical and material character of the lower(LP) and upper(UP) polaritons respectively, obtained from the Hopfield coefficients defined as $|\alpha|^2$ and $|\beta|^2$. It can be seen that, at

resonance, i.e. when the material excitation matches the frequency of the cavity, the polariton is a hybrid state of half-light and half-matter.

3

Soft Mode Dynamics and Ferroelectricity in $SrTiO_3$

3.1 Soft Mode Concept of Ferroelectricity

3.1.1 Introduction to Ferroelectrics

Ferroelectrics are the materials that exhibit spontaneous electric polarization with two stable and switchable polarization states[81]. The first ferroelectric material was found in the 1920s in Rochelle salt [82]. All ferroelectrics are pyroelectric and piezoelectric being sensitive to mechanical stress and temperature respectively. The most important characteristics of the ferroelectrics are Curie's temperature (Tc), ferroelectric domain and domain switching. Curie temperature is the temperature associated to the phase transition from paraelectric phase to ferroelectric phase. Below the transition temperature, ferroelectric domains are formed to minimize the electrostatic energy related to depolarizing fields and the elastic energy associated with mechanical constraints[83]. Domain switching corresponds to response of the domains towards the applied electric field. In the ferroelectric phase, the dipoles in the material becomes oriented with respect to the applied electric field resulting in an increase in the macroscopic polarization until the domains are completely aligned. When the applied electric field is reduced to zero, the material would still possess some net polarization that is lower than the saturation polarization. This is the remanent polarization. When a bipolar external electric field in excess of the coercive field is cycled, an electric polarization/electric field hysteresis loop (P-E hysteresis loop) is generated[84]. This analogies with ferromagnetism result in the term ferro in the definition of ferroelectricity. Figure 3.1 shows the P-E hysteresis loops of a classical ferroelectric which is the most common hysteresis loop.[84]

Among the great variety of ferroelectrics, the largest class is consisted of perovskite oxides. These materials have a general chemical formula of form ABO_3 with a structure shown in Figure 3.2. A, B are metal atoms, O is oxygen atom where A is on the eight vertexes (blue balls), B is in the body center of unit cell(yellow ball), O occupies the center of the six faces (red balls), and the blue octahedrons are $[BO_6]$ octahedrons. Their relatively simple chemical and crystallographic structures led to investigation of their properties. The

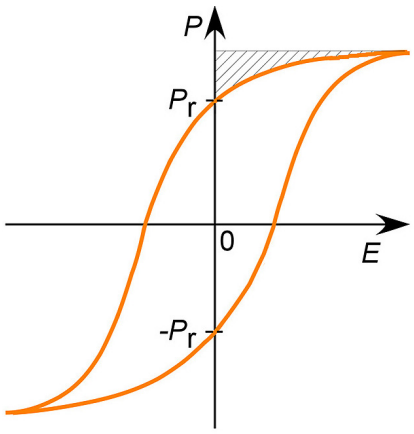

Fig. 3.1 **Electric polarization/electric field hysteresis loop of the ferroelectric.** Dependence of the polarization against electric field for a classical ferroelectric (Figure is taken from [84])

spontaneous polarization of ferroelectrics originates from the inner structure, i.e. the net polarization in this materials arises due to the displacement of positive ion in the center with respect to the negative ions in the unit cell.

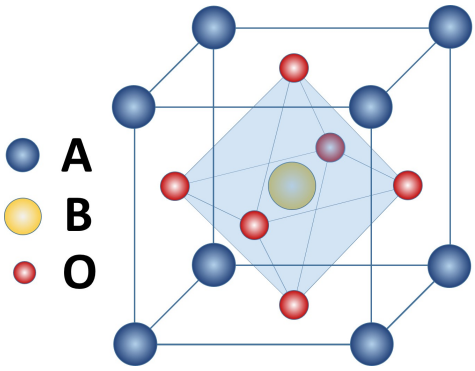

Fig. 3.2 **Chemical Structure Perovskite Oxide.** Structure of the materials with the chemical formula of form ABO_3. A, B are metal atoms(yellow and blue), O is oxygen atom(red)

One of the important advantages of ferroelectrics is that the energy can be stored and generated in the form of switchable ionic polarization. Under adiabatic compression, ferroelectrics have been used to produce high electric charge density enabling creation of compact, lightweight ferroelectric power sources that are capable of producing high voltage, high current, and megawatt power levels for brief intervals of time[85–90]. There are also other possible applications of high-power ferroelectric systems that require high current, high voltage, high power, portability, compactness and a need for a limited number of events[84]. Another important application of ferroelectric materials in energy storage technologies is as a medium in dielectric capacitors but with different energy storage mechanism[91–96].

3.1.2 Ferroelectric Phase Transition

Ferroelectricity prevails only at low temperatures. As the temperature is raised, the macroscopic polarization decreases and vanishes above transition temperature, T_c due to the phase transition in to a higher symmetry phase called paraelectric(PE) phase[97]. The Curie point in ferroelectrics can be defined as the temperature in which the long range ferroelectric order overcomes the short range thermal fluctuations.

The ferroelectricity can be modelled by Landau-Ginzburg-Devonshire theory (LGD) in which the order parameter is the polarization(P). So the Gibbs energy can be written in terms of the order parameter as[98, 99],

$$G = F - EP = F_0 + \frac{\alpha}{2}P^2 + \frac{\beta}{4}P^4 + \frac{\gamma}{6}P^6 - EP \tag{3.1}$$

where F_0 is the free energy density of the paraelectric state near the phase transition. α, β, γ are parameters depending on temperature and pressure and E is the electric field.

For a second order phase transition[100], the $\beta > 0$ and $\gamma = 0$ according to Landau theory, and the parameter α can be written as a function of the Curie temperature and the Weiss constant C[1]

$$\alpha = \frac{1}{\varepsilon_0 C}(T - T_c) \tag{3.2}$$

since it changes sign crossing T_c, there are two new stable minima as shown in Figure 3.3a. At the minima of the Gibbs energy, the spontaneous polarization(P_s) can be written as,

$$P_s = \pm\sqrt{-\frac{\alpha}{\beta}} = \pm\sqrt{\frac{1}{\varepsilon_0 \beta C}(T_c - T)} \tag{3.3}$$

where the double sign represents the two different direction of spontaneous polarization. T_c represents the transition temperature. Here the change in free energy occur continuously as temperature is decreased. The name second-order results from the discontinuity in the second order derivative of the free energy or susceptibility.

In the case of a first order transition, the parameters are

$$\alpha = \frac{1}{\varepsilon_0 C}(T - T_0), \quad \beta < 0, \quad \gamma > 0 \tag{3.4}$$

where T_0 represents the temperature at which the two polarizations are the only two stable configurations, while we define T_C when we have three minima, as represented in (Figure 3.3b. Assuming $E = 0$, it is possible to compute T_C

$$F = \frac{\alpha}{2}p^2 + \frac{\beta}{4}p^4 + \frac{\gamma}{6}p^6 = 0 \tag{3.5}$$

where the solutions are

$$P = 0 \tag{3.6}$$

[1]We recall the Weiss law for the susceptibility χ: $\chi = \frac{C}{T - T_C}$

$$P = \pm\sqrt{\frac{1}{4\gamma}(-3\beta + \sqrt{9\beta^2 - 48\gamma\alpha})} \tag{3.7}$$

which means that

$$\alpha = \frac{3\beta^2}{16\gamma} \quad \text{i.e.} \quad T_C = T_0 + \frac{3\epsilon_0 C\beta^2}{16\gamma} \tag{3.8}$$

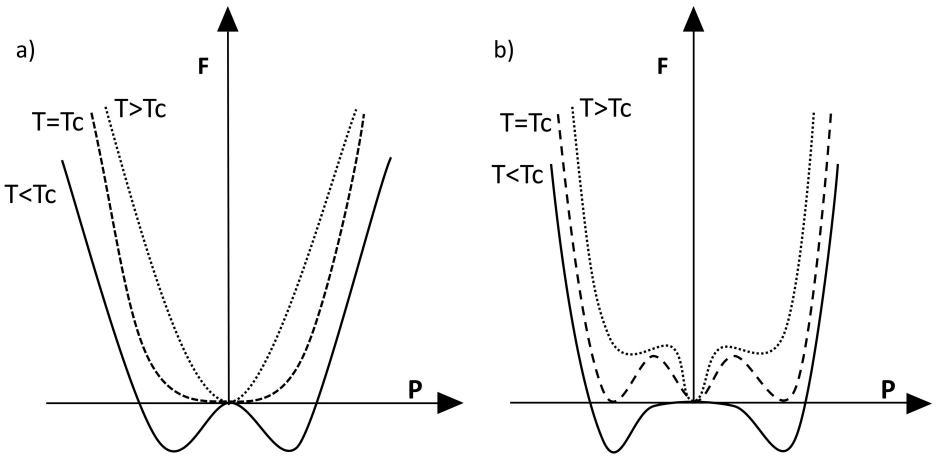

Fig. 3.3 **Free Energy Diagram of Ferroelectric Phase Transition.** Free energy as a function of polarization for a) second-order phase transition and b) first-order transition at $T > T_c$, $T = T_c$ and $T < T_c$

From the previous equations, at $T = T_C$ the polarization shows a jump of

$$\Delta P = \sqrt{\frac{-3\beta}{4\gamma}} \tag{3.9}$$

Here, polarization is discontinuous at the Curie temperature, T_C. There are two notable temperatures for a first-order transition. T_C is the temperature at which the three local minima of the free energy are energetically degenerate and the second T_0 is where the quadratic coeffcient, α changes the sign from positive to negative. This enables for the low temperature phase to exist at higher temperatures and viceversa as metastable states. This leads to thermal hysteresis in the phase transition.

Below the Curie temperature, the stable configurations are two and minimum energy state can be calculated as

$$P_s = \pm\sqrt{\frac{\beta}{2\gamma}\left(1 - \sqrt{1 - \frac{4\alpha\gamma}{\beta^2}}\right)} \tag{3.10}$$

When it comes to materials like $BaTiO_3$ or $PbTiO_3$ [101], the coupling between the strain and polarization also has to be taken into account in the energy expansion since the ferroelectricity is associated to the structural changes in the crystal. The expansion associated to the strain can be written as

$$F_{strain} = \frac{1}{2}K\eta^2 + Q\eta P^2 \tag{3.11}$$

where K represents the Hooke's law and Q represents the coupling between strain and polarization.

3.1.3 Softmode in Ferroelectrics

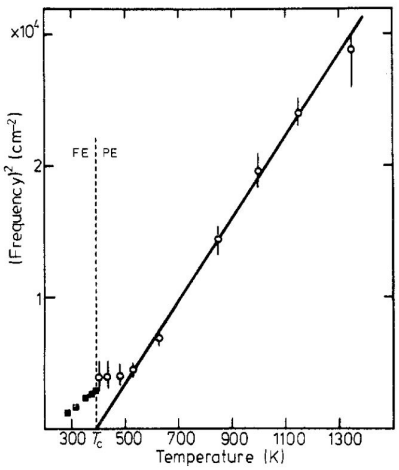

Fig. 3.4 **Softening of the Transverse Mode in Perovskites.** Temperature dependence of the frequency squared of the lowest transverse mode for $BaTiO_3$. Raman data (black squares) are those of ref[102].[103]

In potential ferroelectrics, the average value of the order parameter, P denoted by $< P >$ vanishes above the transition temperature. It has to be noted that P itself is not a static quantity but $< P >$ is. The fluctuations in P are derived from the collective atomic displacements called the phonon mode vibrations. These fluctuations are so organised above T_c resulting the $< P >$ to vanish[104].

In perovskite oxides, the ferroelectric order is generally associated to the polar instability resulting from the lowest energy transverse optical phonon mode(s). The ferroelectric transitions are usually divided in to two mechanisms, displacive and order-disorder transition. In a displacive transition the soft mode freezes at the phase transition(Figure 3.4) meanwhile in order-disorder transition the frequency of the soft mode only decreases enough to allow the thermal hopping between the two available free energy wells[81]. Ferroelectrics are classified based on which of the above mentioned mechanisms dominate the phase transition. The classic ferroelectrics BTO and lead titanate, $PbTiO_3$ are examples of displacive ferroelectrics. In contrast the more chemically complicated potassium dihydrogen phosphate, KH_2PO_4 and sodium nitrite, $NaNO_2$ are of the order-disorder type [81].

We will be discussing the soft mode dynamics based on the displacive transition which is dominant in most of the classical ferroelectrics. The lattice stability is achieved when vibrational modes have real and finite frequencies and it reaches its limit when the phonon mode freezes. This occurs at the phase transition and the phonon mode that vanished is called soft mode. If the frequency of the mode is zero, once atoms are displaced in the

course of that particular vibration, there is no restoring force to return them to their original equilibrium position. The atoms then assume new equilibrium positions determined by the symmetry of the mode, and the structure of the crystal changes[97]. Hence, the displacement of the central metal ion in to a non-centrosymmetric region of the octahedron induces a finite dipole moment in the unit cell. These displacement associated to the soft mode can be considered as order parameter of the ferroelectric phase transition as they are directly related to the spontaneous polarization.

The softening and ultimate vanishing of the soft mode at the transition temperature occurs due to the cancellation between competing forces (short-range and long-range Coulombic forces in the case of ferroelectrics)[97]. This cancellation can be induced by changes in composition, temperature, or other external fields. In particular, the application of pressure can significantly influence the balance between competing forces and thereby strongly influence the soft-mode behavior.[105]

The anharmonic effect plays a crucial role in the mode softening. The mode softening can be understood by considering the lattice dynamical Hamiltonian[106]. So, for frequency mode j with wave vector q:

$$H = \frac{1}{2}\sum_{q,j} P(q,j)P(-q,j) + \omega_0^2(q,j)Q(q,j)Q(-q,j) \tag{3.12}$$

where the Q's denote the normal coordinates and the P's the conjugate momenta. Considering that the quartic anharmonicities are present in the system the effective Hamiltonian can be written as,[104]

$$H = \frac{1}{2}\sum_{q,j} P(q,j)P(-q,j) + \omega_0^2(q,j)Q(q,j)Q(-q,j) + \sum_{q,\kappa}\sum_{j,k,l,m} g^{(4)}_{j,k,l,m}(q,\kappa) < Q(q,j)Q(-q,k) > Q(\kappa,l)Q(\kappa,m) \tag{3.13}$$

where $g^{(4)}$ is the fourth-order coupling constant and the resulting renormalized mode frequency can be written as,[104]

$$\overline{\omega}^2(q,j) = \omega_0^2(q,j) + 2\sum_{\kappa}\sum_{l,m} g^{(4)}_{j,j,l,m}(q,\kappa) < Q(\kappa,l)Q(-\kappa,m) > \tag{3.14}$$

Specifically, the square of the harmonic frequency, ω_0 is presumed to be sufficiently negative (i.e., ω_0 is imaginary) that this mode cannot be stabilized by zero-point anharmonicities alone. Thermal fluctuations then renormalize ω_0 and make it real at finite temperatures, thereby stabilizing the lattice. As temperature is lowered, the anharmonic contribution cannot overcome the effects of ω_0^2 sufficiently. This would lead ω_0 to be negative resulting the crystal to be unstable.

By evaluating the equation for mode frequency, we obtain[105, 107]

$$\omega_T^2(q,j) = \omega_0^2(q,j) + 2\sum_{l,\kappa} g^{(4)}_{lj}(q,\kappa) \times \frac{1}{2\omega(\kappa,l)} \coth\left(\frac{\omega(\kappa,l)}{2k_B T}\right) \tag{3.15}$$

over all modes l and wave vectors κ. At sufficiently high temperatures, when $\omega_0 << k_B T$

$$\omega_T^2(q,j) = \omega_0^2(q,j) + \alpha(T - T_c) \tag{3.16}$$

where $\alpha = K_B \sum_{l,k} g^{(4)}_{j,j,l,l}/\omega_0(\kappa,l)$.

In FE crystals, the temperature dependence of ω_0 is responsible for the observed Curie-Weiss temperature dependence of the static dielectric constant, ϵ_0 and for the divergence of ϵ_0 at the transition.

$$\epsilon_0 = C/(T - T_c) \tag{3.17}$$

where C is a constant. This is because ϵ_0 and ω_0 are related by the Lyddane-Sachs-Teller relationship which, to a very good approximation, leads to the result [105, 97]

$$\epsilon_0(T)\omega_0^2(T) = constant. \tag{3.18}$$

3.2 Ferroelectricity in $SrTiO_3$

The ferroelectric transition in a material is determined by the competition between the long range FE order and fluctuations that disrupts the system[97]. In the classical regime, i.e. in the high temperature phase the FE ordering is hindered by the thermal fluctuations. If the transition is occuring at sufficiently low temperatures where the quantum effects are dominant the quantum fluctuations, or zero-point motions will prevent long range FE ordering resulting in the suppression of ferroelectricity in the material. Here the free energy can be presumed as a double well like the one shown in Figure 3.3 below T_c, but the system cannot stay in one of the two minima: due to quantum fluctuations it tunnels in between them and it does not find a stable configuration.[99]

When the transition is in the quantum regime the total fluctuations do not reduce by decreasing the temperature. This results in the high temperature paraelectric phase to extend below the classical limit of phase transition temperature. At low enough temperatures, quantum fluctuations can suppress the ferroelectric transition completely. This would result in the formation of quantum paralectric state characterized by high static dielectric susceptibility which would saturate at low temperatures[97, 99].

Another aspect related to the suppression of phase transition is the special critical point which is T_c^q=0 K. This is referred to as quantum displacive limit and it gives rise to classical to quantum crossover phenomena[108, 109, 97]. Various studies in the displacive limit has provided relation between transition temperature and interaction parameter(S) which is proportional to the mean square fluctuations of the ionic displacements as[108, 109, 97],

$$T_c(S) = (S - S_{min})^{1/\phi} \tag{3.19}$$

S_{min} is the value of S for T_c^q=0 K. The value of ϕ is 2 close to T_c^q=0 K and 1 for large S i.e. in the classical regime as shown in the Figure 3.5. In the experimental frameworks, it is important to relate S to some measurable variable such as pressure or chemical composition which can be achieved by assuming that S is proportional to the lattice parameter[110, 97].

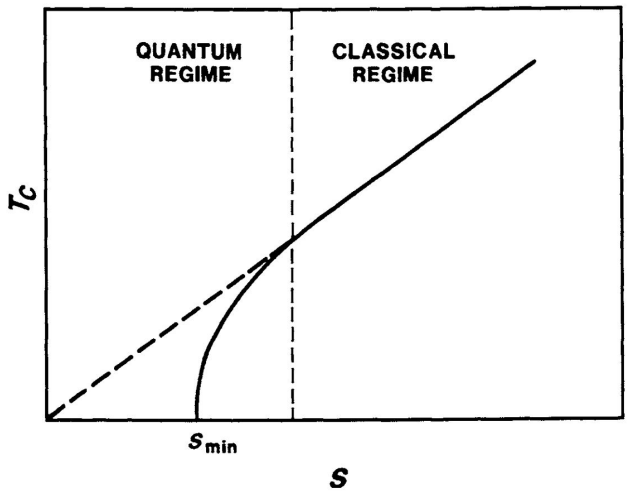

Fig. 3.5 **Quantum Ferroelectric State.** Schematic phase diagram for a quantum ferroelectric. The interaction parameter S is proportional to pressure or composition. [97]

The influence of quantum effects has been reported in the perovskites $SrTiO_3$ and $KTaO_3$ suppressing the ferroelectric transitions in this materials. Hence they are called incipient ferroelectrics. At low temperature, these crystals exhibit the quantum paraelectric state in atmospheric pressure conditions[111, 112, 97]. The dielectric response of these materials show a deviation from the Curie Weiss form at low temperatures. This deviation has been formulated by Barret expression[113, 105] in a $KTaO_3$ crystal[114] as,

$$\epsilon_0 = A + \frac{B}{\frac{1}{2}T_1 \coth(T_1/2T) - T_0} \tag{3.20}$$

where T_0 is the transition temperature in the classical limit.

The perovskite crystal $SrTiO_3$ has huge dielectric constant at low temperature(~ 23000 below ~ 5 K) making it easier to align the dipoles by applying an external stimuli as the lattice polarizability is high. In the next section, we will present different studies that has reported an induced ferroelectric transition in the paraelectric $SrTiO_3$ crystal.

3.2.1 Calcium and Isotopic Substitution

When the Sr^{2+} ions are substituted by Ca^{2+} ions, the difference in the ionic radii of Calcium (114 pm) from Strontium(132 pm) would result in a change in the equilibrium position of Ca atoms[115]. This results in a local net dipole and due to the huge dielectric constant the material falls in to a ferroelectric state[116]. This can be also explained by the the damping of quantum fluctuations due to Ca substitution. The Ca atoms increase the barrier in the double well potential suppressing the tunnelling between the two ferroelectric minima[117, 99].

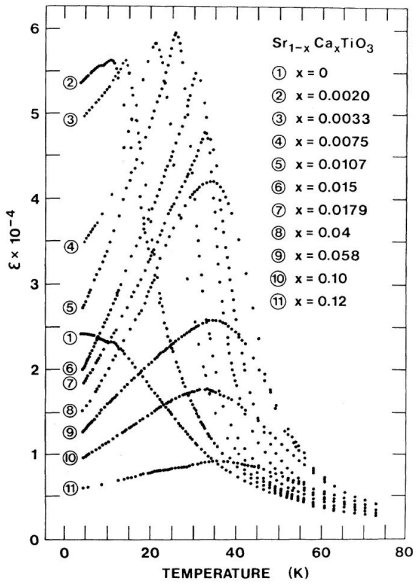

Fig. 3.6 **Ferroelectric Transition in Ca-doped $SrTiO_3$ Crystal.** Temperature dependence of the static dielectric constant(ϵ) of $Sr_{1-x}Ca_xTiO_3$ crystals with x between 0.0 and 0.12.[116]

Bednorz and Muller[116] have conducted studies in a $Sr_{1-x}Ca_xTiO_3$ sample using dielectric measurements and revealed a ferroelectric domain state for Ca concentration ranging from $0.002 \leqslant x \leqslant 0.12$. The result of the studies are shown in Figure 3.6[116].

In pure $SrTiO_3$, i.e. when x=0 ferroelectricity is suppressed because of the quantum fluctuations. The static dielectric constant is saturating below 10 K. By increasing the concentration x, it can be seen that above the concentration x =0.0018, the crystal shows ferroelectric features like a peak maximum in the static dielectric constant(ϵ) which can be associated to the transition temperature T_c. The T_c deduced from the maximum of the ϵ has been reported to be related to the Ca concentration as $(x - x_c)^{\frac{1}{2}}$ between the quantum critical point $x_c = 0.0018$ and $x = 0.0075$. Hence, obeying the Equation 3.19($S = x$) for the transition temperature near the quantum displacive limit[97]. Upon increasing the Ca concentration above $x_r = 0.016$, the peaks show a transition which is diffused, which has been attributed to the onset of random-field induced domain state i.e. due to random electric fields introduced by Ca^{2+} doping in $SrTiO_3$. In Addition, the T_c becomes independent of concentration above x=0.016 breaking the law of quantum ferroelectrics(Equation 3.19). It can be said that, from x_c to x_r the system crosses over from true quantum ferroelectric at x_c, to classical behavior as T becomes different from zero[116].

In 1999, quantum ferroelectricity has been reported in oxygen isotope substituted STO sample by Itoh et al. [118]. They found that replacing O^{16} with O^{18} results in the emergence of a peak in static dielectric constant (ϵ_0) indicating the ferroelectricity in STO18. The transition temperature of 23 K has been observed in STO18 which is almost the same as the peak temperature of the Ca-substituted system, 18 K. In Itoh and Wang [119], the authors have shown that the transition temperature can be written as a function of fraction of O^{18} using the law for quantum ferroelectrics as $T_c(x) = 28(x - x_c)^{\frac{1}{2}}$ with $x_c = 0.36$ indicating that the origin of ferroelectricity is a quantum effect.

The lattice parameter is the same for O^{16} and O^{18}. So, the authors have attributed the effect to a change in the vibrational frequencies of relevant ion pairs due to the mass change of the constituent atoms. Therefore, the enhanced mass of the oxygen ion from 16 to 18 leads to a lower soft mode frequency and $T_c = 0$ K for the sample with x=0.36[119]. The suppression of quantum fluctuations have been a widely believed origin for the induced ferroelectricity which has been framed using Barret's formulaEquation 3.20. There have been efforts to explain this by a decrease in T_1 or an increase in T_0 upon isotope substitutions[120, 121]. However, a clear explanation for this evolution still remain unsettled.

3.2.2 Strain

The polarization in a ferroelectric material can be controlled by means of strain on the material[122–124]. Thin film materials are a good candidates for this purpose due to their high stress tolerance. One of the many ways to strain a thin film is the development of the new substrates enabling the growth of uniformly strained films[125]. The differences in the lattice parameters and thermal expansion behaviour between the film and the underlying substrate will result in the development of misfit strain[126–128]. The biaxial strain from lattice mismatch between the film and the substrate can be defined as, $s = \frac{a_s - a_f}{a_s}$ where a_s and a_f are substrate and thin film lattice parameters respectively[124]. For tetragonal perovskite ferroelectric materials like STO, the ferroelectric performance is closely related to the axial ratio. Hence, strain can have a significant influence on the tetragonality of the material making it an effective way to tune the performance of perovskite ferroelectric materials[124, 129].

There have been experimental frameworks[125, 130, 131] that have reported strain induced ferroelectricity in STO thin films. Haeni et al. [125]. has reported room temperature ferroelectricity in STO thin films grown on $DyScO_3$ by imposing a tensile strain of 0.8%. The authors have observed Curie–Weiss behaviour in static dielectric constant with a maximum at $T_c \sim 293$ K and a Curie constant typical of displacive ferroelectrics. The theoretical studies[126] on the soft mode behaviour in strained $SrTiO_3$ thin films have shown that reducing strain results in a decrease in the ferroelectric transition temperature(T_c), accompanied by nonlinear behavior at lower strain levels. T_c approaches T= 0 K for a critical tensile strain of 0.038% below which the spontaneous polarization of the STO thin film is completely suppressed and the material behaves like a paraelectric even at T = 0 K.

3.2.3 Resonant Terahertz Laser Pumping

Li et al. [132] has reported a transition in to a hidden ferroelectric state in $SrTiO_3$ by driving the FE soft mode using intense terahertz light. The excitation of the soft mode using the terahertz pulses causes a dynamic response in the crystal, resulting in the movement of ion in the crystal in to new positions. The coherent soft-mode lattice vibrational motion leads to inversion symmetry breaking in the crystal transforming the crystal in to a lower symmetry geometry with a dipole moment. The long range ordering of the dipole moments causes the quantum paraelectric(QPE)-to-ferroelectric(FE) phase transition in STO. In STO, the terahertz induced highly nonlinear responses of FE soft mode overcomes the quantum fluctuations and hence, favours the ferroelectric ordering in the crystal. Figure 3.7a shows the

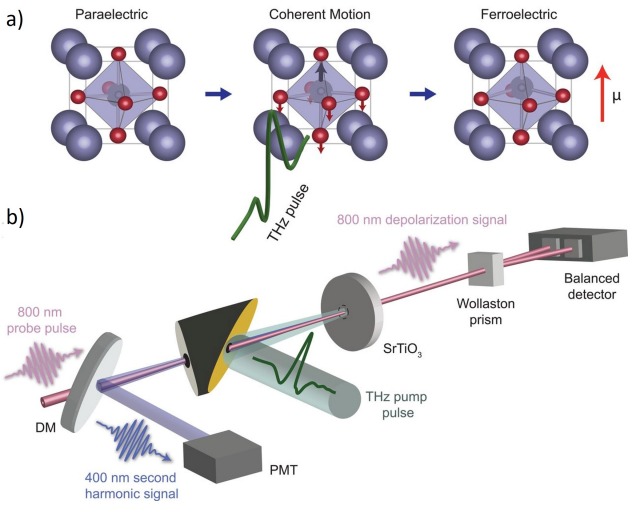

Fig. 3.7 **Terahertz Induced Ferroelectricity in $SrTiO_3$.** a) The single cycle terahertz field drives the "soft" lattice vibrational mode towards new positions resulting in a lower-symmetry geometry with a dipole moment. b) Experimental setup. THz field–induced lowering of the STO crystal symmetry is observed using 800-nm probe pulses that are partially depolarized (terahertz Kerr effect, or TKE) and which are partially converted to the second harmonic frequency (THz field–induced second harmonic, or TFISH).[132]

schematic of movement of the ions from the initial position towards their position in the new phase due to the terahertz excitation of the soft phonon mode. Figure 3.7b is the illustration of the experiments (THz field–induced second harmonic (TFISH) generation spectroscopy and THz field–induced optical birefringence (THz Kerr effect, or TKE) spectroscopy) performed by the authors using single-cycle THz pump pulses and time-delayed optical probe pulses.

Li et al. [132] has observed that the resonant terahertz pumping of the FE soft mode results in a nonoscillatory SHG signal which rises in a highly nonlinear fashion as a function of the field strength. The evolution of the signal has been linked to the growth of dipole ordering and hence, the emergence of the collective FE phase. The coherent oscillations in the SHG traces and optical depolarization signals have been attributed to the excitation of anti ferro-distortive(AFD) and FE mode in the ferroelectric phase of STO. Moreover, the terahertz field dependent growth of the multiple vibrational modes reveals the anharmonic coupling with the soft phonon mode and the change in lattice symmetry. These experimental observations have been also reproduced by simulating the interaction of resonant single-cycle THz pulse on the low-temperature quantum paraelectric state of $SrTiO_3$ using time-dependent lattice Schrödinger equation based on first-principles calculations[133].

3.2.4 Predictions in Cavity Engineering

The ferroelectricity in $SrTiO_3$ is strongly related to the collective behaviour of the ions in the FE soft mode. The strong light matter interaction can be exploited to alter these collective behaviours in order to give rise to new stable states. In the recent year, Latini et al. [36] theoretically proposed that this can be realized by embedding a bulk film of tetragonal $SrTiO_3$ inside a dark optical cavity with a dielectric medium resulting in the stabilization of

a ferroelectric photo ground state. In this approach, a ferroelectric state has been plausible even without driving the system out-of equilibrium using intense lasers.[132]

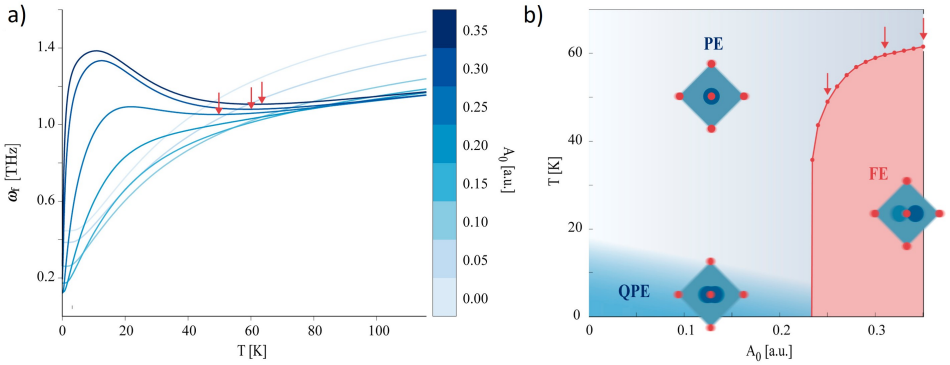

Fig. 3.8 **Revised Phase Diagram of $SrTiO_3$ inside Cavity.** a) FES mode frequency as a function of lattice temperature at different cavity coupling strengths (cavity frequency= 3 THz). The minima of the curves, marked with red arrows, are used to identify the phase boundaries in b. b) The microscopic phase diagram of SrTiO3 inside the cavity.[36]

The cavity can be used as an efficient tool to trap the photons in to a confined space and hence increases the light matter coupling. The off-resonant dressing of the STO lattice modes with the cavity photons results in an enhancement of the effective mass of the ions, slowing them down and hence reduces the quantum fluctuations. So, the cavity effectively localizes the system, reducing the hopping between the two states where the Ti and O atoms have a finite positive or negative displacement. This will result in spontaneous symmetry breaking and localizes the FES mode in one of the two wells. In addition, the lattice expansion was also reported by increasing the coupling strength with the cavity photons. This will give rise to deepening of the potential energy double wells and hence enhances the localization of the FES mode. These two localization effects leads to the formation of a macroscopic polarization inside the cavity, typical of the ferroelectric phase.

The results reveal that ferroelectricity can be achieved for a wide range of cavity photon energies and the effect of the cavity is larger in the off-resonance case. The authors point out that the hybridization between the ferroelectric mode and the cavity photons above a critical light matter coupling strength results in the softening of the FE mode indicating the instability to a ferroelectric state. This can be seen in Figure 3.8a[36] and the minimum of the FES mode frequency can be identified as the phase transition temperature from paraelectric to ferroelectric state. This results provide a revised phase diagram(Figure 3.8b[36]) inside cavity for paraelectric to ferroelectric transition in STO, with the cavity coupling strength as a new dimension. In a similar geometry, but with a different coupling mechanism Ashida et al. [37] has discussed the ferroelectricity of STO in a cavity environment. They emphasizes on coupling between photons, phonons and plasmons in a system consisting of paraelectric STO embedded between cavity mirrors and develops a theoretical model based on quantum light-matter interaction to control its equilibrium state.

4

Experimental Setup and Methodology

As described in the previous chapters optical cavities play a crucial role in enhancing light matter interaction to control the properties of the materials. In order to analyze the hybridization of different fundamental excitations like phonons and magnons with cavity mode it is important to develop a cavity assembly with tunable cavity resonance in the terahertz regime. In the first section of this chapter, we present the tunable cryogenic cavity assembly that has been developed in order to study light matter coupling in the terahertz frequency range[27]. This section of the chapter is adapted from [27].

The second part of the chapter explains the terahertz transmission setups employed in the experiments present in this thesis. The characterizations were done using single cycle terahertz pulses generated from two different sources. Firstly, transmission measurements were performed using a photo conductive antenna(PCA) based broadband time domain terahertz spectrometer. The second time domain terahertz setup concerns the production of high intense terahertz pulses through the optical rectification in a $LiNbO_3$ crystal in order to probe the nonlinear responses of the materials. We report also the characterization of the non-linearities emerging from the experimental setup.

4.1 Cavity Assembly

4.1.1 Optical Cavity Design

Figure 4.1 depicts the detailed schematic of the tunable cryogenic terahertz cavity. The built in cavity assembly consists of two cryo-cooled mirrors contolled by piezo actuators (N472-11V, Physik Instrumente). The actuators has total travel range of 7 mm and a minimum incremental motion of 50 nm with a designed resolution of 5 nm. Each cavity mirrors are controlled by three piezo actuators which ensures independent alignment of mirrors horizontally and vertically and a simultaneous motion of the three piezos results in rigid translation of the whole mirror. This independent control of mirror position with piezoelectric mechanics makes it possible to tune the cavity length and sample inside the cavity. The

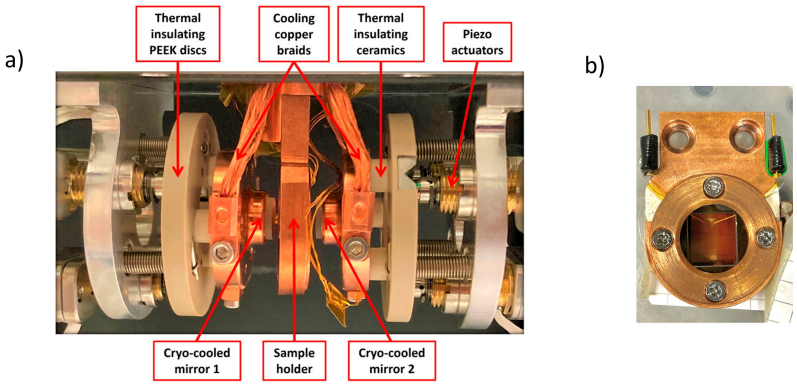

Fig. 4.1 **Terahertz cavity assembly** a) Cryogenic terahertz cavity assembly with description[27]. b) Sample mount with STO mounted between the Si_3N_4 membranes. Thermocouple used to measure the sample temperature is also shown.

tunability of the cavity length sets the resonant frequency of the cavity fundamental mode and the tunability of the sample position inside the cavity allows to maximize the coupling of the cavity photons with the targeted excitation, since the coupling energy scales with the absolute cavity field [16]. The cavity mirrors are mounted on copper holders which are cryo-cooled by means of copper braids connected directly to the cold finger of the cryostat. The functional range of the piezo actuators are 283-313 K, which makes it necessary to thermally decouple the piezo actuators from the mirror mounts. This has been achieved by placing a PEEK disc on which the actuators actually act and three ceramics cylinders between the piezo actuators and copper mirror holders. These materials are thermal insulators, and they have a low thermal expansion coefficient in the operational temperature range of the cryostat (10 K -300 K). These features ensure the mirrors to be thermally insulated as well as alignment stability of the cavity in the operational temperature range. In [27], we have shown that our setup has been proven to work efficiently in tuning the cavity length at cryogenic conditions.

For the THz experimental purpose, the cavity assembly is mounted on a flow cryostat which is supported by a mechanical assembly allowing for the movement of the whole sample in the x, y and z directions. The vacuum conditions are achieved by enclosing the setup in a vacuum chamber with two crystalline quartz windows of two mm thickness enabling the transmission studies in the terahertz range. A pressure in the range of 10^{-6} mbar at room temperature and 10^{-7} mbar at cryogenic temperatures were reached by pumping the chamber with a turbo pumping system (Pfeiffer Hi-Cube). The temperature of the cold finger has been read and controlled by a feedback circuit consisting of a cryogenic silicon diode and a temperature controller.

4.1.2 Fabrication of Cavity Mirrors

The cavity semi-reflecting mirrors were fabricated by evaporating a thin bilayer of titanium-gold (2-15 nm) on a 2 mm thick crystalline quartz substrate, resulting in a transmission amplitude of 10% across the THz spectral range in the experiment with no apparent spectral features. In detail, the deposition of the thin film coating has been achieved by classical E-beam evaporation. The substrates were first cleaned using standard procedure

based on RCA-1 ($NH_4OH - H_2O_2 - H_2O$ 1:1:5, 75^0 C, and 10′), rinsed by de-ionized (DI) water, and dried under N_2 blow. Right before the transfer in the evaporator chamber, the substrates were treated by oxygen plasma (P:20 W, B:50 V, and t:1′). The first 2 nm thin layer of titanium was used to increase the adhesion of the following gold layer. The deposition rate for the titanium layer was ~ 0.1 Å/s, while the gold was deposited at a rate of ~ 0.4 Å/s. At these deposition rates, we estimated an error in the film thickness of ~ 5 %, which translates in a 0.1 nm error for the 2 nm titanium film and 0.5 nm error for the 15 nm gold film.[27]

4.1.3 Sample Mount

The sample is mounted between the semi-reflecting mirrors in a copper sample holder which is connected directly to the cold finger of the cryostat and sealed between two silicon nitride membranes (LP-CVD grown) with a window size of 11 x 11 mm^2 and a thickness of 2 µm. A strontium titanate sample mounted between the silicon nitride membranes are shown in Figure 4.1b. The membranes are supported by a 13 x 13 mm^2 silicon frame with a thickness of 500 µm. The terahertz transmission spectra and transmitted terahertz pulse(inset) of the Si_3N_4 membranes are shown in Figure 4.2a which clearly shows that the membranes are transparent and do not have any spectral features in the THz frequency range.

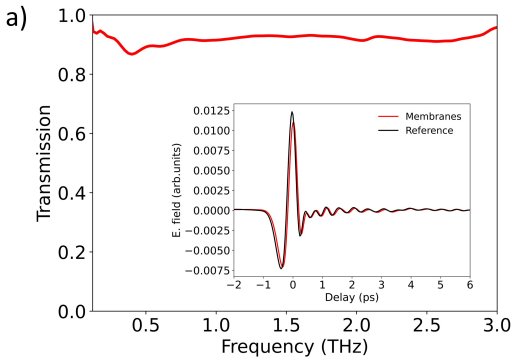

Fig. 4.2 **Characterization of the Si_3N_4 membranes** a) Transmission of the Si_3N_4 membranes with THz fields in the inset (THz source: Photoconductive antennae (PCA)).

4.1.4 Temperature Measurement of the Membranes

Figure 4.3a and Figure 4.3b shows the finite-elements simulations performed using the COMSOL MULTIPHYSICS software to gain information about the membrane's thermal profile in the freespace configuration. The simulation has been done in the assumption that the membrane's edges are at the same temperature of the cold finger (T_{cf}=180 K). The thermal profile implies that the actual temperature at the center of the membranes will be different from the cold finger temperature due to the high thermal impedance of the Si_3N_4 membranes. Hence, it's important to measure the actual temperature of the sample embedded between the membranes. The temperature of the membranes and the sample has been measured by sealing a home-made 20 µm Cr-Al junction between the membranes.

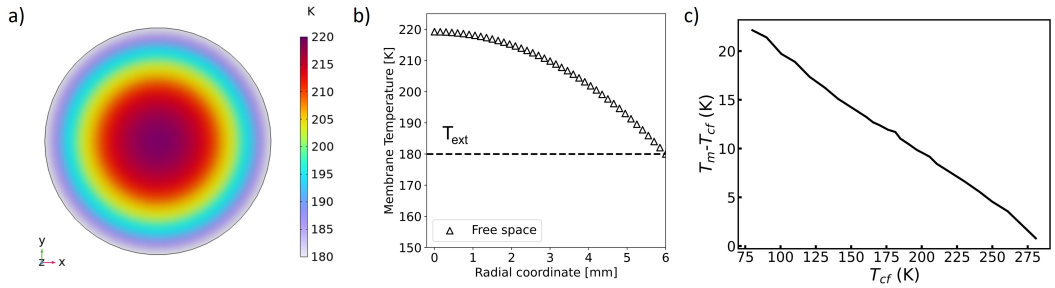

Fig. 4.3 **Characterization of Membrane's temperature** a) Simulated 2D temperature profile of the membrane in free space. b) Radial dependence of the membrane's temperature held in free space. The cold-finger temperature has been set at T_{cf} = 180 K.[134] c) Deviation of temperature at the center of the membranes (T_m) measured using thermocouple as a function of cold finger temperature (T_{cf}) inside the membranes

Figure 4.1b shows the thermocouple sealed between the membranes in order to measure the temperature of $SrTiO_3$. Figure 4.3c shows the deviation of the temperature of the membranes(T_m) in the free space scenario as a function of cold finger temperature(T_{cf}). In order not to have offsets in the temperature readout, all the wires connecting the junction to the output of the cryostat head were made of Cr and Al of ~ 120 µm. The only discontinuity point is represented by the gold male-female connectors at the output of the sample holder which, as we verified, gives no temperature discrepancy.[134]

4.2 Terahertz Time Domain Spectroscopy

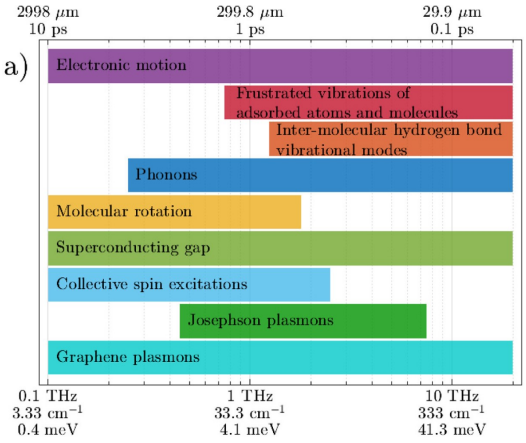

Fig. 4.4 **Terahertz applications and sources.** a) Fundamental excitations in solids and molecular systems in the THz region. (Figure is taken from [135])

Terahertz spectroscopy has gained significant attention recently due to the application of terahertz waves in ultrafast condensed matter physics, material science, chemistry, biology, medical diagnostics, high bandwidth short distance communication/data transfer, security, defense and its non-destructive, non-ionizing material evaluation[136]. The Tera-Hertz (THz = 10^{12} Hz) frequency region of the electromagnetic wave spectrum (100 GHz to 10 THz) occupying the middle gap between microwaves and infrared waves is known as

terahertz gap[137, 138]. The lesser energy(meV scale) of the terahertz waves makes it non-ionizing and an efficient tool to study and drive the low energy excitations in the materials. These excitations include phonons, plasmons, spins, intersubband transitions, excitons, macromolecular vibrations and molecular rotations. In the field of condensed matter physics, terahertz spectroscopy has proven to be efficient in studying rotations and vibrations in molecular systems, driving phase transitions and related changes in material characteristics, and probing and controlling quasi-particles and collective excitations in solids[135]. Various collective excitations of the materials lying in the terahertz region are shown in Figure 4.4.

The main challenges in the field of terahertz spectroscopy were the unavailability of efficient terahertz sources and detectors as the frequency is too high to make use of conventional electronic detectors. In the last decade there has been significant advancement in the efficient terahertz sources and detectors resulting in considerable surge in the research on the application of terahertz waves. The various techniques to generate terahertz waves range from photo conductive switch [139, 140], optical rectification in nonlinear crystals like ZnTe[141, 142] ,GaSe[143], $LiNbO_3$[144–146], DAST[147] and HMQ-TMS[148, 149], air plasma generation[150, 151], terahertz quantum cascade lasers[152] and accelerated electron bunches[153–155]. The mechanism behind terahertz detectors is the inverse of the one used in the terahertz sources. The most common terahertz detection techniques are based on unbiased photo-conductive switches[156], electro-optic sampling[157] and THz air breakdown coherent detection (THz-ABCD)[158].

Terahertz spectroscopy is advantageous in providing information on the amplitude and phase simultaneously compared to conventional Fourier Transform Infrared Spectroscopy (FTIR). Materials can be characterized in THz transmission/reflection geometry. The terahertz waves reflected/tramsmitted from the material can be evaluated in the frequency domain to study light matter interaction using Maxwell's equation. More details on the terahertz sources employed in the linear and nonlinear terahertz transmission spectrometers and the extraction of optical constants from the terahertz transmission are included in the following section of the chapter.

4.2.1 Broadband Terahertz Transmission Spectrometer

Terahertz Source: Photoconductive Antenna

The first design of a photoconductive antenna(PCA) has been proposed by Auston [159] where they have bombarded an antenna structure fabricated on an Ar - ion irradiated Silicon on Sapphire substrate with sub - picosecond laser pulses to generate radiation pulse. This is the first version of the photo-conductive antenna design which has undergone quite a bit of change in design, however the basic idea remained the same. The PCA consists of DC-biased metallic electrodes deposited on a photoconductive substrate. A detailed schematic of the PCA and the terahertz generation is shown in Figure 4.5. When we incident an optical pulse on the antenna gap photocarriers are generated as the optical pulse is absorbed. The concentration of this photo carriers(red curve in Figure 4.5) is proportional to the optical pulse. The DC bias applied on the electrodes results in the acceleration of the photo carriers and ultimately results in the emission of terahertz waves[160, 156]. The

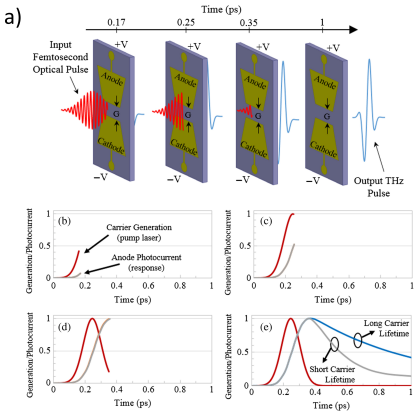

Fig. 4.5 **Illustration of pulsed THz generation in a PCA.** a) Femtosecond optical pulse propagates into the photoconductor, generates a transient photocurrent, which drives the antenna, and is re-emitted as a broadband THz pulse. Time profile of the carrier generation (red trace) and photocurrent in the antenna gap of photoconductive material (gray trace) for short-carrier lifetime and (blue trace) for long carrier lifetime.(Figure is taken from [139])

transient photocurrent(black curve in Figure 4.5) in the substrate has a rise time proportional to the rise time of the optical pulse as,

$$J(t) = N(t)e\mu E_{bias} \tag{4.1}$$

where N is the density of photocarriers, e denotes the elementary charge, μ is the mobility of electron, and E_{bias} is the bias electric field. Here, the photo-carrier density N is a function of time. This makes the decay time of the photo-current to be determined by the electrical properties of the substrate material rather than the temporal profile of the optical pulse. A shorter carrier lifetime(grey curve in Figure 4.5) will result in the recombination of photocarriers immediately after the optical pulse is fully absorbed[160, 156, 161]. In contrast, the substrates with longer carrier lifetime (blue curve in Figure 4.5) continues to have a photo-current even after the optical pulse is fully absorbed. This results in the broadening the photo-current pulse and hence the output terahertz pulse and reduce the overall THz frequency bandwidth[162]. Since the photo-current produced varies in time, it generates electromagnetic waves, whose electric field is determined by the relation [163, 164, 139]

$$E_{THz}(r,t) = -\frac{1}{4\pi\epsilon_0 c^2}\frac{\partial}{\partial t}\int \frac{J_s(r', t - \frac{|r-r'|}{c})}{|r-r'|}\,ds' \tag{4.2}$$

where, J_s is the spatially and temporally dependent surface current on the emitter surface, r is the spatial vector of the location of the THz field, r′ is spatial vector of the location of the surface current, which is integrated across the emitter surface ds′, c is the speed of light in vacuum, and ϵ_0 is the permittivity of the vacuum. The equation conveys that the power of the terahertz can be enhanced either by increasing power of the laser pulse or by using a high bias voltage. However, these are limited by saturation threshold and dielectric breakdown of the substrate.

The most commonly used substrate for the PCAs is gallium arsenide (GaAs)[165] due to its subpicosecond carrier lifetime, high carrier mobility and a band gap of 1.44 eV, which

allows it to be pumped above the band gap with Ti:sapphire lasers. Nevertheless, the intensity of the terahertz field is limited by the maximum bias field that can be applied due to low breakdown field. Eventhough, high bias fields have been used in low-temperature gallium arsenide (LT-GaAs) PCAs[166–168, 166, 169], such high fields are only possible with small (10 μm) gap sizes. There has been efforts to overcome these limitation by using wide band gap semiconductors such as diamond[170] , ZnO[171], ZnSe[172, 173], GaN[174] (band gap > 3.1 eV) and ZnSe (band gap:2.7 eV) which comes with a requirement of exciting the substrate with higher harmonics of a Ti:sapphire laser.

The THz emitter employed in the experiments presented in this thesis is fabricated on a semi-insulating GaAs substrate by depositing the metal electrodes having an inter-digitated finger-like structure. Each electrode is ~ 1 cm long and 10 μm wide. The gap between two nearby electrodes, which is also the active region, is 10 μm. The total area of the emitter is 1 × 1 cm^2. Due to such a narrow electrode gap, a bias of just a few volts on the electrodes creates an electric field of the order of a few kV/cm in the active region. Now, photo-excitation of the active regions creates charge carriers in GaAs, which accelerate due to the presence of an applied electric field and emit THz radiation having polarization parallel to the applied electric field. To avoid the destructive interference of THz radiated from two neighbouring active regions, each alternate active region is covered with a metallic layer to avoid the photo-excitation and, hence, out-of-phase THz generation from those regions.[27]

Terahertz Detection: Electro-optic Sampling

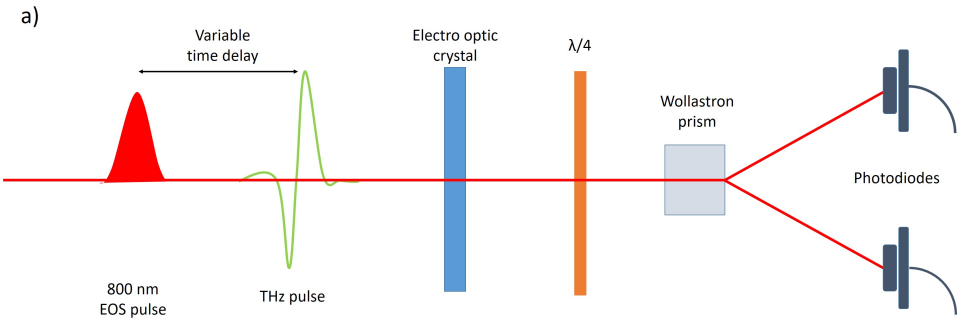

Fig. 4.6 **Schematic of electro-optic detection** a) Detailed schematic layout of electro-optic detection used in the experiment. Probe pulse is swept over the THz pulse in time using an optical delay stage. THz induced birefringence on EO crystal gives the time domain profile

As we discussed before, the small pulses of the order of 10s of femtoseconds cannot be detected using conventional electronic detectors. As the pyroelectric and bolometer detectors do not give the frequency responses they can't be used for the spectroscopic purposes. The electro-optic effect is a technique that has been borrowed from the field of photonics for the time domain detection of terahertz pulses. A schematic of the electro-optic sampling is shown in Figure 4.6. The electro optic sampling is based on the nonlinear optical effect called pockel effect in non-centrosymmetric materials like ZnTE[175] or GaP[176] exhibiting χ^2 susceptibility[177]. The terahertz electric field induces a change in the refractive index of the material along the polarization direction of the incident field creating a birefringence on the electro-optic crystal. Electro-optic sampling makes use of an ultrafast optical pulse

with pulse width much shorter than the terahertz pulse. This makes the electric field of the THz pulse to be treated as quasi-DC field and the optical probe to be considered as a gate pulse. The optical pulse is time delayed with respect to terahertz pulse and when the optical pulse overlaps with terahertz pulse spatially and temporally on the EO crystal the terahertz field induced birefringence will modify the polarization of the optical pulse. This change in the polarization will be proportional to the terahertz electric field. As we scan through the delay stage of the probe, the optical readout pulse sweeps through the terahertz pulse and the time domain terahertz electric field can be mapped from the modification of the probe pulse polarization. The degree of depolarization of the optical probe pulse can be measured using the polarization sensitive optical setup consisting of quarter wave plate, wollastron prism and a pair of photodiodes. The vertical and horizontal polarization components of the probe pulse are balanced by a quarter-wave plate, separated by the Wollaston prism, and detected by a pair of photodiodes. In the presence of terahertz field the photodiodes have an unbalanced signal due to the elliptical polarization of the probe pulse after the quarter wave plate. The difference in the intensity between two photodiodes are related to the terahertz electric field through[178, 179]

$$E_{THz} = \frac{\Delta I}{I}\left(\frac{\lambda}{2\pi n^3 r_{41} d}\right) \tag{4.3}$$

where λ is the wavelength of the probe pulse, n is the refractive index of the electro-optic crystal at the probe pulse frequency, d is the thickness of the electro-optic crystal, r_{41} is the electro-optic tensor component and $\frac{\Delta I}{I}$ is the degree of depolarization measured from the intensities on the two photodiodes.

Geometry of the Terahertz Spectrometer

The layout of the built THz transmission spectrometer is shown in the Figure 4.7a. Ultrashort laser pulses (50 fs pulse duration and 745 nm central wavelength) from a commercial 50 kHz pulsed laser + Optical Parametric Amplifier (OPA) system (Pharos + Orpheus-F, Light Conversion) are split into two to form an intense optical beam for THz generation (6 μJ/pulse) and a weak readout pulse (< 100 nJ/pulse) for time-resolved Electro-Optical Sampling. Single-cycle THz pulses are generated via the acceleration of the photoinduced carriers in a large-area GaAs-based photoconductive antenna (PCA). The acceleration of the free carriers induced by the pump is achieved by biasing the PCA with a square-wave bias voltage (V_{bias}) triggered with the laser at a frequency of 1.25 kHz. We employed a biasing square wave with a voltage peak of 8.0 V and a 50 % duty cycle. For an efficient THz generation using 6 μJ pump pulse energy, an area of around 6 mm diameter on the 1 cm^2 large emitter is illuminated using a collinear pump beam. Since the diameter of the excitation area is comparatively much larger than the THz wavelength, the radiated THz beam has a similar wavefront as the pump beam on the emitter and, hence, follows the same beam path as the pump beam.[27]

The emitted collimated THz beam is then focused on the sample mounted inside the cavity, which is placed in the focal plane of two off-axis parabolic mirrors (OPMs). The THz field and the readout pulse are then combined and focused on a 0.5 mm ZnTe crystal, which acts as the electro-optic crystal. After the electro-optic crystal, the probe beam, variable

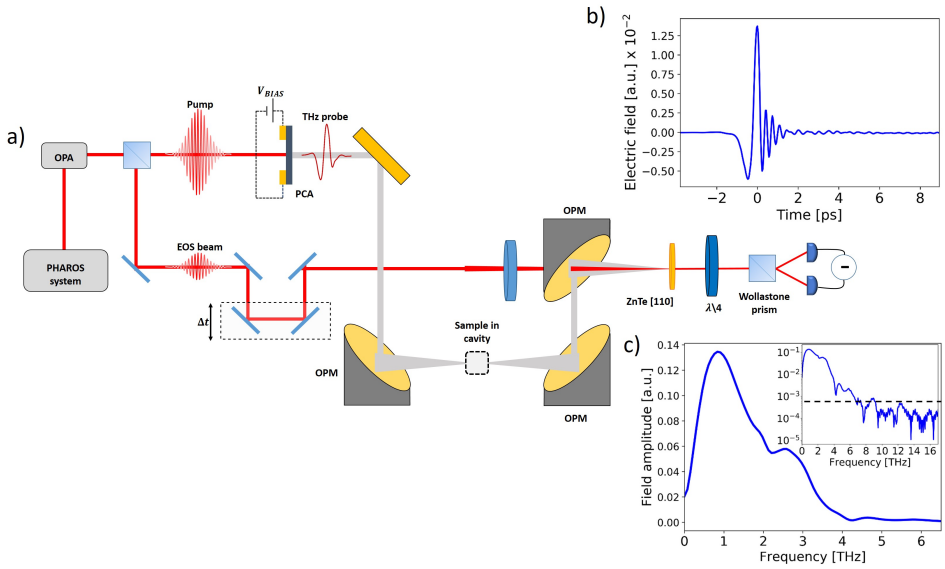

Fig. 4.7 **Terahertz time-domain spectrometer** a) Schematic layout of the Terahertz time-domain spectrometer. OPA: Optical Parametric Amplifier, PCA: Photo-Conductive Antenna, TS: Translation Stage, OPM: Off-Axis Parabolic mirror, λ/4: Quarter-wave plate. b) Single-cycle THz field generated by PCA and detected through Electro-Optic Sampling (EOS) in a 0.5 mm ZnTe crystal. c) Fourier transform of the THz field in Figure 4.7b. In the inset, the Fourier spectrum is plotted in logarithmic scale to highlight the spectral content of the THz field up to 6 THz. The black dashed line in the logarithmic plot marks the spectral noise level. Figure is taken from [27]

delayed in time through a translation stage (TS), is analyzed for its differential polarization changes induced by THz in the ZnTe crystal, which maps the time evolution of the ultrafast THz field. This is carried out by standard Electro-Optic Sampling (EOS), by splitting the two probe polarizations with a Wollaston prism and measuring the differential intensity recorded on a pair of photodiodes. The resulting differential signal is then detected using a lock-in amplifier (SR830, Stanford Research System) referenced at the frequency of the bias voltage (V_{bias}). We estimated the signal to noise ratio of the detected THz field to be 4.6 × 10^4 and the temporal phase stability to be < 30 fs. The entire system is purged with nitrogen to eliminate THz absorption coming from the water vapour in the ambient atmosphere. We show in Figure 4.7b the measured electric field of the generated THz pulse and its calculated Fourier spectrum (Figure 4.7c). As shown, the input field is, indeed, a nearly single-cycle THz pulse with the spectral content reaching 6 THz, as highlighted in the logarithmic scale plot in the inset of Figure 4.7c.[27]

4.2.2 Nonlinear Terahertz Spectrometer

Terahertz Source: Tilted Pulse Front Method

Optical rectification has been a reliable source of intense terahertz pulses since 1985[180] exploiting the second order nonlinear processes in non centrosymmetric media. The polar-

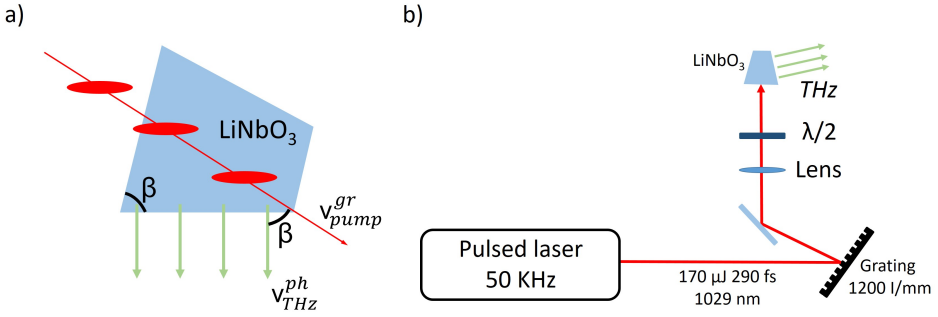

Fig. 4.8 **Schematic of THz generation from $LiNbO_3$ crystal**. a) Specially cut $LiNbO_3$ prism with cut angle same as the tilt of the 1029 nm inside the crystal ($\beta = 63.58°$). b) Tilted pulse front generation of high energy terahertz pulses. Incoming optical pulse is tilted by a diffraction grating. $\lambda/2$ is used to flip the polarization to be parallel to the optic axis of $LiNbO_3$ crystal.

ization(P) of a nonlinear medium exposed to high electric field can be described as[177, 181]

$$P_{NL} = \varepsilon_0(\chi^{(1)}E + \chi^{(2)}E^2 + \chi^{(3)}E^3 + \ldots) \tag{4.4}$$

Here ε_0 is the vacuum permittivity, and $\chi^{(n)}$ is the n^{th} order susceptibility of the material. In the Equation 4.4 the second term can be used to describe the induced second order nonlinear polarization density in materials lacking inversion symmetry. If the driving field has atleast two frequency components ω_1 and ω_2 this nonlinear polarization density will be a sum of frequency components 0, $2\omega_1$, $2\omega_2$, $\omega_1 + \omega_2$ and $\omega_1 - \omega_2$. Here the component which describes induced polarization at difference frequency will be the basic principle behind the terahertz generation through optical rectification. Hence the terahertz waves can be seen as difference frequency generation from all the spectral components of a laser pulse. The source of electromagnetic radiation is the second order time derivative of the nonlinear polarization density[181].

$$E(t)_{THz} \propto \frac{\partial^2 P_{-}(t)}{\partial t^2} \tag{4.5}$$

where $P_{-}(t)$ is the sum of induced polarization densities from the difference frequency generation. The temporal shape of this single-cycle electromagnetic pulse will be the derivative of the temporal shape of the pump laser pulse intensity. So the pump pulse in the range of hundred femtoseconds can give rise to single cycle terahertz pulses.

For nonlinear terahertz spectroscopic studies, it is important to have terahertz sources that generates terahertz fields on the order of several kilovolts per centimeter(kV/cm) to megavolts per centimeter(MV/cm). The terahertz field strength can be increased either by choosing materials with high conversion efficiency or by increasing the pump pulse intensity. ZnTe[182], GaP and GaSe[183] are the most commonly used nonlinear crystal to generate terahertz waves using optical rectification. However, the low damage thresholds and low conversion efficiency make them not suitable for the nonlinear studies[184]. The crystals like $LiNbO_3$(LN)[185] can be advantageous in generating intense terahertz field due to its higher nonlinear coefficient and high damage threshold[186, 144]. But, the collinear velocity matching condition[182] necessary for the efficient generation of single cycle terahertz pulses cannot be reached due to the significant difference in the group index(n_{gr}) of the

laser pulse and the refractive index(n_{THz}) of the terahertz waves the inside crystal. This can be visualized using Huygen's principle for the wavefronts. So, in order to sum up the generated THz radiation in phase the laser pulse front has to be tilted by an angle γ which makes the THz wavelets generated at different points of the pump pulse propagation arrive at exit surface in phase and sum up to generate an intense single-cycle THz pulse. This is illustrated in Figure 4.8a and the technique is called tilted pulse front technique[187, 188]. The tilt angle(γ) can be calculated as[189, 190],

$$\gamma = \arccos\left(\frac{\nu_{THz}}{\nu_{gr}}\right) = \arccos\left(\frac{n_{gr}}{n_{THz}}\right) \tag{4.6}$$

Here the group index(n_{gr}) is[181]

$$n_{gr} = n - \lambda_0 \frac{dn}{d\lambda_0} \tag{4.7}$$

and the THz phase index(n_{THz}) is

$$n_{thz}(\nu_w) = A + B\nu_w^2 + C\nu_w^4 \tag{4.8}$$

where n is the refractive index, λ_0 is the central wavelength, ν_w is the frequency wavenumber and the A,B and C are the polynomial coefficients from [191].

In order to ensure a perpendicular entrance and exit of the pump pulse and terahertz pulse respectively from the LN crystal it is important that the LN prism to be cut specially to match the pulse front tilt angle to yield an efficient terahertz source. The tilting of the pump pulse front can be done by using a diffraction grating[145]. The grating equation is given by

$$\sin\theta_i = \frac{\lambda_0}{d} - \sin\theta_d \tag{4.9}$$

where θ_i is the incident angle, λ_0 is the central wavelength of the pulse, d the distance between the slits and θ_d the diffraction angle. To accurately calculate the diffraction angle, one must also consider the dependence of the tilt angle inside the crystal on the group index, as well as the magnification of the lens system used to image the tilt inside the crystal[145]. The magnification of the lens is chosen in such a way that the image of the grating coincides with the tilted pulse front inside the crystal for the most efficient generation[192, 145]. In these conditions the tilt angle(γ) is given by[193]

$$\tan\gamma = \frac{N\lambda_0\beta}{n_{gr}\cos\theta_d} \tag{4.10}$$

Here N is the grooves density of the grating. The polarization of the incident beam has to be horizontal before the grating (perpendicular to the grating's rows) to maximize the efficiency and is then changed to vertical by a half wave plate ($\lambda/2$) to match the orientation of the optical axis of the LN crystal. The optical rectification in LN crystal has been proven to be efficient in generating single cycle terahertz pulses in the range of 0.2-2 THz with an energy of 2 μJ[187]. The terahertz pulses with higher energy has been generated by increasing the pump pulse intensity to 0.43 mJ[194] and by cooling LN crystal[195]. The tilted pulse front

method has been also applied in other nonlinear crystals like gallium arsenide(GaAS)[196] to generate terahertz waves.

Geometry of the Nonlinear Terahertz Spectrometer

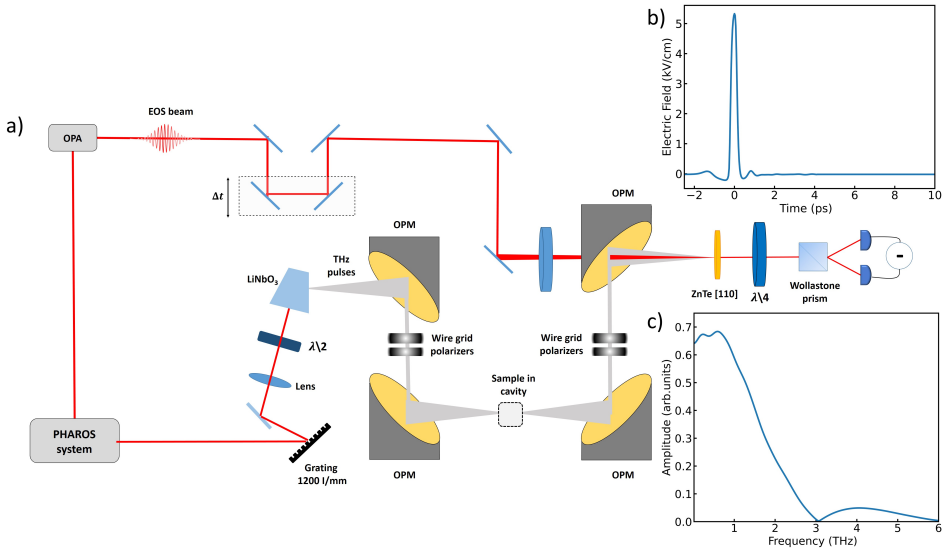

Fig. 4.9 **Nonlinear Terahertz spectrometer** a) Schematic layout of the Terahertz time-domain spectrometer in nonlinear geometry. OPA: Optical Parametric Amplifier, TS: Translation Stage, OPM: Off-Axis Parabolic mirror, λ/4: Quarter-wave plate, λ/2: Half-wave plate. Pair of wire grid polarizers are used to attenuate the electric field b) Single-cycle THz field generated from $LiNbO_3$ and detected through Electro-Optical-Sampling (EOS) in a 0.5 mm ZnTe crystal. c) Fourier transform of the THz field in Figure 4.9b.

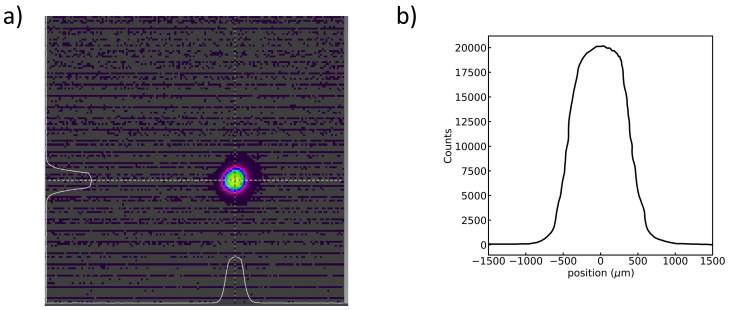

Fig. 4.10 **Image of THz focus** a) Image of focused THz spot taken with a Pyroelectric Array Camera positioned after the second parabolic mirror b) Gaussian profile of the cross section.

The schematic illustration of the nonlinear terahertz transmission spectrometer employed in this thesis is shown in Figure 4.9. The basic design of the nonlinear spectrometer is achieved by simply substituting the terahertz source with tilted pulse front technique on a $LiNbO_3$ crystal. In our setup, tilting of the optical pulse front is done by using a diffraction grating calculated using the Equation 4.9 and Equation 4.10. The grating surface (i.e. the tilted pulse) has been imaged inside the $LiNbO_3$ crystal (doped with 6.1% MgO), that has been cut to match the tilt angle of wavefront of the pump beam, resulting in a source of single cycle THz pulses. In the nonlinear terahertz studies performed in this thesis, the

$LiNbO_3$ crystal was pumped by 290 fs laser pulses at 1029 nm with 170 μJ per pulse energy from a commercial 50-kHz pulsed laser (Pharos, Light Conversion) as shown in Figure 4.8. The tilted-pulse-front setup has a 1200 lines/mm grating, which was imaged in a 2:1 demagnification ratio into the $LiNbO_3$ crystal. The pump pulse was incident on the grating at an angle 21.9^0 and diffracted at 59.3^0 as per Equation 4.10 and grating equation(Equation 4.9). The prism was cut at 63^0 to match the tilt angle(Figure 4.8).

The THz waves emitted from the LN crystal is then focused on the sample mounted inside the cavity using two off-axis parabolic mirrors (OPMs). The transmitted THz field was detected by electro-optic sampling using the same geometry explained in the broadband terahertz transmission spectrometer subsection 4.2.1. An image of the Terahertz at the sample position taken by a pyroelectric array camera (Pyrocam IIIHR), is shown in Figure 4.10a. Gaussian profile of the cross section (Figure 4.10b) reveal a THz focus size of less than 2 mm. The terahertz pulse energy measured at the focus by a pyroelectric detector (Gentec) was 12 nJ with terahertz conversion efficiency of almost 10^{-4}. When focused, a peak THz electric field of 5.3 kV/cm (calculated using Equation 4.3) were obtained, with usable frequencies extending until 3 THz. We show the electric field of the THz pulse in Figure 4.9b and its calculated Fourier spectrum in Figure 4.9c. In a nonlinear terahertz spectrometer, it is necessary to insert a pair of wire grid polarizers before the sample (WGPs are placed after the 1st OPM as shown in Figure 4.9a) in order to perform the THz field dependent studies on the sample. The electric field transmitted through the pair of polarizers(Malus's law) is given by

$$E = E_0 \cos^2 \theta \tag{4.11}$$

where, E_0 is the incident field and θ is the relative angle between the two polarizers. The second polarizer is fixed and the first polarizer is rotated to obtain THz fields that varies according to Equation 4.11 and to maintain a constant polarization on the sample. Another pair of wire grid polarizers were placed after the sample to eliminate the nonlinearity on the detection crystal for the measurements in the freespace.

4.2.3 Extraction of Terahertz Optical Properties

As mentioned before time domain terahertz technique(THz-TDS) can provide information about the amplitude and phase of the electromagnetic field. The reflection coefficient and the transmission coefficient of the sample in the frequency domain can be obtained from the THz-TDS measurements in reflection and transmission geometries respectively. This helps in extracting the frequency dependent dielectric function of material without using the Kramers-Kronig relations. Since the experimental setups in this thesis are in transmission geometry we will be discussing the procedures to obtain optical constants of the sample from the time domain terahertz pulse transmitted through the sample. The Figure 4.11a and Figure 4.11b shows the schematic of the propagation of the terahertz field with and without sample(100 μm thick STO sample at room temperature) and the corresponding temporal waveform of the terahertz field respectively. Then Fourier transform of this time-domain data gives the frequency dependent amplitude and phase of the transmitted THz wave

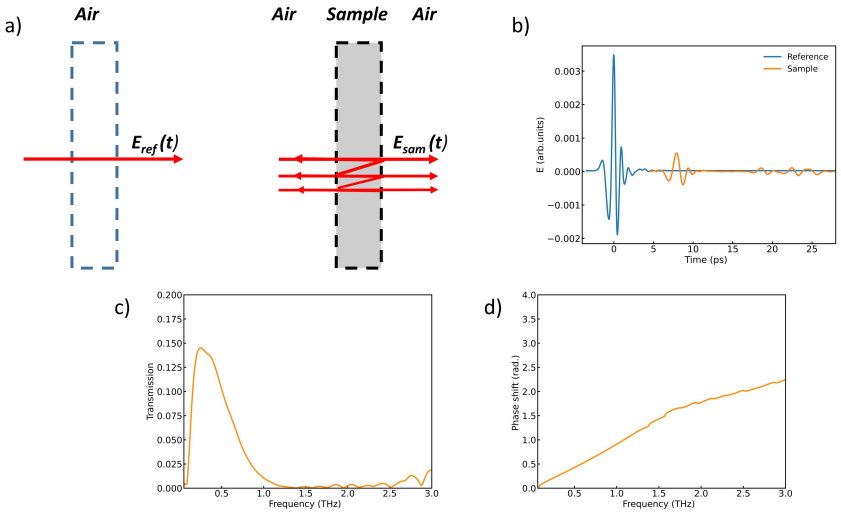

Fig. 4.11 **THz Transmission Analysis.** a) Schematic diagram of transmission from a sample. b) Time domain pulses measured with and without sample (In this case a 100 µm thick STO sample at room temperature is used). c) Amplitude and d) phase of the transmittance of the sample calculated by taking the Fourier transform of the terahertz pulses in Figure 4.11b

pulse and the complex transmittance of the sample can be calculated as

$$\tilde{T}(\omega) = \frac{\tilde{E}(\omega)_{sam}}{\tilde{E}(\omega)_{ref}} \tag{4.12}$$

The amplitude and phase of the transmittance of the sample calculated from Equation 4.12 is shown in Figure 4.11c and Figure 4.11d respectively. Assuming that the surrounding media is air, the transmission coefficient of the sample can be determined using Fresnel's equations as,

$$t_{as} = \frac{2}{\tilde{n}+1}, \quad t_{sa} = \frac{2\tilde{n}}{\tilde{n}+1} \tag{4.13}$$

where $\tilde{n}$ is the complex refractive index of the sample. If the pulse transmitted through the sample has echoes like the one shown in Figure 4.11a the complex transmittance(Equation 4.12) can be written in terms of refractive index as

$$\tilde{t}_s = \frac{\tilde{E}_{sam}(\omega)}{\tilde{E}_{ref}(\omega)} = t_{sa} \cdot t_{as} \cdot \exp\left(-i\frac{(\tilde{n}-1)\omega d}{c}\right)\left[1+\sum_{l=1}^{m} r_{sa}^{2l} \exp\left(-i\frac{2l\tilde{n}\omega d}{c}\right)\right] \tag{4.14}$$

$$= \frac{4\tilde{n}}{(\tilde{n}+1)^2} \exp\left(-i\frac{(\tilde{n}-1)\omega d}{c}\right)\left[1+\sum_{l=1}^{m}\left(\frac{\tilde{n}-1}{\tilde{n}+1}\right)^{2l} \exp\left(-i\frac{2l\tilde{n}\omega d}{c}\right)\right]$$

$$= T(\omega)\exp\left(-i\phi(\omega)\right)$$

here d is the thickness of the sample, c is the speed of light and $T(\omega)$ and $\phi(\omega)$ are experimentally obtained amplitude and phase of the transmittance. The Figure 4.11b shows a terahertz pulse that has been delayed by more than t=7 ps (t >> pulse width of THz) due to the propagation through the sample(STO). In this scenario, we can use the approximation for the optically thick samples and the Fabry Perot echoes can be neglected. By supposing

that the material is low absorptive(k << n) the transmittance can be expressed as,

$$T(\omega) = \frac{4n}{(n+1)^2} \exp(\frac{-k\omega d}{c}), \quad \phi(\omega) = \frac{(n-1)\omega d}{c} \tag{4.15}$$

where n and k are the real and imaginary part of the refractive index which gives

$$n(\omega) = \frac{\phi(\omega)c}{\omega d} + 1 \tag{4.16}$$

$$k(\omega) = -\frac{c}{\omega d} \ln\left(\frac{\rho(\omega)(n+1)^2}{4n}\right) \tag{4.17}$$

$$= \frac{c}{\omega d} \ln\left(\frac{4n}{\rho(\omega)(n+1)^2}\right)$$

The optical properties of a given medium can be described by the dielectric constant $\tilde{\epsilon}$, the optical conductivity $\tilde{\sigma}$, and the complex refractive index $\tilde{n}$, all of which are, in general, complex quantities:

$$\tilde{\epsilon} = \epsilon_1 - i\epsilon_2, \tag{4.18}$$

$$\tilde{\sigma} = \sigma_1 - i\sigma_2 \tag{4.19}$$

The frequency dependent complex dielectric function and conductivity of the sample can be obtained from the relation,

$$\tilde{n}^2 = \tilde{\epsilon} = \epsilon_\infty - i\frac{\tilde{\sigma}}{\omega\epsilon_0} \tag{4.20}$$

ϵ_∞ is the permittivity at infinite frequency, $\tilde{\epsilon}$ is the complex permittivity and $\tilde{\sigma}$ is the complex conductivity of the sample.

4.3 Experimental Setups Characterization

4.3.1 Characterization of the Optical Cavity

Cavity Resonance Characterization

The terahertz Fabry Perot cavity used in the experiments reported in this thesis is characterized by time resolved terahertz transmission spectroscopy. The major parameters of a cavity such as resonant frequency and quality factor can be determined directly from the transmitted terahertz field. The cavity losses has been minimized by aligning the cavity mirrors parallel to each other and perpendicular to the incident terahertz field. An optical beam has been send collinear to the terahertz waves to align the optical cavity. The normal incidence on both the mirrors of the cavity is achieved by making the reflected beam coincide with the incident beam. The mirrors are well aligned horizontally and vertically by moving the Piezo actuators. The reflections from the cavity are identified by observing variations in the time domain terahertz field as we adjusted the position of the entire mirror.

The trasmitted terahertz field from the empty cavity at two different cavity lengths are shown in Figure 4.12a. The first pulse transmitted through the cavity is followed by the

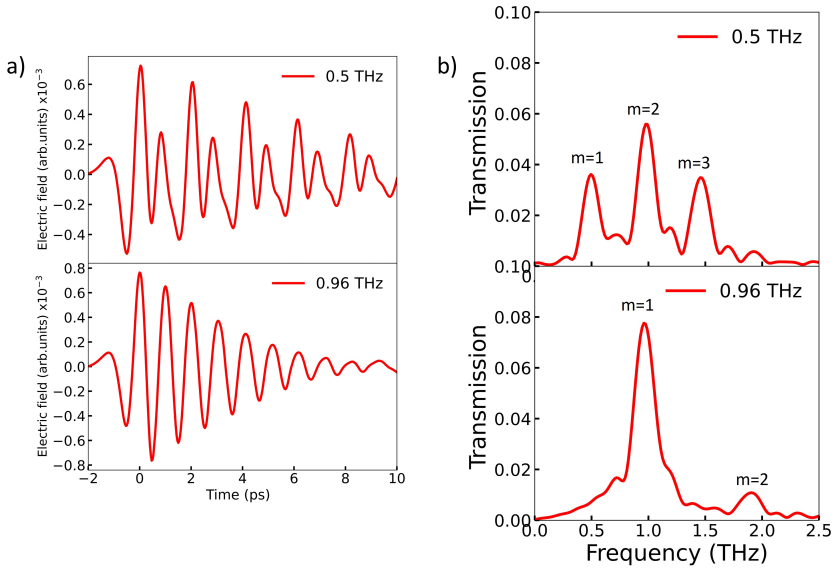

Fig. 4.12 **THz Characterization of Empty Cavity.** a) Trasmitted terahertz field from cavities with resonant frequencies 0.5 THz (Top) and 0.96 THz (bottom). Fields are measured with cavity mirrors at room temperature b) Amplitude of transmittance for transmitted terahertz pulses in Figure 4.12a. The fundamental resonance mode (m=1) and higher harmonics (m=2 & m=3) are marked in the figure. (THz source: $LiNbO_3$ crystal)

Fabry Perot reflections inside the THz cavity and the reflections are set by the round trip time of the cavity. The Figure 4.12b shows the amplitude of transmission calculated from the ratio of Fourier transformation of the terahertz field in Figure 4.12a and reference field. Fundamental frequency of each cavity is shown in the legend. In the spectra, Fabry Perot modes of the cavity is marked with the mode number(m). The frequencies of the modes are related to the cavity length as $\omega_c = m\frac{c}{2nL}$ where n is the refractive index of the medium inside the cavity and L is the cavity length. The bandwidth of the fundamental mode is related inversely to the time in which energy leaks out of the cavity and the quality factor of the cavity can be calculated as the ratio between the fundamental cavity mode and its bandwidth at a fixed cavity length which has been estimated as $Q \sim 4.9$. The quality factor of the cavity can be further improved by using cavity mirrors of higher reflectivity. However, as the THz TDS measurements were performed in the transmission geometry an optimal reflectivity had to be chosen in order to have good signal to noise ratio.

Calibration of Cavity Length Variation with Temperature Change

The experiments in this thesis have been performed in the temperature range of 80 K-295 K. The mirror mounts are directly connected to the cold finger. Hence, the change in the cold finger temperature affects the cavity length due to the thermal expansion of copper mirror mounts[197]. Because of this reason, it is important to develop a protocol to correct this thermal effects to perform temperature scans at a fixed cavity length.

Figure 4.13a presents temporal terahertz field from a 10 mm cavity at 295 K in which cavity length is determined from the round trip time of the reflection marked as cavity peak (first cavity reflection). The thermal evolution of this cavity reflection shown in Figure 4.13b

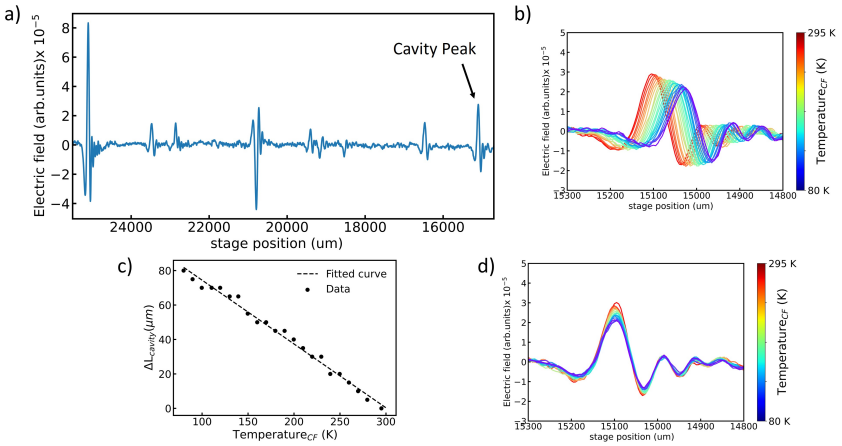

Fig. 4.13 **Temperature Calibration of Cavity Length.** a) Transmitted terahertz field from a cavity with cavity length 10 mm at 295 K. b) Cavity peak plotted for different cold finger temperature(T_{cf}) before calibration. Cavity length variation arises from the thermal expansion of mirror mounts. c) Change in the estimated cavity length (from the terahertz time domain pulse) as a function of cold finger temperature(T_{cf}). Dotted plot is the linear fit. d) Cavity peak at different cold finger temperature after calibration. The correction used here is $\alpha = 0.372\ \mu m/K$

reveals that the cavity length has been increased at low temperature resulting in a variation of the resonant frequency of the cavity. The change in the cavity length(ΔL_{cavity}) as a function of cold finger temperature(Figure 4.13c) shows that the cavity length has changed by 80μm by cooling down from room temperature to 80 K which will be highly evident and significant at higher cavity frequencies. The thermal expansion coefficient (α=0.372 $\mu m/K$) can be determined by fitting the data points with the function,

$$\Delta L_{cavity} = \alpha(295 - T_{CF}) \tag{4.21}$$

The coefficient obtained from the fit has been used as a correction factor to adjust the cavity length in the temperature scans by controlling piezo actuators through the labview program. The procedure has been proven to be efficient in fixing the cavity length over the whole temperature range (295K-80 K). The temperature scan after the correction is shown in (Figure 4.13d).

4.3.2 Nonlinearities in the Experimental Setup

Nonlinear effects like kerr effect, terahertz related kerr effect(induced by the second order optical nonlinear processes in noncentrosymmetric media) and two photon absorption observed in Zinc Telluride(ZnTe) crystals[198][199] have been reported to have strong influence on the terahertz generation. In addition, Terahertz field induced second harmonic generation[200] and nonlinear absorption features of the low frequency THz phonon mode[201] in ZnTe makes it necessary to understand the possible nonlinearities in the detection crystal in order to disentangle the non-linear effects of the detection to those of the sample.

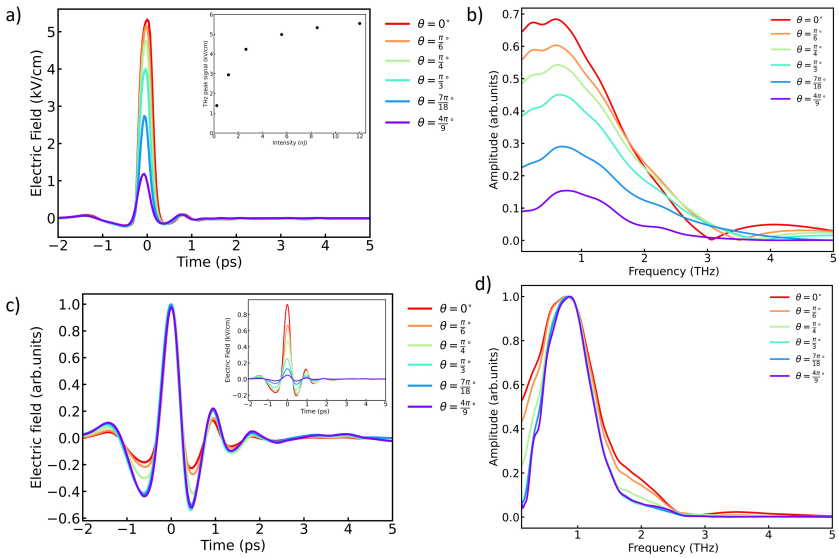

Fig. 4.14 **Non-linearity of the Detection Crystal.** a) Terahertz field from $LiNbO_3$ detected by ZnTe crystal altered by the wire grid polarizers. Field shapes are completely different due to the non-linearity. The peak to peak value against intensity(nJ) in the inset is not linear and saturates at higher intensities b) Amplitude of the FFT for the fields in Figure 4.14a. Spectral content distribution is not the same at different intensities c) The terahertz field (normalized to the peak) detected by ZnTe after placing a pair of wire grid polarizers almost perpendicular to each other before the detection crystal. The terahertz peaks are almost linear to the $\cos^2\theta$ (Malus's law). The fields are overlapping at lower intensities. d) The amplitude of FFT for the terahertz fields(normalized) after placing a pair of WGP before detection crystal

Firstly, the intensity of the terahertz generated from the $LiNbO_3$ crystal was attenuated using two wire grid polarizers and the temporal field was mapped using electro-optic sampling. The time domain of the terahertz field on the ZnTe and its Fourier transform is shown in Figure 4.14a and Figure 4.14b at different relative angle between the two polarizers. The terahertz electric field is saturating at higher intensities which is clearly visible in the THz peak to peak plotted against intensity in the inset of Figure 4.14a. Additionally, a terahertz field dependent effect was observed in the shape of the terahertz pulses resulting changes also in the spectra. This nonlinear effects can be possibly associated to the anharmonic vibrational potential of phonon modes in ZnTe[201]. In order to perform nonlinear terahertz spectroscopy measurements on the materials, it is important to eliminate the nonlinear effects of the detection crystal.

As an attempt to remove the nonlinear responses of the ZnTe, two wire grid polarizer were placed almost perpendicular between the sample and the detection crystal(Figure 4.9a). This helps in attenuating the THz intensity on the ZnTe crystal with out changing the incident field strength on the sample. The terahertz field and the Fourier transform under this condition are shown in Figure 4.14c and Figure 4.14d respectively. The fields are normalized on the peak in both time and frequency domain. Even though the THz peak saturation has been suppressed the changes in the terahertz pulse and spectra are still clearly visible. However, the THz fluence dependence is completely eliminated below a peak field of 0.25 kV/cm($\theta = \pi/3$ (Inset Figure 4.14c)). Since the detection crystal falls into the linear

regime below this field strength($\theta = \pi/3$) the reference fields at $\theta = 0, \pi/6$ and $\pi/4$ (In the free space) used in the nonlinear spectroscopy measurements are obtained by rescaling the terahertz field at $\theta = \pi/3$ using Malus's lawEquation 4.11.

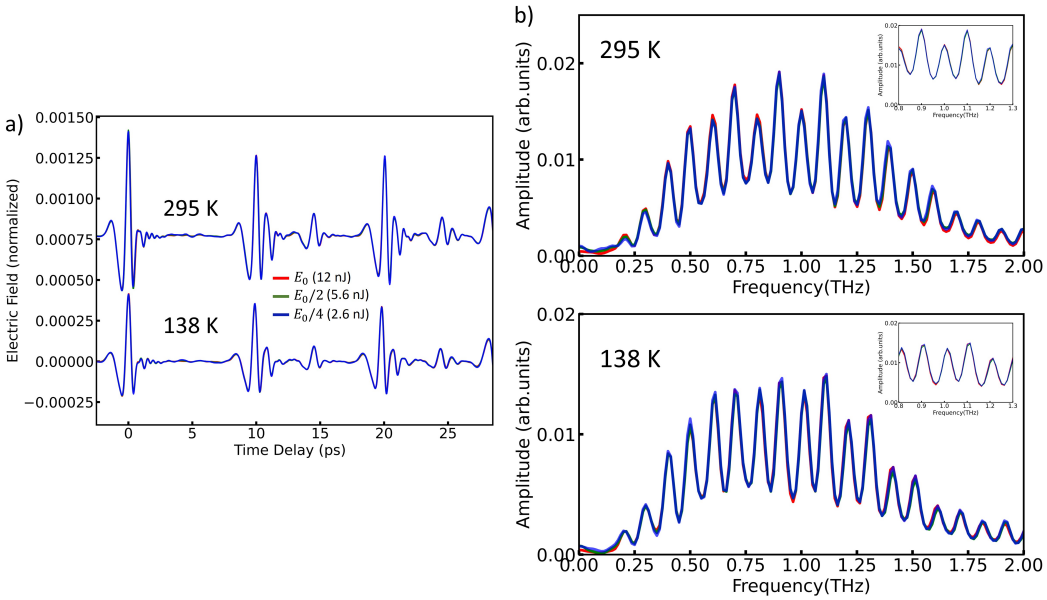

Fig. 4.15 **Nonlinear Studies on Empty Cavity.** a) Transmitted terahertz field from an empty cavity with cavity length 1.5 mm at different terahertz intensities for T= 295 K and T= 138 K. The terahertz pulses are normalized by $\cos^2\theta$ (Malus's law). b) Amplitude of the FFT for the fields in Figure 4.15a. The FFT is also normalized by $\cos^2\theta$ (Malus's law). The inset shows the FFT zoomed from 0.8 THz to 1.3 THz for better clarity

The nonlinear THz-TDS measurements in this thesis are performed in the conditions in which the nonlinearities of ZnTe crystal are eliminated. The fluence dependent terahertz transmission of empty cavity at T= 295 K and T= 138 K are shown in Figure 4.15. Since the transmitted terahertz field from the empty cavity is already in the linear regime of the detection crystal the measurements with the cavity has been performed by removing the pair of wire grid polarizers before the detection crystal in order to ensure good signal to ratio. Both the terahertz waveforms(Figure 4.15a) and the spectra(Figure 4.15b) are well overlapped after normalizing using Malus's law(Equation 4.11) for the polarizers at both temperature conditions. For better clarity, the spectra zoomed from 0.8 THz to 1.3 THz (frequency range in which nonlinearities are pronounced in the nonlinear studies given in chapter 7) are shown in the insets of Figure 4.15b. This indicates that the terahertz transmission responses from an empty cavity doesn't have any fluence dependence at the terahertz field strengths used in this thesis and the intensity of transmitted terahertz waves from the bare cavity is lower than the threshold for the nonlinearities in the detection crystal.

In conclusion, a tunable cryogenic cavity assembly efficient in studying the light matter interactions at the terahertz frequency range has been developed. The light–matter hybrids are characterized using broadband single cycle terahertz pulses generated from a photoconductive antenna. The nonlinear responses of the matter inside the cavity has been studied using a constructed nonlinear terahertz spectrometer based on tilted pulse front technique.

5

Signatures of Strong Light-Matter Coupling in Quantum Materials

5.1 Motivation

In the strong coupling regime, coherent exchange of energy between the light and the matter leads to the formation of hybrid states with energies that are different from the independent eigen states of the confined optical field and the emitter. This phenomenon is called Rabi splitting. And light matter hybrid states are termed as polaritonic states[202, 203]. Modification of the energy states of the system opens the possibilities to control fundamental properties like rate of chemical reactions[204] and the conductivity of organic semiconductors[205]. In addition, strong amplification of the Raman scattering signal from a strongly coupled system can be applied to design an optical parametric oscillator based on a Raman laser[206], and more efficient second and third-harmonic generation from the low polaritonic state is promising for nonlinear optics[207, 208]. Furthermore, the vibrational strong coupling with the phonons have been explored for its potential impact on phonon-assisted collective phenomena in quantum materials, including superconductivity[44], ferromagnetism[45] and ferroelectricity[37].

In this chapter, we are reporting our efforts to experimentally demonstrate the strong light matter interaction in $CuGeO_3$[27] and 1T-TaS_2 sample by coupling the cavity modes to the infrared(IR) active phonon modes. One of the most commonly used experimental way to detect strong light matter coupling is to compare the transmission spectra of the empty cavity and the material inside the cavity. Hence, the strong coupling phenomena has been demonstrated using broadband terahertz spectrometer described in subsection 4.2.1. The first section of the chapter documents the vibrational strong coupling regime in the $CuGeO_3$ crystal. The high oscillator strength of the optically-active phonon mode in $CuGeO_3$ enable to observe anticrossing behaviour, a distinctive feature of strong light matter coupling when the material is embedded in a resonant optical cavity.

In the second part of this chapter, we reveal the emergence of multimode vibrational coupling in the charge density wave (CDW) material 1T-TaS_2 due to the hybridization of fundamental mode of the cavity with the three CDW phonon modes. The screening of the

CDW phonons above the metal insulator phase transition temperature results in the closing of the multimode polaritons in the metallic phase. The temperature dependent terahertz transmission measurements across the first order phase transition shows the evidences of coupling between the cavity field and the free carriers across metal insulator phase transition resulting in the enhancement of cavity dissipation.

5.2 Strong Light Matter Coupling in $CuGeO_3$

5.2.1 Terahertz responses of $CuGeO_3$

$CuGeO_3$ is an insulating crystal belonging to the family of cuprates and it exhibits an orthorhombic crystal structure with space group Pbmm, consisting of chains of CuO_6 octahedra along the c axis interconnected by GeO_4 tetrahedra as shown in Figure 5.1[209]. The material undergoes a spin-Peierls transition at low temperatures(below 14 K) in which the one dimensional antiferromagnetic spin chain undergoes a transition to a nonmagnetic dimerized state[210–213]. This transition is driven by the interaction between the magnetic spins and the lattice vibrations or phonons.

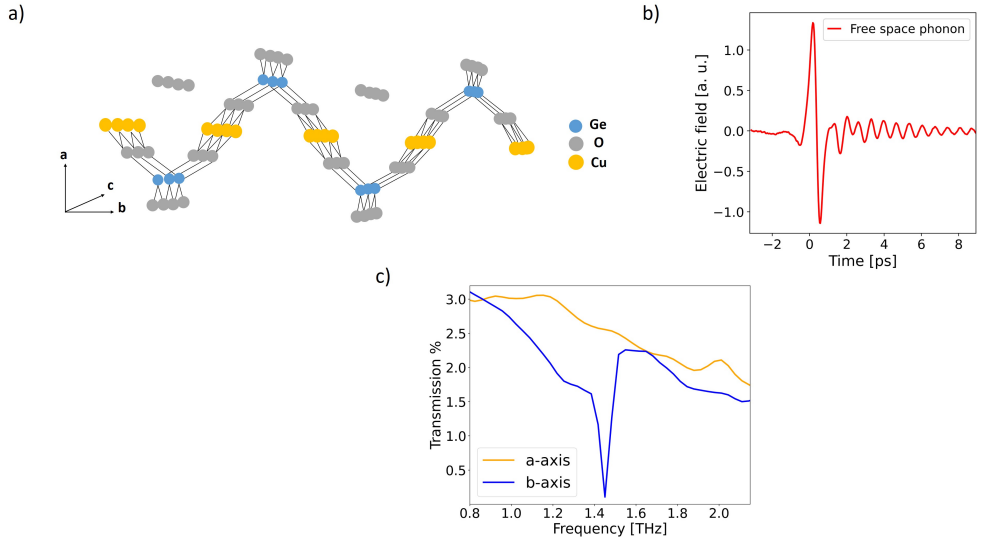

Fig. 5.1 **Terahertz response of $CuGeO_3$ sample** a) $CuGeO_3$ crystal structure in the normal phase. b) Transmitted terahertz field from a 20 µm thick $CuGeO_3$ sample along the b-axis (at 80 K). c) Comparison of transmission spectra of the $CuGeO_3$ along the b-axis and a-axis

Infrared reflectivity measurements have revealed distinct phonon modes along the b-axis and c-axis of the pure $CuGeO_3$ crystal. Phonons are detected at 5 THz, 15.8 THz and 21.5 THz when light is polarized along the c-axis and at 1.45 THz, 6.3 THz, 8.6 THz, 11.3 THz and 23 THz along the b-axis[209]. In the THz range employed in this setup, only the Cu-O infrared-active vibrational mode at 1.45 THz along the b-axis can be detected. This mode is associated with the rotation (accompanied by a slight internal distortion) of the GeO_4 tetrahedra around the axis defined by the oxygen sites and presents a B_2u symmetry. This strong Cu–O IR-active vibrational mode also shows a monotonic blue shift in the normal

phase from 14 K to 300 K with a line broadening due to phonon thermal population[209, 214]. Hence the temperature dependence of the linewidth and the high oscillator strength of the B_2u phonon makes $CuGeO_3$ a suitable candidate to study the emergence of light matter hybrid states in a resonant optical cavity.

The terahertz transmission measurements of the bare $CuGeO_3$ has been done in the open cavity configuration, i.e.,when the distance between the two mirrors is such that the fundamental cavity frequency lies far below with respect to the phonon frequency and the resulting transmission can be regarded as the freespace one with only a damping coefficient(~ 5% transmission) due to the semi-reflecting mirror absorption. Figure 5.1b shows the transmitted terahertz wave from a $CuGeO_3$ crystal of thickness 20 µm at 80 K when the terahertz electric field was oriented in the b-axis. The oscillation in the transmitted terahertz field can be attributed as the vibrational phonon mode in the b-axis (perpendicular to the magnetic chains). Figure 5.1c shows the frequency dependent terahertz transmission of the $CuGeO_3$ when the THz polarization was parallel to the crystal b-axis(blue) and a-axis(yellow). No spectral features were detected in the terahertz range along the a-axis, but a distinct absorption peak at 1.45 THz associated with the B_2u mode with a linewidth of γ_{phon} = 76 GHz (full-width half-maximum) was observed when the terahertz electric field was parallel to the b-axis.

5.2.2 Vacuum Rabi Splitting inside Optical Cavity

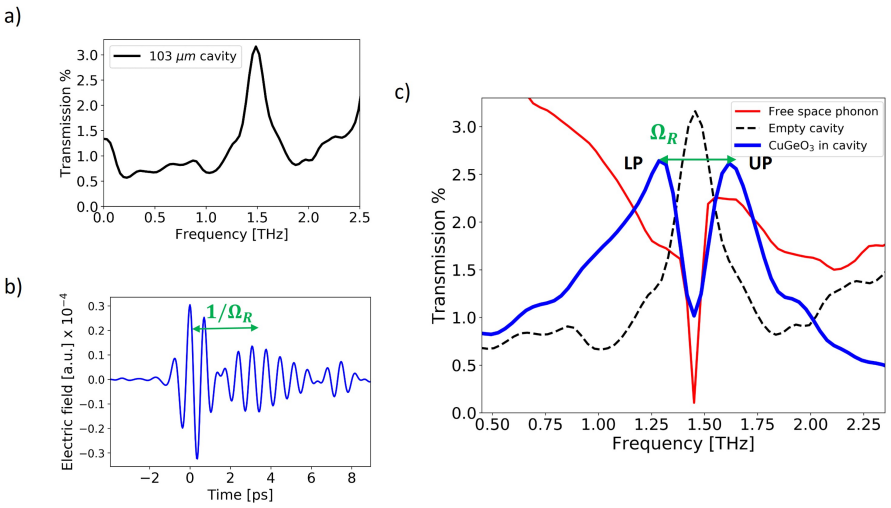

Fig. 5.2 **Resonant Light Matter Coupling of $CuGeO_3$ in a Terahertz Cavity.** a) Transmission spectrum of the empty cavity resonant with the phonon mode at 1.45 THz. b) Transmitted terahertz field from $CuGeO_3$ sample embedded inside the resonant cavity(obtained by filtering the region between 0.4 THz and 2.5 THz). c) Transmission spectrum of the light matter hybrid system(blue line) along with the spectral response of the bare cavity(black dashed line) and the freespace phonon(red line) (at T= 80 K)[27]

The strong coupling phenomena in $CuGeO_3$ crystal has been studied by placing the sample at the center of a Fabry Perot cavity resonant with the vibrational phonon mode at 1.45 THz. The spectral response of the bare cavity used in this studies is shown in Figure 5.2a. The estimated quality factor of the cavity at 80 K was, Q=6.3 obtained from the ratio between

the fundamental cavity mode (ω_{cav} = 1.45 THz) and its FWHM[1]. Shown in Figure 5.2b and Figure 5.2c are transmitted time domain terahertz field(obtained by filtering the region between 0.4 THz and 2.5 THz) and transmission spectra of the hybrid system at temperature, T=80 K. The spectral response of the bare cavity(black dashed line) and the $CuGeO_3$ in freespace(red line) are also shown along with the spectrum of the coupled system(blue line). The transmitted spectrum of the coupled system shows two distinctive peaks which are shifted in frequency with respect to the bare phonon and cavity resonance indicating the presence of two new eigen states. The spitting between this peaks, Ω_R=0.32 THz is greater than the linewidth of both the bare phonon and the cavity.

The coupling between a matter and cavity are determined by the photon decay rate of the cavity, γ_{cav}, the lifetime of the phonon, γ_{phon} and the coupling strength,g. Both γ_{cav} and γ_{phon} can be associated to the line width of the cavity and the phonon absorption respectively[18, 71, 49, 215]. The splitting in the spectral response of the coupled system reflects that the light matter coupling (g) has become faster than the dissipation processes and the system is in the strong coupling regime. This effect is called Rabi splitting and the two spectroscopically resolved peaks can be attributed as hybrid vibro-polaritonic states. The signatures of coupling between the phonon mode and the cavity fundamental mode can be observed also in the transmitted terahertz field(Figure 5.2b). This terahertz field exhibits an exponential decay modulated by periodic beating of period $1/\Omega_R$=3.1 ps instead of a single exponential decay as in the case of uncoupled phonon and bare cavity. This temporal beating is called coherent Rabi oscillations resulting from the coherent energy exchange between photons and phonons at a rate Ω_R = 0.32 THz occuring inside the resonant cavity.

The relative strength of the coupling can be estimated from the ratio between the Rabi frequency and frequency of the cavity mode. The system falls in to the ultra-strong coupling(USC) regime when the ratio is greater than 0.1 to 0.2[216, 49]. The strength of the coupling of the hybrid system is estimated as 0.22 placing it close to the ultra-strong coupling regime.

Dispersion of Polaritonic States

The cavity-phonon hybridization can be confirmed to be in the strong coupling regime from the anticrossing of the polaritonic branches. To characterize the anti-crossing behaviour of polaritons, the fundamental mode of the cavity has been tuned across the phonon mode in $CuGeO_3$ at 80 K. The cavity frequency has been varied by moving cavity mirrors symmetrically in order to position the sample always at the center of the cavity.

The 2D terahertz transmission spectra as a function of cavity fundamental mode(ranging from 0.8 THz to 1.6 THz) is shown in Figure 5.3b. The most prominent modes observed near the phonon resonance at 1.45 THz can be identified as lower polariton(LP) and upper polariton(UP). By tuning cavity frequency away(lower) from the resonance case, both the LP and UP displays a blue-shift with respect to the resonant case and a change in the spectral content is also observed. LP and UP approaches the frequency of uncoupled cavity and phonon respectively when the fundamental mode of the cavity is different from the vibrational mode frequency. At the far off resonant case, the UP vanishes completely and

[1]Full Width Half Maximum

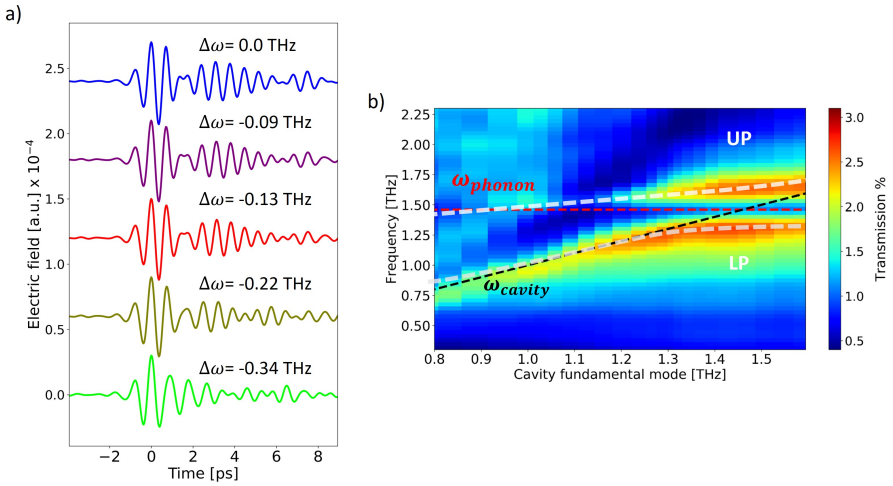

Fig. 5.3 **Dispersion of Polaritons** a) Terahertz field transmitted through the coupled cavity at different cavity detunings(fields are filtered the region between 0.4 THz and 2.5 THz). b) 2D transmission spectra of the system showing the dispersion of phonon polaritons at 80 K.[27]

only LP is visible. The dispersion of both polaritons in the transmission spectra shows a clear anti-crossing behaviour at the phonon frequency indicating the strong coupling phenomena.

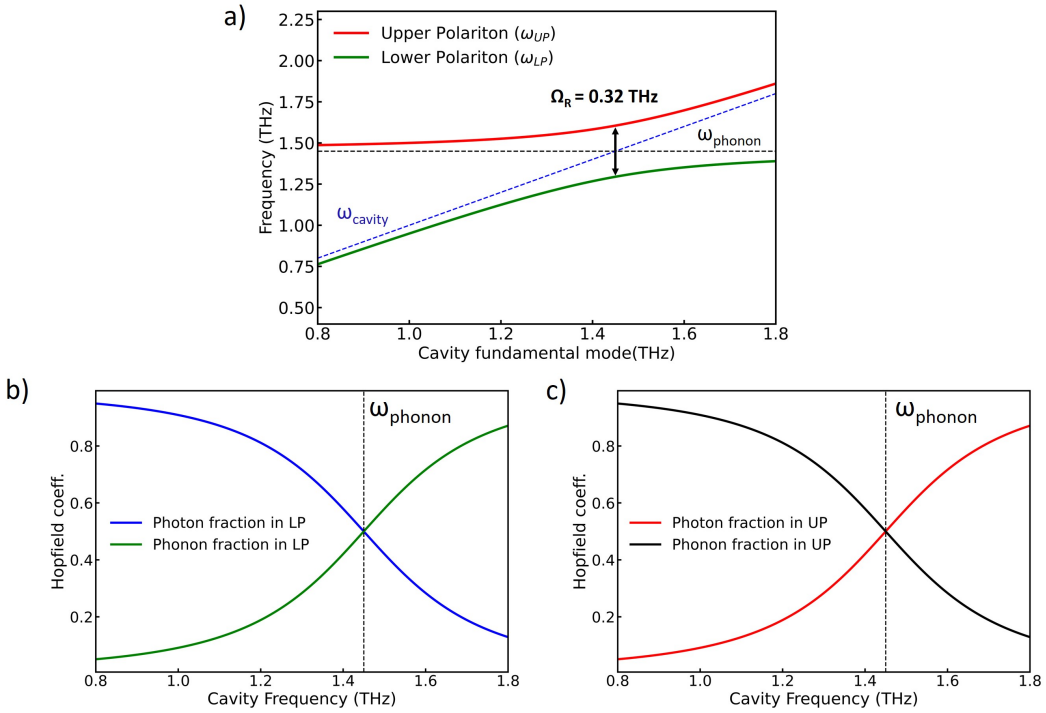

Fig. 5.4 **Polariton Dispersion obtained by the CHO model** a) Theoretical fit for the polariton frequencies using CHO model. Dashed lines represents the frequency of the uncoupled cavity (blue) and phonon (black) Hopfield coefficients for the b) Lower polariton(LP) and c) Upper polariton(UP)

Figure 5.3a presents the evolution of the filtered time-domain THz fields transmitted by the cavity for different detuning $\Delta\omega = \omega_{cav} - \omega_{phon}$ around the phonon frequency. The data conveys that the detuning of the cavity mode away from the vibrational mode results in the damping of the coherent Rabi oscillations with respect to the resonant case $\Delta\omega = 0$.

The dispersion of polaritons shown in Figure 5.3 can be modelled using the coupled harmonic oscillator(CHO) model described in section 2.3[80]. Dispersion of the polaritons shown in Figure 5.4a is estimated using the CHO model with a Rabi splitting $\Omega = 0.32$ THz and linewidths $\gamma_{cav} = 0.23$ THz and $\gamma_{phon} = 76$ GHz. The calculated contributions from photonic and phononic components for lower and upper polaritons are shown in Figure 5.4b and Figure 5.4c respectively. At lower frequencies LP has more cavity component and UP has more phononic component and vice versa for the cavity frequencies higher than the resonant vibrational phonon mode. At resonance, when the frequency of the cavity matches the phonon frequency, the polaritonic states are hybrid states of half light and and half matter as shown in Figure 5.4b and Figure 5.4c.

Temperature Evolution of the Vibro-Polaritonic States

The B_{2u} vibrational phonon mode in $CuGeO_3$ shows an anomolous monotonic blue shift above the spin - peierls transition when the temperature is increased from 14 K to 300 K. The optical spectroscopy measurements in [217] has reported a blue shift of 0.66 cm^{-1} and a broadening in the linewidth of 1.06 cm^{-1} in this temperature range due to the phonon thermal distribution. To comprehend the impact of thermal evolution of the vibrational mode on the polaritons, we monitored the dispersion of polaritons at different temperatures.

Figure 5.5a shows the comparison between transmission spectra of $CuGeO_3$ sample at 80 K and 290 K outside the cavity. We noted a blue shift of 0.05 THz in the vibrational Cu-O mode, accompanied by a 50% broadening in the line width. The broadening of the phonon line width implies a faster decay rate of the phonon mode, consequently resulting in a shorter polariton lifetime.

Figure 5.5b portraits the Rabi splitting in $CuGeO_3$ at 295 K(red) and 80 K(blue). We report a shift of the polariton states to higher frequencies at 295 K compared to 80 K. Additionally, the linewidth of the two polaritons becomes broader by increasing the temperature indicating a shorter polaritons' lifetime. We have mapped the polariton dispersion as a function of fundamental mode of the cavity at 80 K and 295 K in Figure 5.5c and Figure 5.5d respectively. The dispersion across the detunings shows significant broadening in the line width of the polaritons at 295 K. The dispersion plots also reveal a slight increase in the Rabi splitting between the vibro-polaritons at 295 K which can be rationalized from the relation between the Rabi splitting and the linewidth of the cavity and phonon we obtain from the diagonalization of the Hamiltonian. In the assumption of zero detuning between the phonon resonance and the cavity the Rabi splitting can be quantified as,

$$\Omega_R = 2\sqrt{g^2 - (\gamma_{cav} - \gamma_{phon})^2/16} \tag{5.1}$$

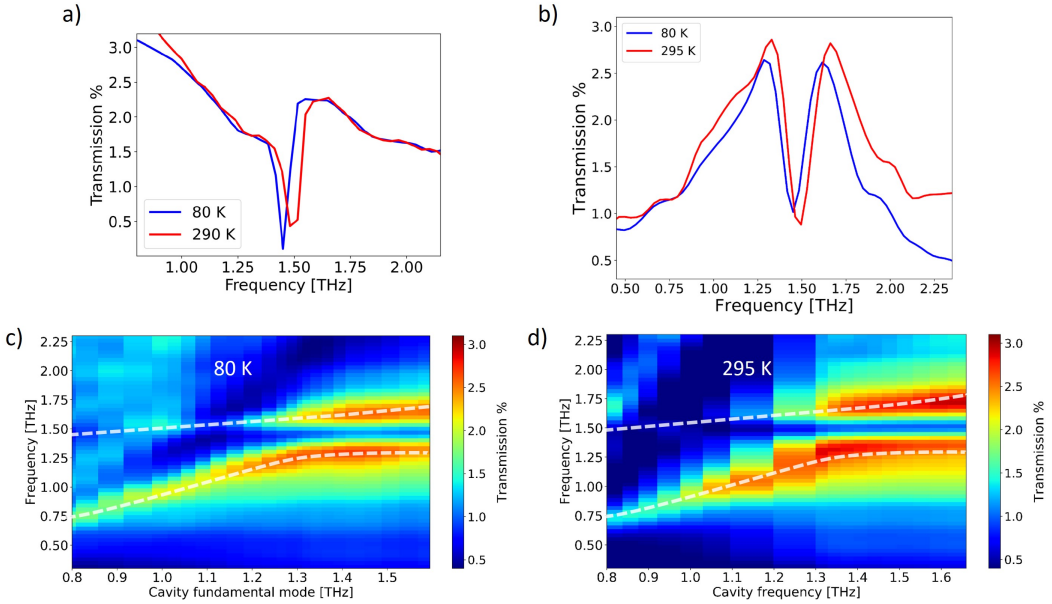

Fig. 5.5 **Thermal Evolution of the Polaritons** a) Rabi splitting of vibrational mode in $CuGeO_3$ at 295 K and 80 K. Vibro-polariton dispersion in $CuGeO_3$ at b) 80 K and c) 295 K

The relation says that the losses can be compromised by making the linewidth of the cavity and the material the same. Therefore we can conclude that the change in the Rabi splitting across the temperature can be attributed to the broadening of the bare B_2u mode.

5.3 Collective Strong Coupling in CDW Material 1T-TaS_2

Tantalum Disulphide, 1T-TaS_2 belongs to the family of quasi-two-dimensional transition metal dichalcogenides. The quasi-two-dimensional character is formed due to the weak van der Waals forces bounding the sheets of X–M–X(M-Transition metal ion, X- Chalcogenide) sandwiches(Figure 5.6a)[218]. The 1T corresponds to the polytype of the material associated with the octahedral stacking of the sandwich structure. $1T-TaS_2$ is significant being one of the earliest two-dimensional materials to exhibit the charge density waves[219]. Charge density wave materials(CDW) are characterized by the periodic charge density modulation accompanied by periodic lattice distortion[220, 221]. The CDW formation is usually described by Peierls transition[222] in which the electron phonon interaction causes a distortion in the metallic chain resulting in the opening of the gap at the new Brillioun zone boundary turning the metallic chain in to an insulator[220, 221].

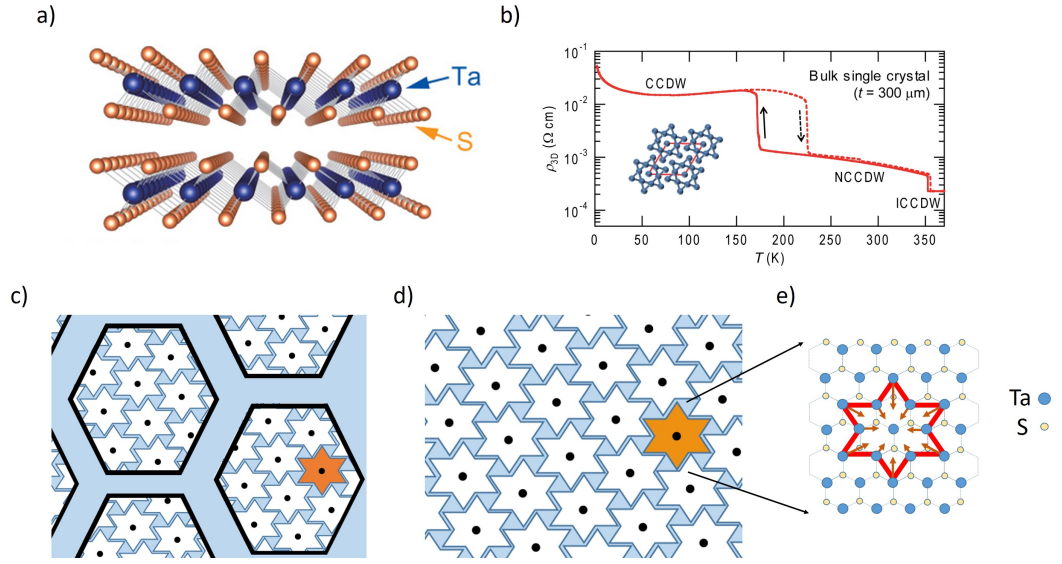

Fig. 5.6 **Tantalum Disulphide** a) Crystal structure of the layered 1T-TaS_2, where the planes of tantalum (Ta) atoms are surrounded by sulfur (S) atoms in an octahedral arrangement. b) Temperature dependence of the resistivity (ρ3D) of the bulk 1T-TaS_2(300 μm) single crystal. The solid and broken lines represent the ρ3D in the cooling and warming scan, respectively. The bulk sample showed the ICCDW-NCCDW transition at around 354 K with a hysteresis of 3 K and the NCCDW-CCDW transition at 200 K with a hysteresis of 51 K. Inset: The Ta atom distortions in the CCDW phase, whose reconstructed unit cell is represented by red lines(Pictures are taken from [218, 223]). Schematic of a Ta atom network in the c) hexagonal NCCDW and d)CCDW e) The crystal structure shows a David-star cluster, where 12 Ta atoms within the layer move toward a 13th central Ta atom.[134]

1T-TaS_2 undergoes first order phase transitions between thermodynamical phases differentiated by commensuration of CDW[224, 225] and resistivity[226]. Above 550 K, material is in a metallic phase with no CDW feature with space group $P\bar{3}m1$ space group[227, 228]. At T= 350 K, a CDW distorion results in an incommensurate CDW phase. By further cooling down the sample below 350 K, hexagonal domains of commensurate CDW(CCDW) clusters form with a domain size of 70 Å. Each of these hexagonal domain are consisted of clusters of tantalum atoms in the so called "Star of David" formation as shown in Figure 5.6e. The neigh-

bouring CCDW domains are separated by dicommensurate regions resulting in a metallic behaviour and hence this phase is called nearly commensurate CDW phase(NCCDW). The size of the CCDW hexagonal domains increases by lowering the temperature and becomes fully commensurate with the underlying lattice at T=180 K accompanied by a CDW wavevector rotation of 13.9°[229]. The commensurate CDW(CCDW) phase of 1T-TaS_2 shows an electronic behaviour of a mott insulator[230]. The schematic pictures of NCCDW and CCDW phases are illustrated in Figure 5.6c and Figure 5.6d respectively.

In 1T-TaS_2, the reconstruction of Brillioun zone boundary associated to the CDW transition occurs due to the structural distortion in the CCDW phase[225, 231, 232]. In this phase, the only unpaired electron sitting at the center of the David star occupies the narrow half filled band located above the lower bands containing paired electrons around the star, forming the uppermost cluster orbital(UCO). The insulating properties of the commensurate phase arises from the so called, Mott localization resulting in the splitting of UCO band into lower Hubbard band(LHB) and upper Hubbard band(UHB)[233–235]. The resistivity data of a 300 µm thick 1T-TaS_2 across different CDW phases are depicted in Figure 5.6b[223].

Firstly, we present the temperature dependent terahertz transmission measurements of a 10 µm thick 1T-TaS_2 across the NCCDW-CCDW phase transition. The measurement shows a drop in the low frequency conductivity, attributed to the opening of the Mott gap and the emergence of the CDW phonons resulting from changes in the screening of the modes by electrons in the NCCDW phase. In the later part, we report the signatures of multimode vibrational coupling in a 1T-TaS_2 embedded inside an optical cavity due to the cavity mediated hybridization of CDW phonons. The thermal evolution of multimode polaritons across the metal insulator transition reveals how the presence of free carriers is reflected in the multimode strong coupling.

5.3.1 Terahertz Characterization of the Metal-to-Insulator Phase Transition

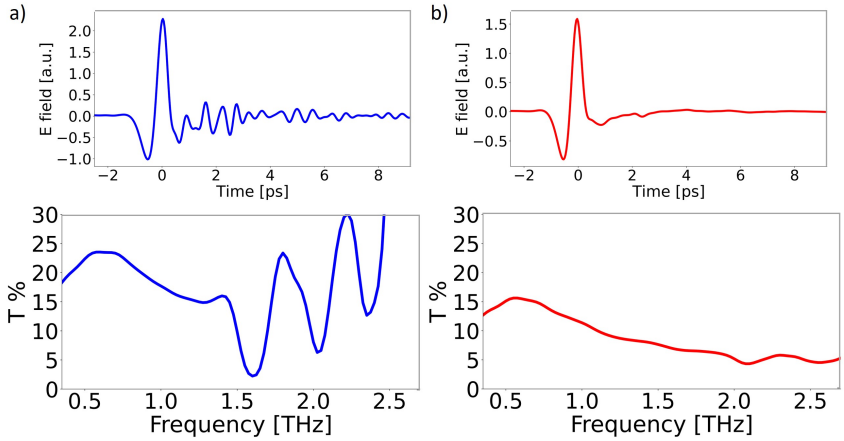

Fig. 5.7 **THz Transmission in the Metallic and Insulating States of 1T-TaS_2** Transmission spectra(bottom) of 1T-TaS_2 with time domain profile(top) for the a) Insulating phase and the b) Metallic phase[134]. [Terahertz source: PCA]

Figure 5.7a and Figure 5.7b shows the transmitted terahertz electric fields(top) and their Fourier transform spectra(bottom) of a 10 µm thick 1T-TaS_2 sample in the insulating and the metallic phase respectively. The terahertz data shows a slightly larger transmission in the insulating phase accompanied by the appearance of ripples in the time domain. The ripples can be observed in the transmitted spectra as absorptions centered at approximately 1.6, 2.0 and 2.3 THz respectively. These absorption can be associated to the three lowest-lying CDW phonon modes in 1T-TaS_2. The drop in the low frequency terahertz transmission can be attributed to the Drude-like response of free carriers.

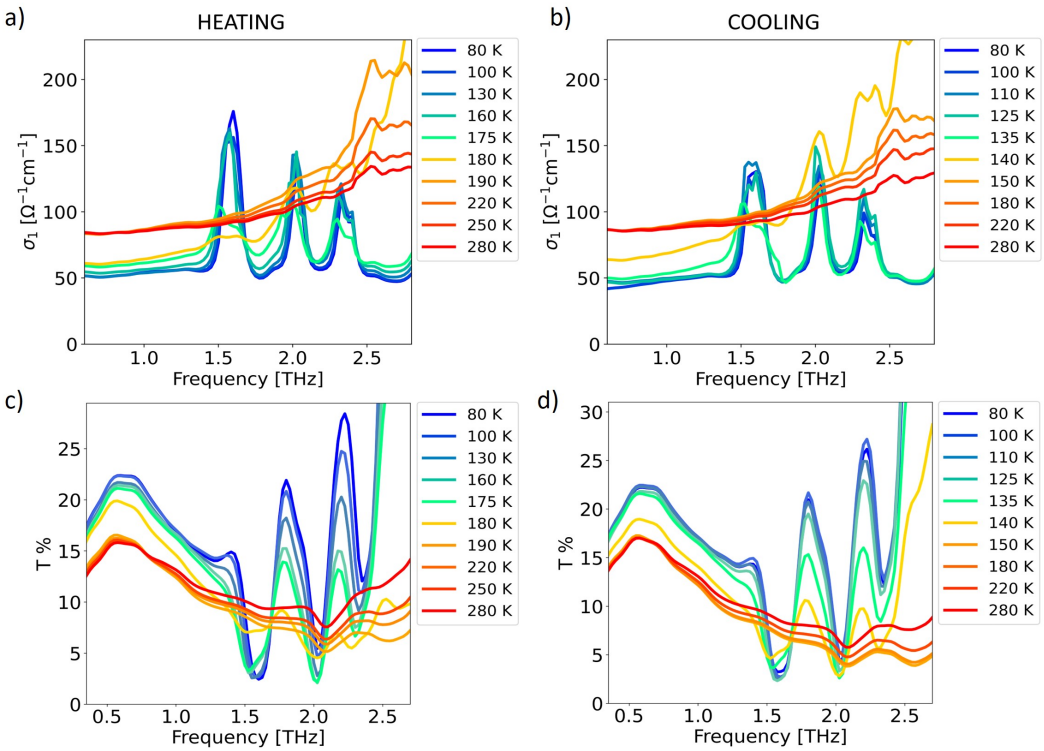

Fig. 5.8 **Temperature resolved Terahertz Measurements on 1T-TaS_2** Real part of the optical conductivity (σ_1 (ω)) measured in free space upon a) heating and b) cooling the sample from the insulating and metallic phase, respectively. THz transmission (T) measured in free space at different cold-finger temperatures T_{ext} upon c) heating and d) cooling the sample.[134]

Figure 5.8c and Figure 5.8d shows the THz transmission of 1T-TaS_2 across the first order phase transition as a function of cold finger temperature upon heating and cooling respectively. The transition between the NC-CDW metallic phase and the C-CDW insulating phase are reflected in the transmission as an increase in the low frequency transmission (0.2 THz < ω < 1.5 THz) below the phase transition temperature(T_c), attributed as Drude-like response of free the carriers and the screening of the infrared-active CDW phonon modes at 1.58 THz, 2.04 THz and 2.35 THz by free carries in the metallic phase[236, 237]. Figure 5.8a and Figure 5.8b shows the optical conductivity upon heating and cooling respectively obtained using the Fresnel relations explained in subsection 4.2.3. The Drude like optical conductivity above T_c indicates the presence of free carriers in the metallic phase. The difference in the T_c upon heating and cooling of the sample marks the hysteresis associated to the first-order phase transition. The phase transition in free space upon heating occurs

at T_c = 181 K and at 143 K upon cooling from the metallic phase. The discrepancy in the phase transition temperature (T_c) with respect to the literature value[238] can be attributed as difference between the temperature of the sample and the temperature of the cryostat's cold finger arising from the high thermal impedance of the Si_3N_4 membranes holding the 1T-TaS_2 sample.

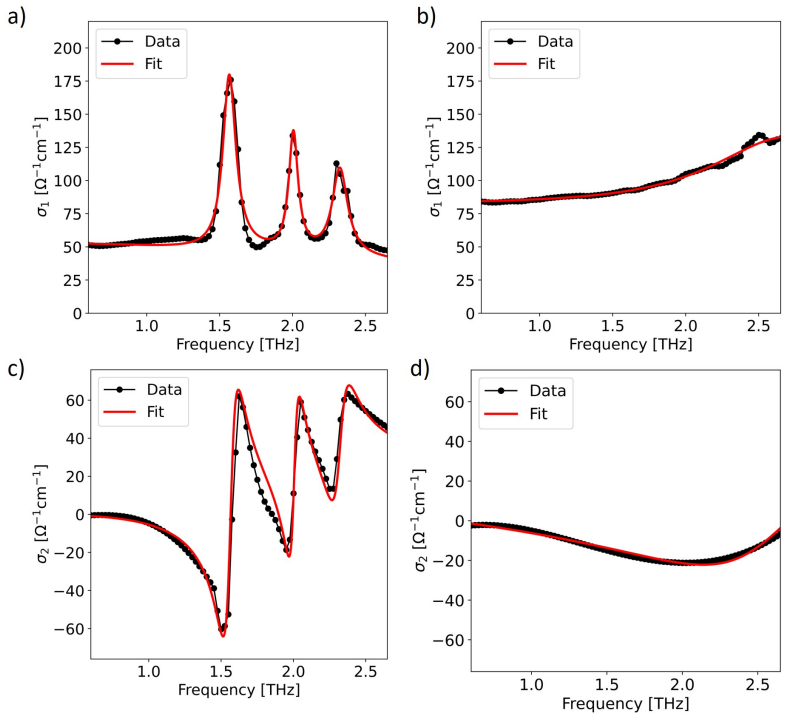

Fig. 5.9 **Complex Conductivity ($\tilde{\sigma}$) of 1T-TaS_2** Real part of the optical conductivity at a) T= 80 K b) T= 280 K. Complex part of the optical conductivity at c)T= 80 K d) T= 280 K.

The complex optical conductivity in Figure 5.9 can be described using Drude Lorentz model with harmonic oscillators given by[226, 236, 237]

$$\hat{\sigma}(\omega) = \frac{\sigma_0}{1 - i\omega\tau} + i\epsilon_0\omega\left(1 - \epsilon_\infty - \sum_{j=1}^{n} \frac{S_j}{\omega_{0j}^2 - \omega^2 - i\omega\gamma_j}\right). \tag{5.2}$$

in which the first term is the Drude conductivity in which $\sigma_0 = \epsilon_0\omega_p^2\tau$. σ_0 is the static conductivity and τ is the scattering time. ϵ_∞ is the high frequency response of the dielectric constant. The last term represents the contribution from the j^{th} harmonic oscillator, where S_j is the oscillator strength, ω_{0j} is the resonance frequency and γ_j is the line width of the same.

The real and imaginary part of optical conductivity at T=80 K (Figure 5.9a and c) and at T = 280 K(Figure 5.9b and d) has been fitted using the Drude-Lorentz model(red line) with REFFIT software. The parameters extracted from the fits are listed in Table 5.1 for the insulating C-CDW phase(T=80 K) and in Table 5.2 for the metallic NC-CDW phase(T=280 K). The mode frequencies and the static conductivity(σ_0) are in good agreement with the

j	ω_{0j} [THz]	γ_j [THz]	S_j
1	1.58	0.110	9.86
2	2.02	0.101	3.05
3	2.35	0.125	2.81

Table 5.1 Drude-Lorentz fit parameters of 1T-TaS_2 in the insulating phase(at T= 80 K)

ϵ_∞	σ_0 [$\Omega^{-1}\times$ cm^{-1}]	τ [fs]
3.5	52.8	215

Table 5.2 Drude-Lorentz fit parameters of 1T-TaS_2 in the metallic phase(at T= 280 K)

values in the literatures[236, 237]. In addition. the insulator metal transition is accompanied by an increase in the Drude scattering time τ and static conductivity σ_0.

5.3.2 Multimode Vibrational Coupling in the CDW Phase of 1T-TaS_2

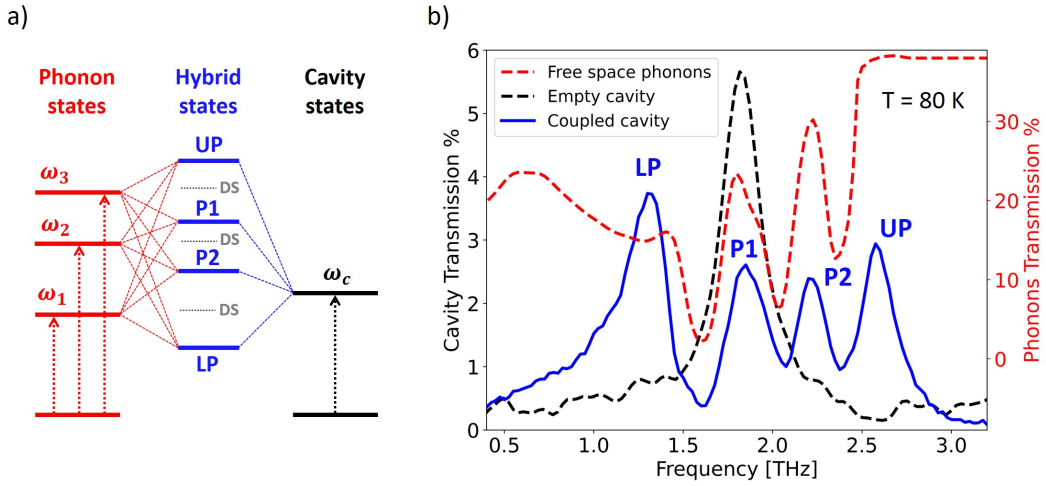

Fig. 5.10 **Multimode vibrational coupling in 1T-TaS_2** a) Energy level scheme of the hybridization of the C-CDW phonons with the cavity mode. Strong coupling between the three C-CDW phonons at frequencies ω_1, ω_2, ω_3 and fundamental cavity mode at frequency ω_c results in the formation of four non-degenerate hybrid states: an upper (UP) and a lower (LP) polariton, and two middle polariton resonances (P1, P2). Dark states resulting from the strong coupling are denoted with DS. b) Transmission spectrum (red, right axis) of the uncoupled 1T-TaS_2, bare cavity(black dashed spectrum, left axis) and the coupled system when the cavity mode is resonant to the midpoint of two C-CDW phonons at 80 K.

The coupling between the fundamental mode of the cavity with the CDW phonon modes in 1T-TaS_2 has been studied by placing the sample inside a Fabry Perot cavity with quality factor Q=7.2. The cavity length has been tuned in order to be resonant to the midpoint of two adjascent CDW phonons ($\omega_{1,2,3}$ = 1.58, 2.02, 2.3 THz) in the insulating phase of 1T-TaS_2. As in the case of single mode case, coupling between the phonons and the cavity mode is determined by the photon decay rate of the cavity and the lifetime of the CDW phonon modes which can be directly mapped from the line width of the cavity and the CDW phonon absorptions respectively. The terahertz spectral response of the uncoupled cavity

(black dashed line), CDW phonons(red dashed line) along with the coupled system(blue dashed line) at 80 K are shown in Figure 5.10b. The transmitted spectra from the coupled system exhibits the splitting in to four spectrally separated peaks as a result of multi-mode coupling between the three CDW phonon modes and the cavity mode. The peaks can be associated to the formation of light matter hybrid states named as lower polariton(LP), upper polariton(UP) and two middle polaritons(P1 and P2) as marked in the Figure 5.10. The splitting between the adjascent polaritons ($\Omega_{1,2,3}$=0.496, 0.301, 0.310 THz) are greater than the line width of both the bare cavity(0.25 THz) and the CDW phonons ($\gamma_{1,2,3}$= 0.172, 0.154, 0.148 THz) indicating that the CDW excitations in the 1T-TaS_2 are in the strong coupling regime.

Dispersion of Polaritonic States

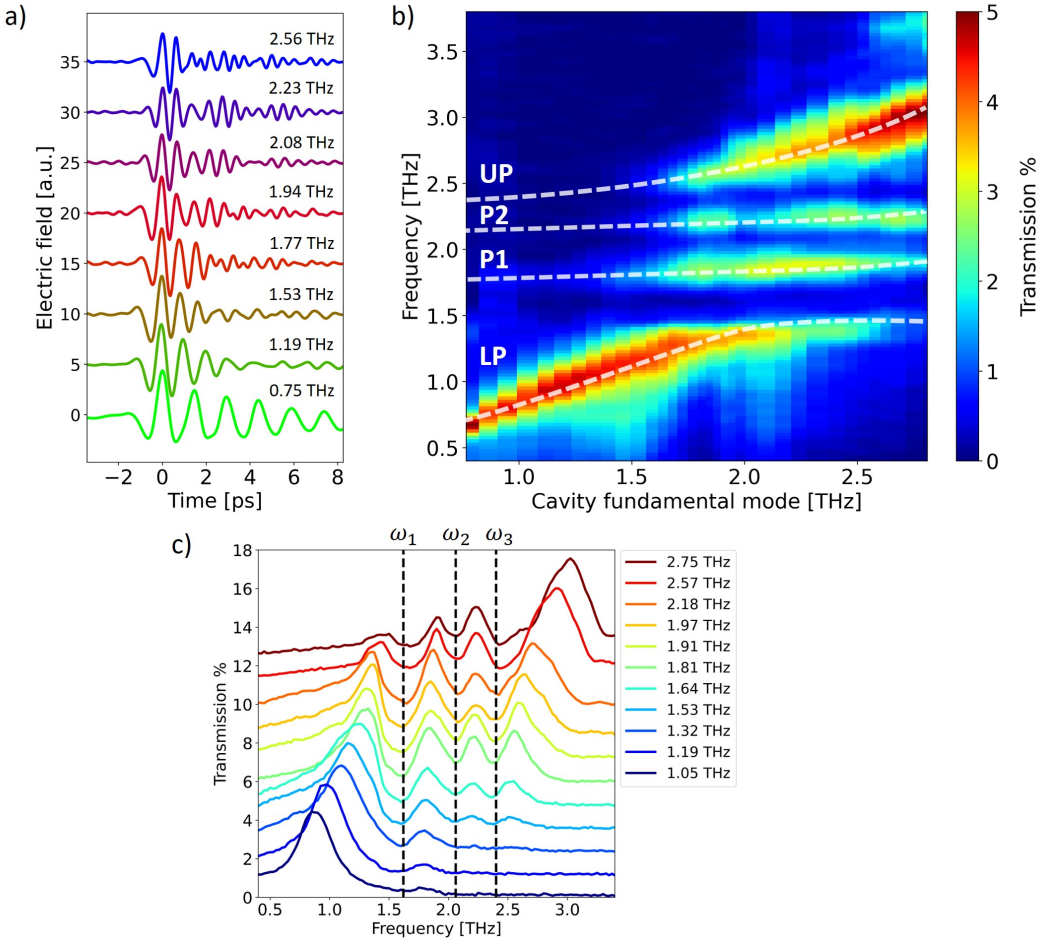

Fig. 5.11 **Multimode Polariton Dispersion in 1T-TaS_2** a) Terahertz field from the 1T-TaS_2 embedded inside the cavity of different resonance frequencies b) 2D transmission spectra of the system showing the dispersion of the multimode polaritons at 80 K. c) Transmission spectra of the hybrid sytem at 80 K with cavity fundamental modes tuned across the three phonon resonances of the C-CDW phase (ω_1 = 1.58 THz, ω_2 = 2.02 THz, ω_3 = 2.35 THz). The spectra have been vertically shifted for clarity.[239]

Figure 5.11b and c illustrates the dispersion of multimode polaritons and selected transmission spectra measured when the cavity fundamental mode is tuned across CDW excitations. The dispersion of upper polariton branch, lower polariton branch and the middle polariton branches are marked as UP, LP, and P1 and P2 respectively in the 2D plot. The Rabi splitting in to multiple polaritons are very evident when the cavity is resonant to the CDW phonon modes as a consequence of strong coupling. In addition, it can be seen that the polaritons are behaving differently when the cavity fundamental mode is tuned towards the off-resonance conditions(Figure 5.11c). The energy of the lower and and upper polarions(LP, UP) are dispersing with the cavity mode and approaches the energy of the uncoupled cavity and the CDW phonon mode when the cavity frequency is away from the resonance case. The lower (upper) polariton energy tends to the bare cavity resonance at low (high) frequency and to the lowest(ω_1) (highest(ω_3)) CDW mode at high (low) frequency. On contrary to this, the energies of the two middle polaritons (P1, P2) do not show any dependence on the cavity frequency. The frequencies of the middle polariton states remains at the midpoints of adjacent phonons. It can seen that the hybrid polariton states exhibits an anti-crossing behaviour, a distinctive feature of strong coupling regime.

Figure 5.11a presents the evolution of the time-domain THz fields transmitted by the cavity for different cavity frequencies around the CDW phonon modes. When the cavity is in the resonance case, the THz field shows an exponential decay modulated by multiple Rabi oscillations instead of a single periodic beating. This emerges from the interference of multiple polaritons originated from the coherent exchange of energy between the cavity and the CDW phonons.

The multi-mode rabi splitting can be analyzed using the coupled harmonic oscillator(CHO) model with four oscillators and the diagonalization of the Hamiltonian will give the energy of the eigen states as the linear combinations of cavity and the CDW phonon modes. In an assumption that there are N excited phonons for each of the three measured CDW modes, the polariton wave-function $|\psi_{PL}\rangle$ can be given by

$$\begin{aligned}|\psi_{PL}\rangle = \chi_{cav}(\Delta\omega)\,|0,0,0;1\rangle + \chi_1(\Delta\omega)\sum_{i=1}^{N}|e_i,0,0;0\rangle + \chi_2(\Delta\omega)\sum_{i=1}^{N}|0,e_i,0;0\rangle \\ +\chi_3(\Delta\omega)\sum_{i=1}^{N}|0,0,e_i;0\rangle\,.\end{aligned} \tag{5.3}$$

Here $|0,0,0;1\rangle$ represents the purely cavity state, and $\sum_{i=1}^{N}|e_i,0,0;0\rangle$, $\sum_{i=1}^{N}|0,e_i,0;0\rangle$ and $\sum_{i=1}^{N}|0,0,e_i;0\rangle$ the pure vibrational states of first, second, and third CDW phonons respectively in which they are in their excited state. We stress that the wave-function components must satisfy the normalization condition $|\chi_{cav}|^2 + \sum_{i=1}^{3}|\chi_i|^2 = 1$ for each cavity frequency ω_c. $|\chi_{cav}|^2$ and $|\chi_{1,2,3}|^2$ are the ratio of the optical and the phonon character of the hybrid states which can be obtained from the Hamiltonian given by[240, 241]

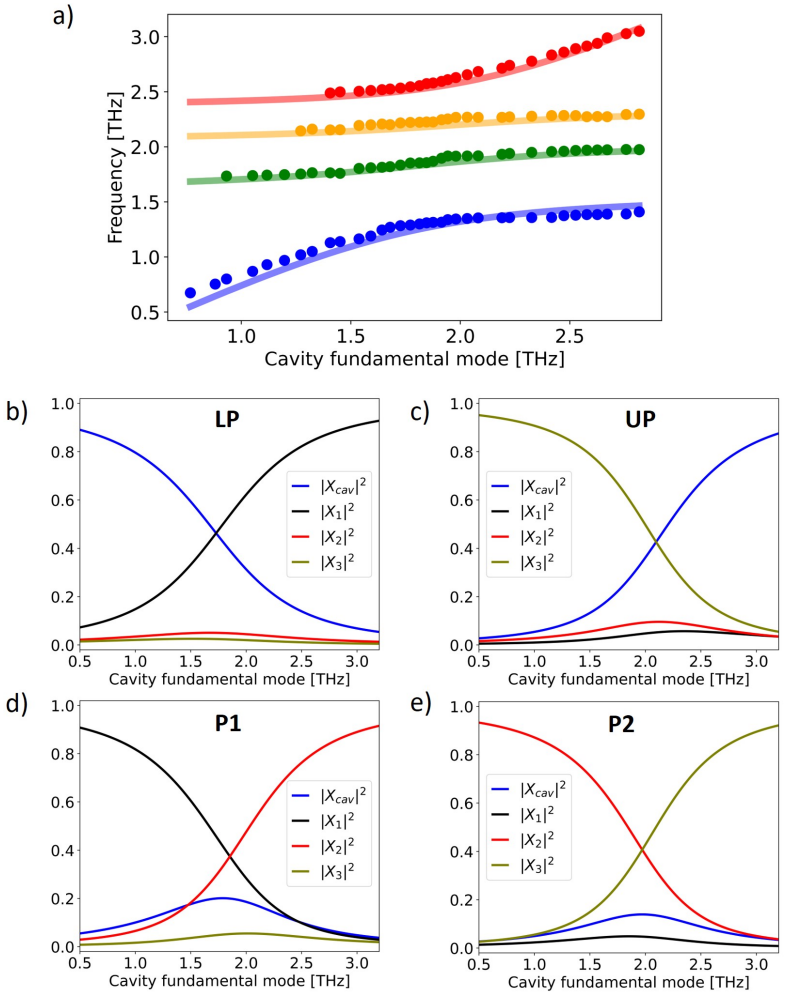

Fig. 5.12 **Polariton dispersion with CHO model in 1T-TaS_2** a) Theoretical fit for the polariton frequencies using CHO model. The circle correspond to the measured polariton peaks, while the solid curves show the frequencies obtained from the CHO model b,c,d and e) Cavity ($|\chi^2_{cav}|$) and phonon ($|\chi^2_{1,2,3}|$) fractions of the polariton wave-functions as a function of the cavity frequency.[239]

$$\hat{H}\begin{pmatrix}\chi_{cav}\\ \chi_1\\ \chi_2\\ \chi_3\end{pmatrix} = \hbar\begin{pmatrix}\omega_c - i\gamma_{cav} & \frac{\Omega_{12}}{2} & \frac{\Omega_{23}}{2} & \frac{\Omega_{34}}{2}\\ \frac{\Omega_{12}}{2} & \omega_1 - i\gamma_1 & 0 & 0\\ \frac{\Omega_{23}}{2} & 0 & \omega_2 - i\gamma_2 & 0\\ \frac{\Omega_{34}}{2} & 0 & 0 & \omega_3 - i\gamma_3\end{pmatrix}\begin{pmatrix}\chi_{cav}\\ \chi_1\\ \chi_2\\ \chi_3\end{pmatrix} = E\begin{pmatrix}\chi_{cav}\\ \chi_1\\ \chi_2\\ \chi_3\end{pmatrix} \tag{5.4}$$

where γ_{cav} and $\gamma_{1,2,3}$ are the linewidths of the cavity and CDW phonon respectively, ω_c and $\omega_{1,2,3}$ are their resonance energies, and Ω_{12}, Ω_{23} and Ω_{34} represent the Rabi splitting between each other. Based on Equation 5.4, the eigenvalues as a function of the cavity frequency are obtained as shown by the solid lines in Figure 5.12a, which agree with the polariton frequencies(circles) obtained from the transmission measurements. Figure 5.12b,c,d and e shows the cavity and phonon fractions for the four polariton states as a function of the cavity fundamental mode, from which we can conclude that the LP(UP) is mainly a

hybrid state of the cavity mode and the first(third) CDW phonon mode while P1 and P2 are hybrid states of the adjascent CDW phonon modes. At lower frequencies LP has more cavity component and UP has more phononic component from the CDW mode and vice versa for the cavity frequencies higher than the resonant condition. However, the anti-crossing feature of the lower polariton originates from the coherent mixing of the ω_1 CDW mode with the cavity field and of the upper polariton results from the mixing between the ω_3 CDW mode and the cavity photons. In addition, the strongly dispersive properties of the LP and UP can be explained from the larger contribution of cavity in these states. The lower cavity fraction of the P1 and P2 results in the low dispersive behaviour of middle polaritons. The CHO model points that the light matter hybrid state P1(P2) originates from the cavity mediated hybridization of ω_1 and ω_2(ω_2 and ω_3) CDW phonon modes. Also it can be seen that the contribution of the cavity and phonon are closer at the resonance condition implying that the strongest interaction is achieved when the cavity is resonant to the CDW excitations.

Temperature Evolution of the Multi-Polaritonic States

The first order insulator metal transition in the 1T-TaS_2 CDW material is accompanied by the screening of the low frequency CDW phonon modes by the free charges in the metallic state. In order to understand how the thermal evolution of the CDW phonon modes are mapped on to the multi-mode polaritons in the insulating phase of 1T-TaS_2 the response of the coupled C-CDW phonons has been studied across the phase transition temperature.

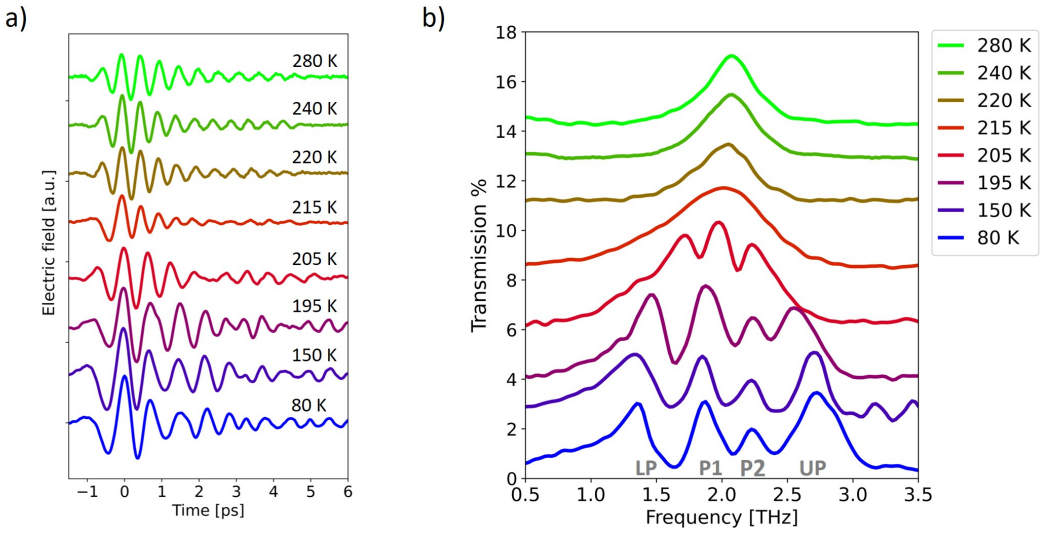

Fig. 5.13 **Temperature Evolution of the Multi-Polaritonic States in 1T-TaS_2** a) Time domain profile and b) the corresponding transmission spectra of the hybrid system across the CCDW-NCCDW phase transition temperature at a fixed cavity frequency.

Figure 5.13a and Figure 5.13b shows the temperature dependence of the terahertz traces and the transmission spectra of the 1T-TaS_2 embedded inside a cavity with resonant frequency, $\omega_c = 2.1$ THz. The thermal evolution of the terahertz response from the coupled system has been tracked by heating the sample from the insulating CCDW phase to NCCDW phase. At low temperature, the transmission spectra exhibits the splitting in to

four polaritons due to the strong coupling between the cavity fundamental mode and CDW phonons in the insulating phase. As we approach the phase transition by increasing the temperature of the sample the Rabi splitting closes and polaritonic features vanishes in the metallic phase. This can be associated to the suppression of polaritons due to the screening of the CDW phonons by the free carriers.

The time domain traces of the transmitted terahertz field shown Figure 5.13b also displays the closing of the polariton resonances across the phase transition temperature. The multiple Rabi oscillations are stretched and the modulations in the decaying field has been reduced by increasing the temperature towards the critical temperature (T_c = 215 K). The screening of the CDW phonon modes in metallic state results in the evolution of the transmitted terahertz waves into a field exhibiting single exponential decay as that of a bare cavity.

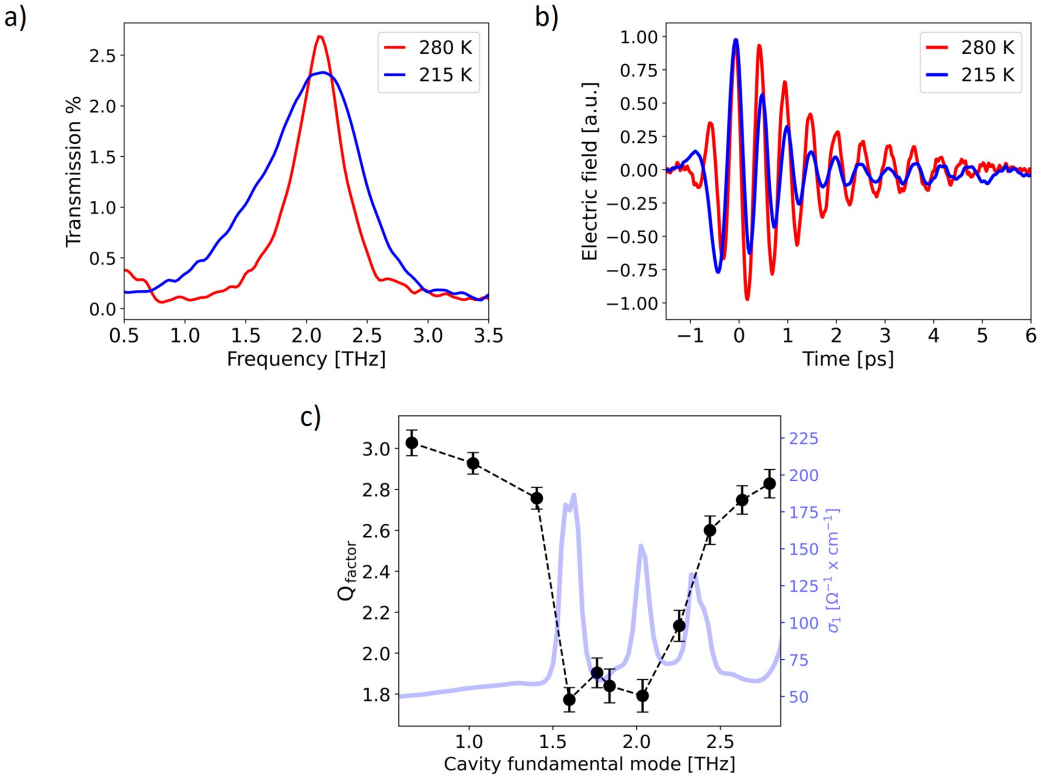

Fig. 5.14 **Signatures of Weak Coupling across metal-to-insulator transition in 1T-TaS_2** a) Transmission spectra and b) time domain terahertz field of 1T-TaS_2 measures inside a cavity resonant to the CDW phonons(ω_c= 2.1 THz) measured in the high temperature metallic phase (T= 280 K) and in the proximity of the heating critical temperature (T = 215 K). The presented fields have been normalized by their respective maximum in order to highlight their different temporal dynamics. c) Estimated quality factor(Q_{factor}) in proximity of the critical temperature (215 K) as a function of the cavity frequency (left axis). A decrease of the quality factor of the coupled cavity is measured across the spectral region of the C-CDW phonons, as shown by the optical conductivity σ_1 measured at 80 K in the C-CDW state (light blue, right axis).

In addition, the screening of the CDW phonon modes in the proximity of the phase transition temperature is mapped differently in the polaritonic states of 1T-TaS_2. The

linewidth of the polaritons have become significantly broader closer to the phase transition and the upper and lower polaritons are strongly modified compared to the middle polaritons. It is also noteworthy that the cavity peak has broadened at the phase transition temperature (T_c = 215 K) compared to higher temperatures suggesting an increase in the cavity dissipation closer to T_c. In order to highlight this, transmission spectra and the time domain traces of the coupled cavity with fundamental mode on resonance with the CDW modes (ω_c = 2.1 THz) at T=215 K and T= 280 K are plotted in Figure 5.14a and b respectively. The broadening of the coupled cavity at the phase transition is evident from the comparison of resonance peaks at T= 215 K and T= 280 K (metallic phase) in the transmission spectra. Also, the time domain terahertz fields (Figure 5.14b) at T= 215 K shows a faster decay with respect to the terahertz field of the 1T-TaS_2 in the metallic phase, indicating a depletion in the cavity photon lifetime. The enhancement in the dissipation reveals that the cavity exhibits the characteristic of the weak coupling regime at T_c [242, 243, 15].

The estimated quality factor of the coupled cavity in proximity of critical temperature is plotted in Figure 5.14c as a function of cavity frequency, to provide an insight in to the cavity dissipations[244]. The quality factor exhibits a drop when the cavity resonance is swept across the CDW phonon modes in the CCDW phase (see the plot of the 80 K optical conductivity (σ_1) superimposed in blue in Figure 5.14c) indicating an enhancement in the cavity dissipation at critical temperature (T ~ 215 K). This can be associated to the Purcell effect which has been attributed as an outcome of the weak coupling regime in atomic and molecular systems[6, 7, 245, 246]. Hence, we can conclude that the free charge screening results in an increase of the dissipative rates of the cavity photons when the energy is comparable to that of CDW excitations, consistent with a transition to a vibrational weak coupling regime.

The signatures of weak coupling regime at the phase transition temperature can be also utilized to reason about dispersion of polaritons closer to T_c. The increase in the dissipation rate of the cavity at the phase transition would reduce the coupling between the cavity mode and the CDW excitations, and hence the Rabi splitting. Using CHO model, we discovered that the cavity components in the lower and upper polaritons are much stronger than the middle polaritons. So, the changes in the dissipations of the cavity will be more evident in the response of the upper and lower polaritons. Therefore, strong dispersion of lower and upper polariton frequencies at the phase transition can be linked to the increase in the dissipative rates of the cavity due to the coupling with the free charges.

5.4 Conclusions

In the first section of the chapter, we have investigated the vibrational strong coupling regime in a $CuGeO_3$ material by embedding in to a cavity resoanant to the vibrational phonon mode at 1.45 THz. We have reported Rabi splitting in to the light matter hybrid states called Polaritons and the anti-crossing phenomena from the direct measurement of the polariton dispersion curves, pointing out that the that the system is in the strong coupling regime. The thermal evolution of the polaritons has been studied in order to understand the influence of phonon lifetime in the light matter coupling. We detected slight increase in the Rabi splitting between the polaritonic branches at higher temperature due to the change in the phonon linewidth.

In the second part, the multimode vibrational strong coupling has been reported in the insulating phase of the CDW material 1T-TaS_2 as a result of hybridization of CDW phonon modes with the fundamental mode of the cavity. The strong coupling between the cavity mode and the three CDW phonon modes results in the formation of four hybrid polaritonic states. The dispersion of the polaritons have been analyzed using the CHO model to obtain the optical and phononic character of each of the polaritons. The dispersion of polaritonic states across the insulator metal revealed the closing of Rabi splitting in the metallic phase and weak coupling features have been observed at the phase transition resulting in the enhancement of cavity dissipation.

6

Cavity-mediated Thermal Control of Metal-to-Insulator Transition in 1T-TaS_2

6.1 Motivation

Over the last century, the control of solid state systems using strong light has been thoroughly investigated unveiling the microscopic mechanisms such as nonlinear phonon interaction[247–249], displacive excitation of coherent phonon[250], and Floquet engineering [251, 252]. Recent advances in the state-of-art laser techniques have made the illumination by ultrashort light pulses a promising route for studying and controlling the macroscopic properties of the quantum materials providing attractive physical phenomena beyond the steady-state of materials. The experimental frameworks in this direction have reported enhanced superconductivity in cuprate[253], alkali-doped C_{60}[254], and molecular solids[255], light induced ferroelectric transition of quantum paraelectric $SrTiO_3$[132, 133], light induced topological phase transition in layered WTe_2 and $ZrTe_5$[256, 257] and light controlled magnetism in piezo-magnetic material[258] and transition metal-dichalcogenides[259]. In addition, the hidden phases that are rarely accessible on equilibrium phase diagrams have been also revealed by driving the system using optical pulses, such as the meta-stable metallic state of 1T-TaS_2[260] and Bose–Einstein condensation in Ta_2NiSe_5[261].

A new approach towards altering the material properties has opened recently by replacing the classical laser field with quantum mechanical photon modes in a cavity[262]. This approach makes the strong coupling between matter and light possible even without the presence of photon, i.e. through vacuum fluctuations inside an optical cavity. Various theoretical frameworks have been proposed in the direction of controlling the ground state properties of the materials by cavity quantum electrodynamics. This includes the control of magnetic phases in correlated magnetic systems[263–265], formation of exciton polaritons in two dimensional materials[36], cavity enhanced electron phonon coupling[31], cavity induced ferroelectricity in $SrTiO_3$ [37, 38] and cavity enhanced superconductivity[266, 29]. The past decade has been witness to great advances in experimental cavity QED as well

apart from these theoretical models such as cavity enhanced ferromagnetism[45], cavity enhanced superconductivity[44] and cavity control of quantum Hall effect in 2D electron gases[43].

In this chapter, we are demonstrating out efforts to control metal insulator phase transition in a charge density wave(CDW) material 1T-TaS_2 by means of cavity electrodynamics. Reversible control of metal to insulator phase transition has been feasible by embedding 1T-TaS_2 in a tunable cryogenic terahertz cavity[27]. The experimental results reveals that the effective critical temperature of the CDW transition can be controlled by changing the resonant frequency of the cavity and the alignment of the cavity mirrors which is triggered by a change in the sample temperature in a Purcell-like scenario[5]. We have put forward two plausible scenarios to explain the dependence of the effective critical temperature on the cavity environment. First one has been based on the renormalization of the free energies of the metallic phase and the dielectric phase for different cavity lengths. The second scenario explores the possibility that the cavity reshapes the exchange of energy between the material and the thermal reservoir of photons in which the material is immersed resulting in a cavity mediated change in the temperature of the sample. The temperature measurements reveal that the renormalization effect is dominated by the purcell like scenario. The content of this chapter has been published in [134].

6.2 Renormalization of the Effective Phase Transition Temperature within the Cavity

We performed temperature dependent THz linear transmission (Source:PCA) of 1T-TaS_2 in free space upon heating and cooling to capture the first order phase transition between the nearly commensurate charge density wave(NC-CDW) metallic phase and the commensurate charge density wave(C-CDW) insulating phase. The detailed explanation of the thermodynamic phases and charge density wave(CDW) dynamics of 1T-TaS_2 is given in section 5.3. The temperature dependent THz linear transmission of a 15 μm single crystal is given in Figure 6.1a. As noted in section 5.3, the first order insulator to metal transition in 1T-TaS_2 is characterized by optical features such as increase of the low frequency transmission (0.2 THz $< \omega <$ 1.5 THz) and the emergence of IR-active optical phonons at 1.58 THz, 2.02 THz, and 2.35 THz which are allowed by the symmetry of the fully commensurate charge density wave below the critical temperature . The CDW phonons are suppressed in NC-CDW metallic phase due to the screening by the free carriers. Since the low frequency transmission(0.2 THz $< \omega <$ 1.5 THz) can be directly linked to the metallicity of the system the integrated transmission at this frequency range(Figure 6.1b) can be used as a marker to track the charge order dynamics in 1T-TaS_2 and hence the metal-to-insulator phase transition.

The integrated low frequency transmission obtained upon cooling and heating the sample in freespace shown in Figure 6.1b marks the hysterisis associated to the first order phase transition. The phase transition in free space upon heating and cooling occurs at 181 K and at 143 K respectively. The effective phase transition temperature was estimated from the maximum of the derivative of the interpolated metallic temperature response[134]. The smooth transition observed could be ascribed to the presence of intrinsic inhomogeneities and strain in the system which smear out the first order transition[134]. The difference

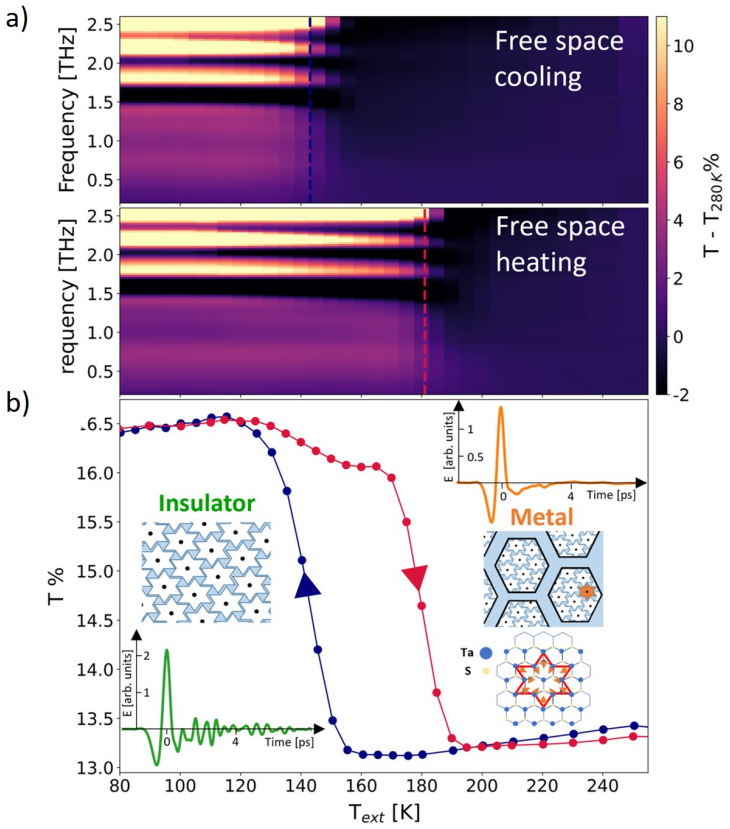

Fig. 6.1 **THz linear spectroscopy of 1T-TaS_2 metal-to-insulator transition measured in free space.** a) Temperature depenedent THz linear transmission spectra of 1T-TaS_2 in free space across metal-to-insulator transition (temperature scans performed by cooling (upper panel) and heating (lower panel)). In order to highlight the phase transition each spectrum has been subtracted from the spectra of 280 K b) Temperature dependence of the integrated low frequency transmission (0.2 THz $< \omega <$ 1.5 THz), marking the metal-to-insulator transition and its hysteresis. The temperature scale indicates the readout of the thermocouple in thermal contact with the cryostat cold finger. In the insets the time domain THz fields are shown for the metallic and the insulating phases, together with the illustration of the in-plane lattice modulations characteristic of the insulating C-CDW phase and of the metallic NC-CDW phase. [134]

(35 K) in the estimated critical temperature with respect to the literature value[238] can be attributed to the mismatch between the sample(T_s) and the cold finger temperature(T_{CF}) due to the high thermal dissipation of the silicon nitride membranessubsection 4.1.4. Hence, in this chapter, we will refer to the critical temperatures detected through THz spectroscopy as effective critical temperatures (T_c^{eff}).

Cavity driven changes in the metal-to insulator transition has been studied by embedding the 1T-TaS_2 at the center of a sub-THz cavity of resonant frequency 11.5 GHz and quality factor, Q~4.

The comparison between the temperature dependent terahertz linear transmission inside the cavity (11.5 GHz) and the freespace is given in Figure 6.2. The Figure 6.2 shows that the effective critical temperature(T_c^{eff}) is shifted to 136 K and 109 K respectively upon heating and cooling the sample inside the 11.5 GHz cavity. The comparison with the

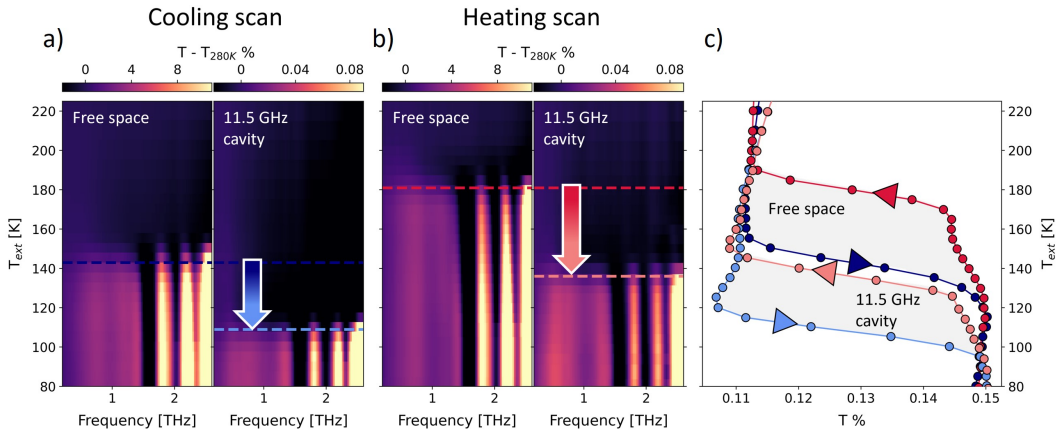

Fig. 6.2 **Cavity-driven renormalization of the effective critical temperature of the metal-to-insulator phase transition.** Temperature dependent THz transmission upon a) cooling b) and heating for a sample held in free space (left) and one placed in the middle of the 11.5 GHz cavity (right). c) Comparison between the hysteresis in free space and within the 11.5 GHz cavity plotted as the integrated cavity transmission in the range 0.2 THz $< \omega <$ 1.5 THz. The free-space data have been arbitrarily translated along the horizontal axis to overlap with the cavity integrated transmission. A possible cavity-driven renormalization of the effective critical temperature of 44 K (33 K) towards lower temperatures is measured upon heating (cooling) the sample. This results in a cavity-mediated shrinking of the phase transition hysteresis of 11 K. [134]

freespace indicates that the cavity mediated renormalization of the effective phase transition temperature differs in the heating cycle(44 K) and cooling cycle(33 K) resulting in the shrinking of the hysterisis inside the cavity.

6.2.1 Dependence of T_c^{eff} on Cavity Alignment

The renormalization of the effective phase transition temperature inside the cavity has been further investigated by changing the alignment of the cavity mirrors. This allows direct mapping of the cavity mediated effects on the effective phase transition temperature, as the cavity misalignment leads to an increase in the decay rate of the cavity photons.

THz time domain traces of the 11.5 GHz cavity in the C-CDW phase for different misalignment angles(θ) are shown in Figure 6.3a. We quantify the cavity misalignment(θ) as the sum of the misalignment angles of the two cavity mirrors with respect to the parallel mirrors configuration. The Fabry Perot reflection associated to the cavity round trip is highlighted in the dashed box. As shown in Figure 6.3b the changes in the alignment of the mirrors causes slight modification in the cavity fundamental frequency($\Delta\omega_c \sim 0.14$ GHz/deg). However, the reduction in the intensity of the cavity peak upon misalignment reflects decrease in the photon lifetime inside the cavity and hence the quality factor. The cavity Q factor as a function of the misalignment angle is shown in Figure 6.3c. The estimation has been performed by approximating the exponential decay with a linear fit.

The temperature dependence of the integrated low frequency(0.2 THz $< \omega <$ 1.5 THz) terahertz transmission at different misalignment of the cavity mirrors is shown in Figure 6.4a. The data reveals that renormalization in the effective phase transition temperature reduces

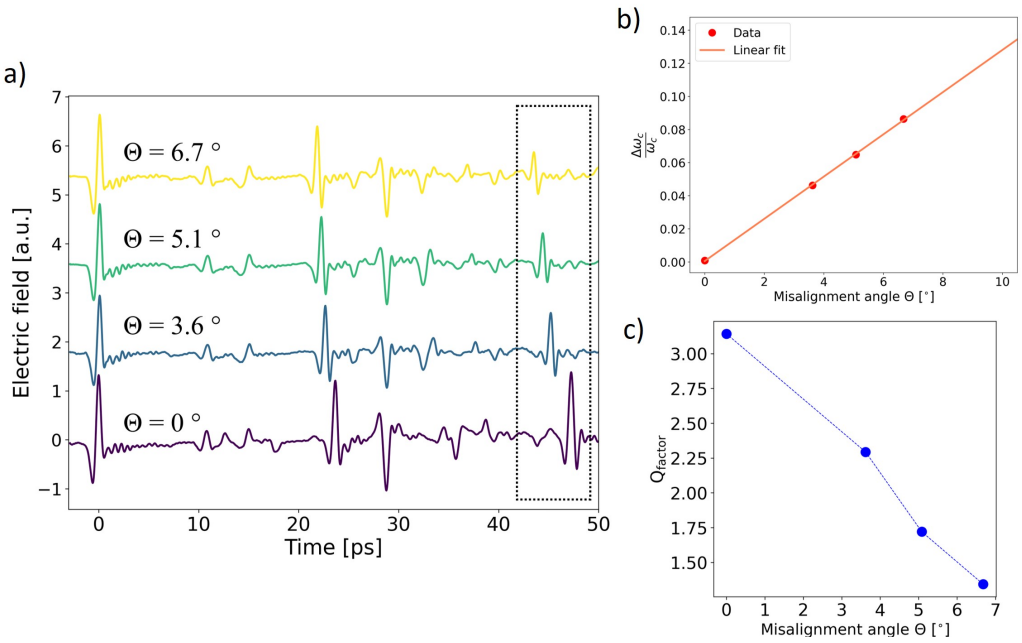

Fig. 6.3 **Variation of the cavity quality factor as a function of the total misalignment angle of the mirrors.** a) THz time domain fields passing through the sample within the cavity for different misalignment angles θ. In the dashed box we highlight the THz reflection associated to the cavity round trip. b) Relative shift of the cavity frequency as a function of the misalignment angle obtained from the THz fields shown in a and corresponding linear fit. c) Estimated cavity quality factor as a function of the misalignment angle. The Q factor has been estimated by approximating the exponential decay of the cavity field with a linear fit. [134]

from the misalignment of the mirrors. It can be seen that, the effective critical temperature move towards the free space value upon increasing the misalignment. The evolution of the critical temperature upon cooling(blue) and heating(red) is plotted in Figure 6.4b as a function of the misalignment angle. In addition to this, Figure 6.4c demonstrates that the hysterisis of the phase transition tends towards the free space hysterisis value when the mirrors are highly misaligned. These observations indicate that renormalization of the critical temperature is associated to cavity environment.

In addition, the shift in the effective phase transition temperature upon cavity misalignment open the possibility to switch between the metallic and the dielectric state by changing the cavity alignment. This has been demonstrated by the time domain terahertz fields in the insets of Figure 6.4a. The temperature of the cold finger has been set at T_{CF}= 154 K and by changing the geometry from misaligned to aligned configuration a transition from insulating to metallic state has been observed at θ= 2.9°. This can be tracked from the vanishing of the CDW phonons (oscillations in the THz time domain) upon tuning θ.

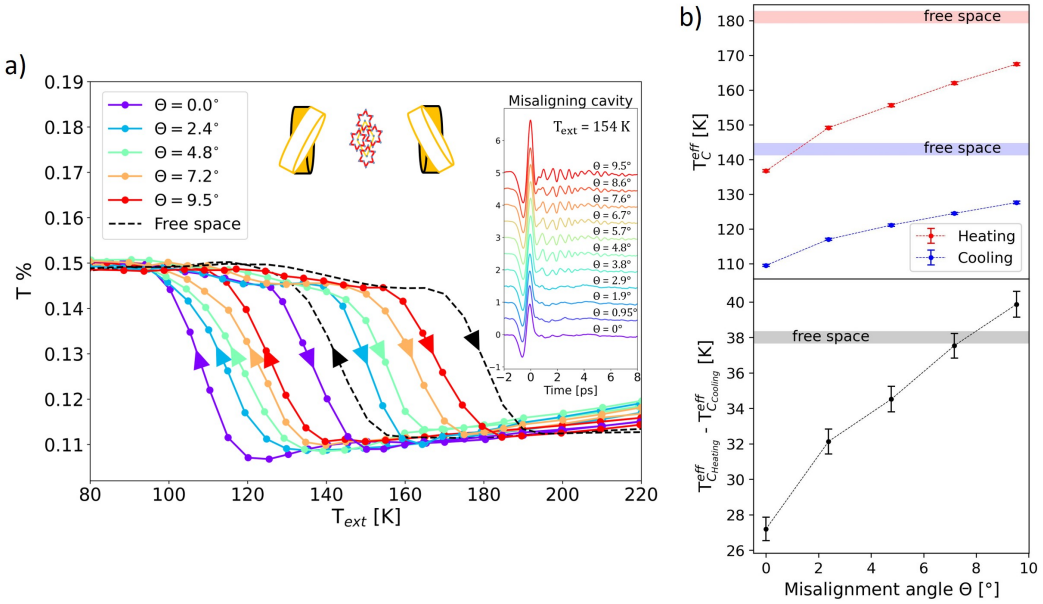

Fig. 6.4 **Dependence of the effective critical temperature on the cavity alignment.** a) Dependence of the metal-to-insulator phase transition as a function of the cavity alignment for the 11.5 GHz cavity. The hysteretic sweeping curves are plotted for each misalignment angle θ as the integrated low frequency transmission (0.2 THz $< \omega <$ 1.5 THz). b) Estimation of the effective critical temperature as a function of the cavity alignment. Top panel: effective critical temperature upon heating (red) and cooling (blue) the sample as a function of the misalignment angle of the cavity. The shaded horizontal lines indicate the free-space reference. Bottom panel: corresponding hysteresis. The black shaded line marks the hysteresis measured in the free space material. [134]

6.2.2 Dependence of T_c^{eff} on Cavity Frequency

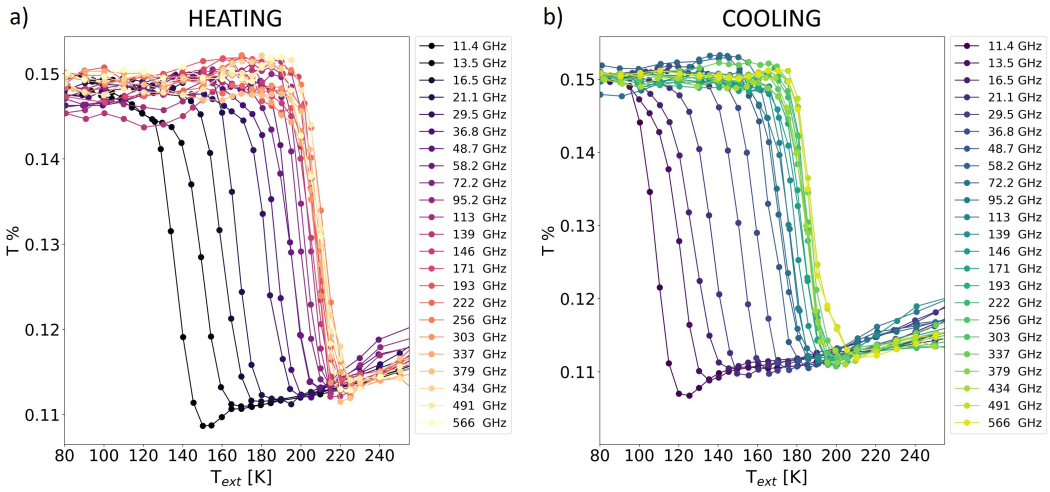

Fig. 6.5 **Temperature hysteretic curves as a function of the cavity frequency.** Low frequency THz transmission (0.2 THz $< \omega <$ 1.5 THz) as a function of the cavity frequency measured upon a) heating and b) cooling the sample. [134]

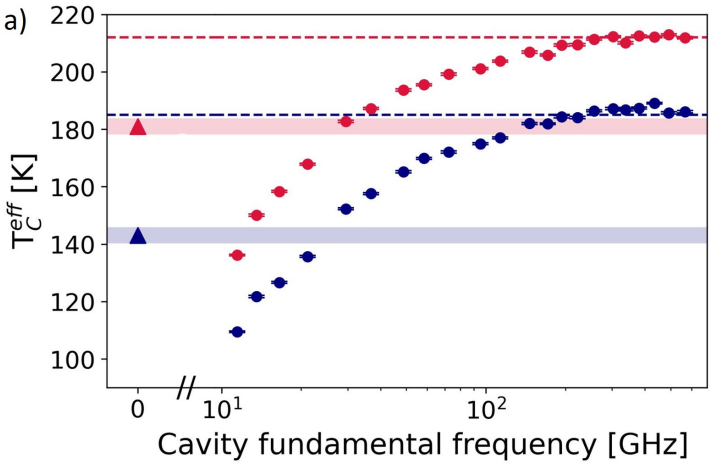

Fig. 6.6 **Cavity-driven renormalization of the effective critical temperature as a function of the cavity resonance.** a) Dependence of the effective critical temperature on the cavity fundamental frequency for the heating and cooling temperature scans. The zero-frequency point represents the free space critical temperature, while the red (blue) dashed line the literature critical temperature [238] for the heating (cooling) temperature scan. The error bar associated to each temperature is the standard deviation of the effective critical temperatures estimated for three consecutive scans. [134]

The influence of the cavity on the effective phase transition temperature can be further verified by changing another aspect of cavity geometry, the fundamental frequency of the cavity. This has been done by tracking the metal-to-insulator phase transition in cavities with resonant frequencies ranging from 11.5 GHz to 570 GHz. The maximum cavity frequency employed here are chosen much below the frequency of the lowest IR-active mode of the C-CDW phase (1.58 THz) in order to disentangle the effects due to the coupling to the IR-active optical phonons.

Figure 6.5a and b shows the temperature dependence of integrated low frequency transmission for cavities with different frequencies upon heating and cooling respectively. It can be seen that the hysteretic curves are shifting towards higher temperatures by reducing the distance between the mirrors and remains the same for cavity frequencies above 200 GHz. The effective critical temperature estimated from the temperature scans in Figure 6.5 is plotted in Figure 6.6a as a function of cavity frequency. The effective critical temperature(T_c^{eff}) inside the cavity shows a non-monotonic trend with respect to the free-space condition, pointing towards a cavity mediated effect. The findings indicate that the long wavelength cavities (up to ~ 25 GHz) effectively stabilize the nearly-commensurate metallic phase, whereas the higher energy cavities stabilizes the insulating C-CDW phase with respect to the material in free space (represented in Figure 6.6a as the zero-frequency point). However, by tuning the cavity across the frequency range in Figure 6.6a we obtained a shift of ~ 75 K in the effective critical temperature(T_c^{eff}). Thus the modification in effective critical temperature (75 K) that is higher than the free space hysterisis(38 K) unveils the possibility for reversible cavity control of metal-to-insulator phase transition in 1T-TaS_2.

The reversible control of phase transition in 1T-TaS_2 by tuning the fundamental mode of the cavity is depicted in Figure 6.7a. The temperature of the cold finger has been fixed at

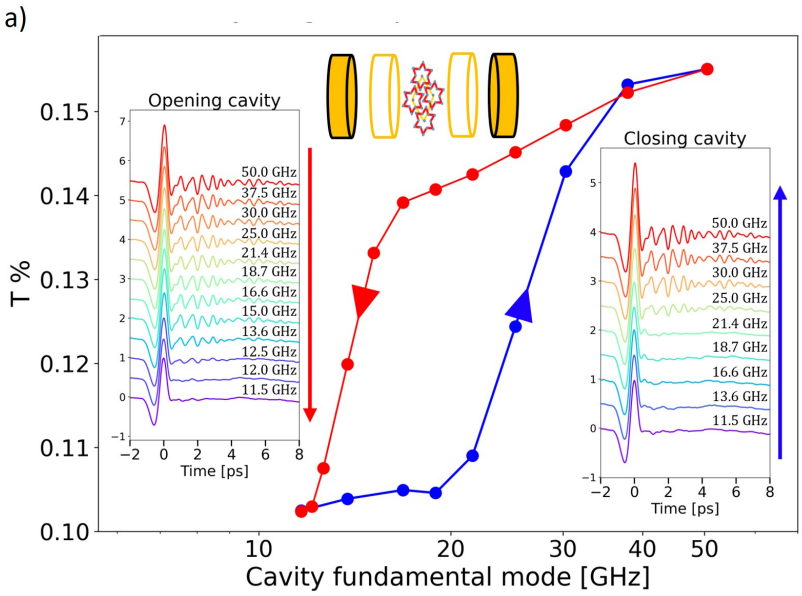

Fig. 6.7 **Reversible cavity control of the metal-to-insulator transition at fixed temperature (150 K) upon tuning the fundamental mode.** a) The hysteresis as a function of the cavity fundamental mode is plotted as the evolution of the integrated low frequency THz transmission (0.2 THz $< \omega <$ 1.5 THz). The insets show the evolution of the time domain THz fields exiting the cavity for different values of the cavity frequency ranging from 50.0 GHz to 11.5 GHz (opening cavity case) and from 11.5 GHz to 50.0 GHz (closing cavity case), demonstrating the reversible switching between the two phases. [134]

T_{CF} = 150 K in order to be in the free space hysteritic curve of the sample. As we mentioned before, the metal-to insulator switch can be tracked from the screening of the CDW phonons in the time domain terahertz field(insets of Figure 6.7a). The evolution of the IR active phonon modes upon closing the cavity reveals a transition from metallic to insulating phase at a cavity frequency of ~ 25.0 GHz and by increasing the cavity length the material switches back to the metallic state at a lower cavity frequency(~ 13.6 GHz). Hence, we obtain the hysteretic behaviour of the low frequency transmission shown in Figure 6.7a by tuning the cavity fundamental mode.

To confirm that the renormalization in the effective phase transition temperature is a cavity mediated effect, it is important to exclude the effects of incoherent heating from the cavity mirrors. A crucial test in this sense will be to perform the same experiment in a condition where the mirrors are significantly hotter than the sample. Indeed, in a simple incoherent thermal scenario we would expect to increase the thermal load on the sample and hence to heat it up. This would result in a decrease in the effective phase transition temperature. Therefore, we mapped the effective phase transition temperature as a function of cavity frequency at different mirror temperatures.

Temperature dependent THz transmission of 1T-TaS_2 embedded in the cavities of frequencies, ω_c = 11.5, 21.2, 48.8 GHz upon heating is shown in Figure 6.8. Figure 6.8a corresponds to the measurements performed with the cavity mirrors at 290 K, while Figure 6.8b were performed in the configuration with cryo-cooled mirrors.

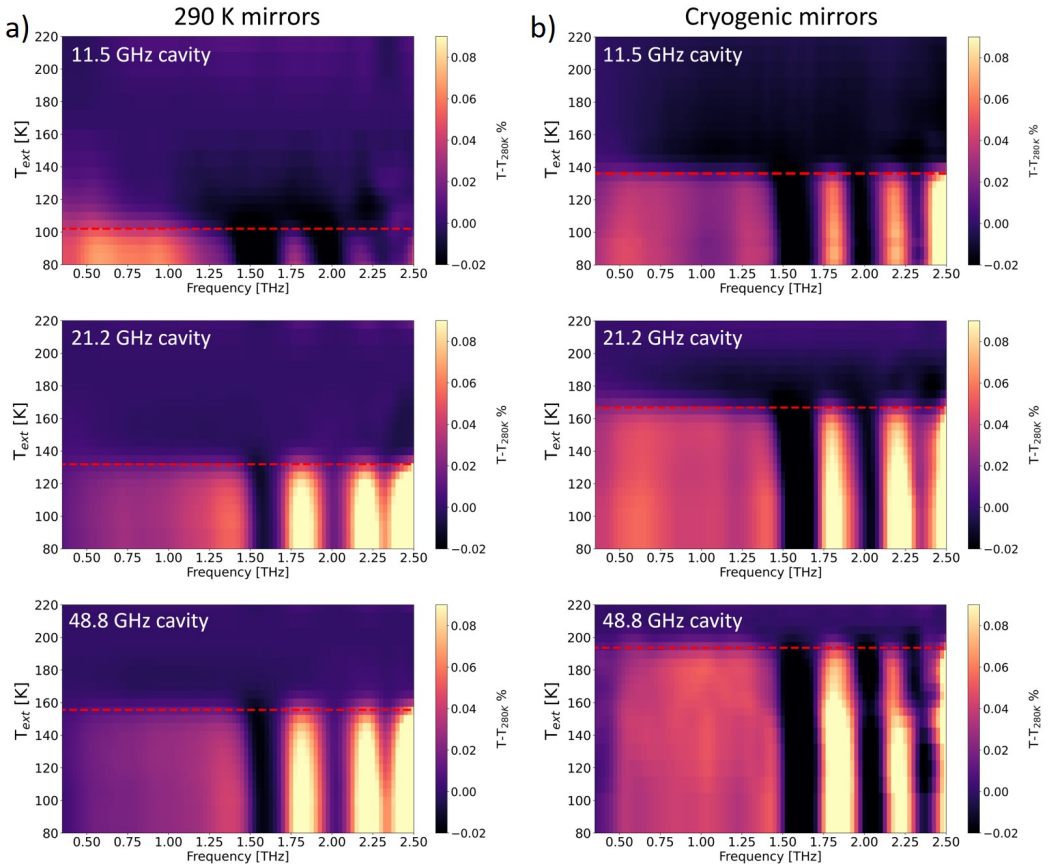

Fig. 6.8 **Dependence of the Effective Phase Transition Temperature on the Temperature of the Cavity Mirrors revealed by THz Spectroscopy.** a) Heating temperature scans for three representative cavity frequencies (ω_c = 11.5, 21.2, 48.8 GHz) in the 290 K mirrors configuration. b) Corresponding heating temperature scans for the cryogenic mirrors configuration.[134]

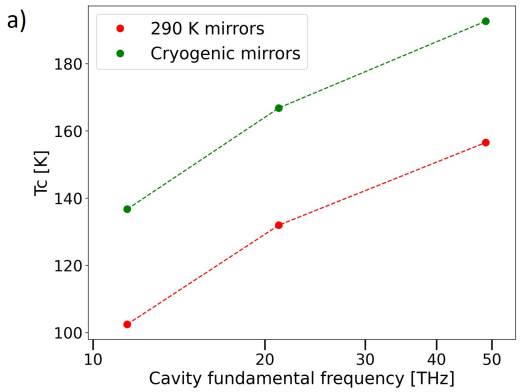

Fig. 6.9 **Dependence of the heating critical temperature on the cavity fundamental frequency for the 290 K and cryogenic mirrors configurations.** a) The effective critical temperature as a function of cavity frequency measured upon heating the sample from the dielectric phase for the cryogenic mirrors(green) and 290 K mirrors(red) configuration. [134]

Figure 6.9a presents dependence of the effective critical temperature on the cavity frequency with the cryo-cooled mirrors (T_{mirr} = 95 K[1]) and 290 K mirrors. The data points out a rigid shift in the effective critical temperature with 290 K mirrors independent of the cavity frequency (~ 35 K). Also, an increase in the effective critical temperature has been observed upon increasing the cavity frequency, displaying a trend which is analogous to the one measured with the cryogenic mirrors. This further verifies that the renormalization in the effective critical temperature originates from the cavity electromagnetic environment.

6.3 Discussion

So far, we have confirmed that the renormalization in the effective phase transition temperature is a cavity mediated effect as the non-monotonic behaviour and the terahertz measurements with the 290 K mirrors cannot be justified by the incoherent radiative heating/cooling of the sample. In the Figure 6.10a, we have demonstarted the phase transition hysterisis curves for low and high frequency cavity settings(ω_c^{low}= 16.7 GHz and ω_c^{high}= 337 GHz). The figure stresses that the change in the cavity frequency results in the shrinking of the hysterisis besides the renormalization of effective phase transition temperture. Hence, the shift in the effective temperature depends also on the thermal cycle of the sample pointing towards a scenario in which the coupling to the cavity is different in the two phases of the material. The shrinking of the hysterisis observed in our results hint towards a context in which the insulating phase is less sensitive to the cavity electromagnetic environment compared to the metallic state. Therefore, we would like to propose that the plausible driving force of the apparent renormalization of the effective phase transition is the coupling between the cavity modes and the EM-active modes of the metallic state in 1T-TaS_2.

Figure 6.10b presents a schematic of the free energies of the metallic NC-CDW phase(F_m) and of the dielectric CCDW phase(F_d) as a function of the temperature in consistent with the hysterisis curves in Figure 6.10a. The crossing temperature between the free energies of the two phases sets the critical temperature of the metal-to-insulator phase transition defined as the centre of the first order transition hysteresis. For simplicity, we assume the free energy of the dielectric phase to be weakly dependent on temperature and subsequently consider the change in the temperature dependence of the free energy of the metallic phase to be responsible for the phase transition.

The cavity mediated effects in the metal-to-insulator transition can be explained using two mechanisms. The first one refers to a change in the energy spectrum of the collective sub-THz modes in the material due to the hybridization with the cavity modes. As shown in the Figure 6.10b(black vertical arrow), the change in the cavity frequency changes the free energy of the metallic phase with respect to the insulating one, resulting in a shift of the transition temperature. The experimental observation would thus suggest that lowering the cavity resonance could cause a decrease of the free energy of the metallic phase resulting in a lower phase transition temperature. The change in the slope of its temperature dependence can be linked to the cavity-driven shrinking of the hysteresis.[134]

[1]This is the lowest reachable temperature of the mirrors for the present experiment, measured when the cold finger is at T_{CF} = 80 K.

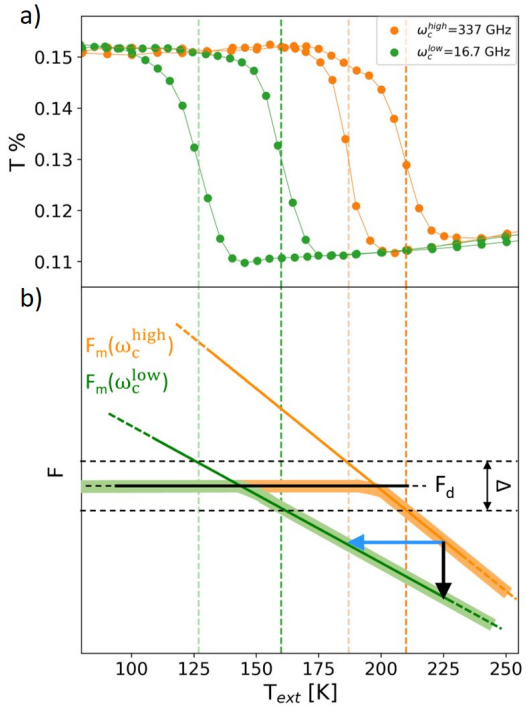

Fig. 6.10 **Cavity-mediated thermodynamics of the metal-to-insulator phase transition in 1T-TaS_2.** a) Comparison of the phase transition hysteresis of 1T-TaS_2 within a low-frequency cavity (ω_c^{low} = 16.7 GHz) and a high-frequency cavity (ω_c^{high} = 337 GHz). b) Schematic temperature dependence of the free energy of the metallic (F_m) and the dielectric (F_d) phase at the cavity frequencies ω_c^{low} and ω_c^{high} employed in a. The activation energy for switching the phase is indicated with Δ. The shift of the apparent transition temperature could be rationalized with a cavity-mediated renormalization of the free energy of the metallic state (black vertical arrow) or with a scaling of the sample effective temperature in analogy with the Purcell effect (blue horizontal arrow). [134]

Second mechanism is a thermodynamical framework based on the mismatch between the temperature of the cold finger(T_{CF}) and actual temperature of the sample(T_S). The emission spectrum of a sample can be altered by reshaping the electromagnetic density of states at the sample position by a cavity. This will result in a cavity mediated change in the temperature of the sample[267] (blue horizonal arrow in Figure 6.10b). For instance, for the studied phase transition, the short cavities move the electromagnetic modes to higher frequency and could effectively decouple the electromagnetic active modes from the vacuum, similarly to the Purcell effect in atomic and molecular physics[6, 7, 245, 246, 134].

The detailed theoretical description of the above mentioned models are given in the subsections(Taken from ref[134]).

6.3.1 Free Energy Picture

In this scenario, we resort to a Dicke-based model with a single cavity mode coupled to a continuum absorption spectrum within the GHz spectral range, where conductivity measurements suggest an increased dielectric response [268, 269]. Importantly, under a

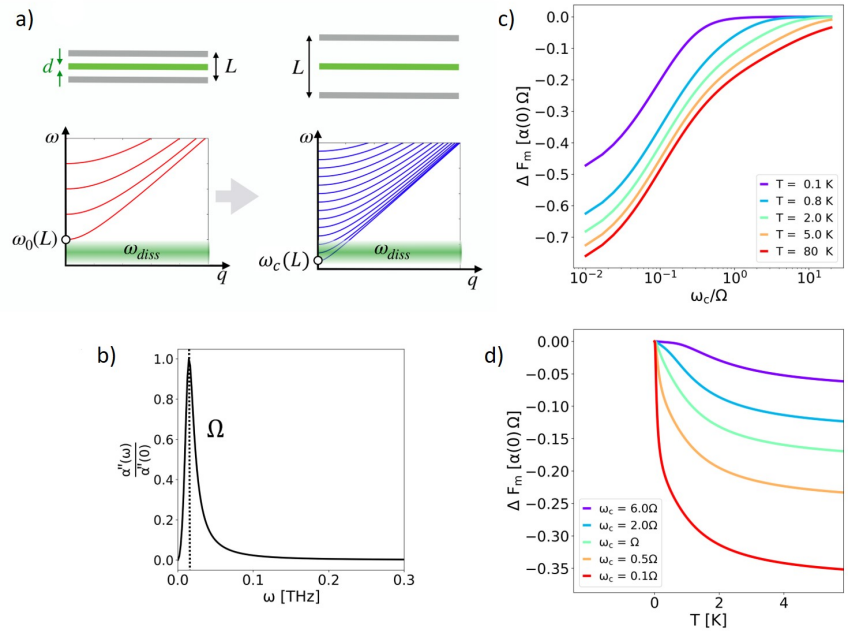

Fig. 6.11 **Cavity-induced renormalization of the free energy of the metallic phase.** a) Free energy model setting. Upper panels: coplanar cavity with a thin slab of matter (thickness d) inside a cavity of length L. Lower panels: Sketch of the cavity modes dispersion and of the absorption solid band (green shaded region centered at ω_{diss}). As L is increased, modes are pulled inside and below the absorption band of the solid. The cavity fundamental mode is indicated with ω_c (L). b) Dielectric loss spectrum $\alpha''(\omega)$ (Ω = 15 GHz, γ = 20 GHz) employed for the calculations. The spectrum has been normalized by the static contribution to the polarizability $\alpha(0)$. c) Renormalization of the metallic free energy ΔF_m as a function of the cavity frequency for different temperatures. The cavity frequencies ω_c are normalized by Ω = 15 GHz. d) Renormalization of the metallic free energy ΔF_m as a function of the temperature for different cavity frequencies above and below resonance $\omega_c = \Omega$. [134]

harmonic approximation for the solid modes, the free energy difference ΔF_m between the light-matter hybrid and the isolated systems can be understood solely in terms of the frequency-dependent polarizability of the solid, irrespective of the microscopic nature of its collective modes.

Let us consider a solid with given dielectric properties, characterized by the polarizability $\alpha(\omega)$ which determines the response of the transverse polarization density to the electric field, $\vec{P}(\omega) = \epsilon_0 \alpha(\omega)\vec{E}(\omega)$. The polarizability $\alpha(\omega)$ is related to the relative dielectric function $\epsilon(\omega)$ as $\epsilon(\omega) = 1 + \alpha(\omega)$. A non-zero polarizability implies that there are modes in the solid which can hybridize with the electromagnetic field, which in turn leads to a change of the free energy when the system is put in the cavity. In order to understand the effect of the cavity on the free energy of the system, we evaluate the difference

$$\Delta F = F_{tot} - F_{mat} - F_{cav} \tag{6.1}$$

between the total free energy of the coupled system (F_{tot}) and the free energies of the uncoupled solid (F_{mat}) and of the electromagnetic field (F_{cav}). A key observation is that as long as the solid is approximately described by a harmonic theory, ΔF can be determined

from the knowledge of the experimentally accessible dielectric function alone, independent of microscopic details such as the precise nature of the electromagnetic activity modes. In short, the reason is that in a harmonic theory one can exactly integrate out the modes of the solid, so that the resulting effective action of the cavity, which then determines ΔF, is given in terms of the linear response functions of matter.

We will make a further simplification in line with the present experimental setting, and assume that the volume V_m of the solid is small compared to the cavity volume V, $V_m/V \ll 1$. This approximation is valid for the experimental setting since the cavities employed have fundamental frequencies in the low THz region, while the sample thickness is $\sim 10\mu m$. With this approximation, as we will show below, for a single cavity mode with fundamental frequency ω_c, the free energy renormalization ΔF due to the light-matter coupling (Equation 6.1) is given by $\Delta F(\omega_c, T) = \frac{V_m}{v} f(\omega_c, T)$, where[134]

$$f(\omega_c, T) = \frac{1}{\pi}\int_0^\infty d\omega\, \alpha''(\omega)\omega \frac{b(\omega_c, T)\omega_c - b(\omega, T)\omega}{\omega_c^2 - \omega^2} \tag{6.2}$$

In the previous equation $b(\omega, T) = (e^{\omega/T} - 1)^{-1}$ is the Bose function and $\alpha''(\omega)$ the imaginary part of the solid polarizability (dielectric loss).

The total free energy change ΔF is a thermodynamically extensive quantity, which arises from the coupling to a continuum of cavity modes with transverse momentum q and a discrete mode index n (Figure 6.11a). For simplicity, instead of summing Equation 6.2 over all cavity modes $\omega_c = \omega_{q,n}$, we will first analyze the single mode result (Equation 6.2) for the lowest cavity frequency ($\omega_c = \frac{\pi c}{L}$, with L the cavity length) to understand the qualitative functional dependence of ΔF on the temperature and on the cavity parameters. In order to estimate the order of magnitude of the total effect of all modes, the result will then be multiplied with a phase space factor that counts the number of modes N_{mode} that are affected by the cavity.

To analyze the free energy renormalization (Equation 6.2), we assume that the solid polarizability $\alpha(\omega)$ gives rise to a broad continuum absorption band that can be fitted by the response of a strongly damped oscillator:

$$\alpha(\omega) = \alpha(0)\frac{\Omega^2}{\Omega^2 - \omega^2 - i\omega\gamma} \tag{6.3}$$

Here Ω corresponds to the central frequency of the material's mode, γ is the linewidth, and $\alpha(0)$ is the contribution of the mode to the static polarizability. The latter also measures the total spectral weight in the absorption band and therefore serves as a phenomenological measure of the effective coupling strength. The dielectric loss $\alpha''(\omega)$ adopted for the estimations is presented in Figure 6.11b. We set a central frequency $\Omega = 15$ GHz and a frequency damping $\gamma = 20$ GHz so that no significant contribution to the solid dielectric loss is present in the THz region ($\omega > 0.1$ THz). We show in Figure 6.11c the dependence of the free energy renormalization of the metallic phase (Equation 6.2) as a function of the cavity frequency ω_c when the latter is swept through the mode centered at Ω. The model indicates that the free energy of the metallic state is lowered upon lowering the cavity frequency, which is qualitatively consistent with the decrease of the effective critical temperature upon

reducing the cavity frequency observed experimentally. The renormalization of the metallic free energy is larger for larger temperatures, indicating that it is related to the thermal population of the low energy mode. We stress that the temperature in the experiment is well above Ω. Figure 6.11d shows the free energy renormalization as a function of temperature for different cavity frequencies ω_c below and above the resonance $\omega_c = \Omega$. The free energy of the metallic phase is lowered and becomes steeper when the cavity frequency is lowered (i.e. opening the cavity). This trend is consistent with the interpretation of the experimental observations from the terahertz measurements.

It should be stressed, however, that the absolute changes of the total free energy are expected to be rather small. As mentioned above, the single mode result $\Delta F(\omega_c, T) = \frac{V_m}{V} f(\omega_c, T)$ should be integrated over all modes or, for a simple estimate, multiplied with a phase space factor N_{modes}. If the latter is simply taken to account for all modes below a certain cutoff ω_{cut} in a volume V, we have $N_{modes} = V\lambda_{cut}^{-3}$ up to constants of order one. Hence the free energy change $N_{modes} \times \frac{V_m}{V} f(\omega_c, T)$ per volume V_m is given by the amount $f(\omega_c, T)$ per volume λ_{cut}^3. The changes of $f(\omega_c, T)$ upon modifying the cavity frequency are of the order of $\alpha(0)\Omega$. (see Figure 6.11c an d), thus corresponding to an energy density $\alpha(0)\Omega/\lambda_{cut}^3$. This value has to be compared with the condensation energy density of the phase transition, which is $Q \approx 6\ J/mm^3 \approx 3.6 \times 10^{10}\ eV/\mu m^3$ [270]. With Ω in the sub-meV range, very large couplings $\alpha(0)$ would be needed, even with a cutoff λ_{cut} in the optical range (which is clearly an upper bound, as optical frequencies are hardly affected by the present cavity setting).

We therefore conclude that although the free energy renormalization in the cavity ΔF follows the correct trend (lowering the free energy of the nearly commensurate phase as the cavity is opened), it is not sufficient to explain the experimental observation. While it will certainly be also interesting to investigate theoretical interpretations which go beyond the harmonic theory, this puts more emphasis on the second mechanism (Purcell-like effect) discussed in the next subsection.

6.3.2 Control of Dissipations through Cavity Electrodynamics

In this section we discuss the Purcell-like scenario mentioned before, i.e. the mechanism in which the observed changes in the effective critical temperature could be related to a cavity control of the dissipations, analogously to the Purcell effect. In this scenario, the reshaping of the electromagnetic density of states at the sample position due to the cavity electrodynamics could result in a modification of the sample's thermal load and subsequently of its temperature. The sample is in thermal contact with the cold finger through the membranes, however it is also in contact with the external photon bath at T_{ph} = 300 K. We assume that the thermal transfer from the cold finger to the sample depends only on the difference between T_{ext} and T_{int} through a cavity-independent thermal coupling constant. Conversely, the thermal load on the sample due to the contact with the external photon bath is mediated by the cavity through a coupling constant depending on the cavity geometry (fundamental frequency ω_c and quality factor Q) and on the sample dielectric loss within the employed cavity range. In order to qualitatively illustrate the mechanism, we model the infrared spectrum of 1T-TaS_2 as a broad continuum absorption band lying in

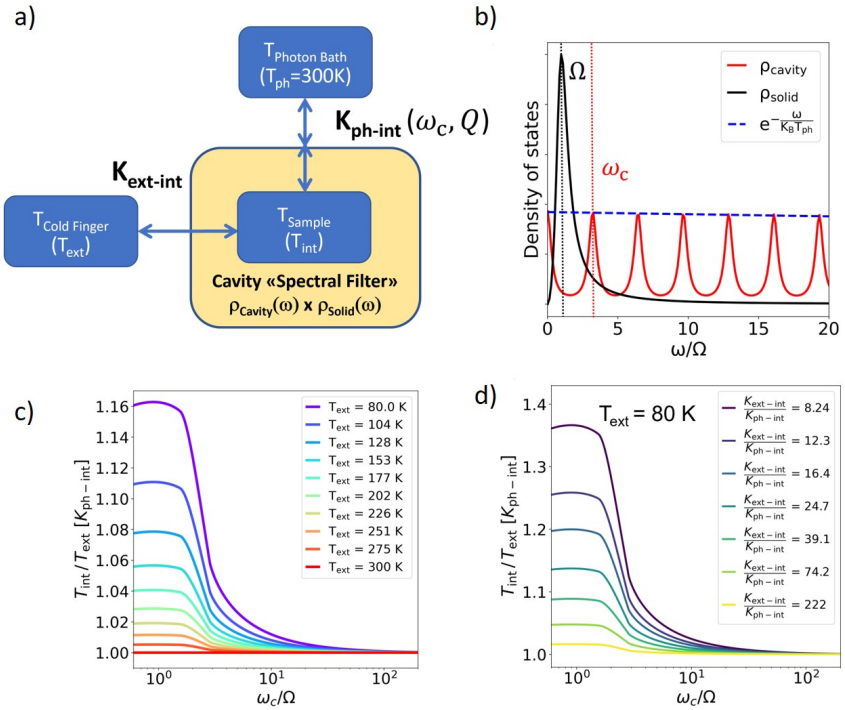

Fig. 6.12 **Cavity control of sample dissipations.** a) Schematic representation of the thermal loads on the sample determined by its coupling with the cold finger through the cavity-independent factor $K_{ext-int}$ and with the photon thermal bath through the cavity-dependent factor K_{ph-int} (ω_c,Q). b) Density of states of the solid (peaked at the mode frequency Ω) and of the cavity (peaked at multiples of the fundamental mode ω_c). The cavity density of states is multiplied by the Boltzmann distribution at the temperature of the photon bath T_{ph} = 300 K. c) Dependence of the temperature ratio $T_{int}(\omega_c, Q)/T_{ext}$ as a function of the cavity frequency for different temperatures of the cold finger T_{ext}. The absolute temperature renormalization scales with K_{ph-int} (ω_c,Q). d) Evolution of the temperature ratio $T_{int}(\omega_c, Q)/T_{ext}$ upon tuning the cavity frequency for different values of the cavity-independent coupling constant $K_{ext-int}$ at a fixed cold-finger temperature T_{ext} = 80 K. The values of the cavity-independent constant $K_{ext-int}$ indicated in the legend have been normalized by K_{ph-int} (ω_c,Q) evaluated at $\omega_c = \Omega$. [134]

the GHz range, and exploit the Purcell-based model to extract an effective temperature of the sample T_{int} (ω_c,Q) depending on the cavity geometry.

In order to estimate this effect, we proceed as indicated in Figure 6.12a. The sample is in thermal contact with the cold finger through the membranes, however it is also in thermal contact with the external photon bath at $T_{ph} = 300$ K. We assume that the thermal transfer from the cold finger to the sample depends only on the difference between the cold-finger temperature T_{ext} and the sample effective temperature T_{int}. Conversely, we assume that the thermal load on the sample due to the contact with the external photon bath is mediated by the cavity, in analogy with the Purcell effect. Under these hypotheses, we can write two rate equations describing respectively the cavity-independent heat flow between the cold finger and the sample:

$$Q_{ext-int} = K_{ext-int}(T_{ext} - T_{int}) \tag{6.4}$$

and the cavity-mediated heat transfer between the sample and the external photon bath:

$$Q_{ph-int}(\omega_c, Q) = K_{ph-int}(\omega_c, Q)(T_{ph} - T_{int}). \tag{6.5}$$

In the previous equations $K_{ext-int}$ represents the cavity-independent coupling constant between the cold finger and the sample, while $K_{ph-int}(\omega_c, Q)$ the coupling constant between the sample and the photon bath, which depends on the cavity geometry, i.e. on the fundamental frequency ω_c and on the quality factor Q.

The coupling constant $K_{ph-int}(\omega_c, Q)$ between the sample and the photon bath can be expressed as the joint density of states of the solid $\rho_{solid}(\omega)$ and of the cavity $\rho_{cavity}(\omega_c, Q)(\omega)$, with the latter multiplied by the Boltzmann distribution at the photon bath temperature $T_{ph} = 300$ K:

$$K_{ph-int}(\omega_c, Q) = \int_0^\infty d\omega\, \rho_{cavity}(\omega_c, Q)(\omega)\rho_{solid}(\omega)e^{\frac{\omega}{k_B T_{ph}}}. \tag{6.6}$$

Considering a continuum broad mode centered at $\Omega = 15$ GHz and with a spectral linewidth $\gamma = 20$ GHz (as for the free energy model described in the previous section), the solid density of states associated to the material's excitations can be expressed through the dielectric loss per unit frequency as:

$$\rho_{solid}(\omega) = \frac{a''(\omega)}{\Omega} = \alpha(0)\frac{\Omega\gamma\omega}{(\omega^2 - \Omega^2)^2 + (\gamma\omega)^2} \tag{6.7}$$

Conversely, the multimode cavity density of states takes the form:

$$\rho_{cavity}(\omega_c, Q)(\omega) = \sum_{n=0}^{\infty} \frac{\gamma_{cav}}{(\omega - n\omega_c)^2 + (\gamma_{cav})^2} \tag{6.8}$$

where γ_{cav} represents the linewidth of the bare cavity which is related to the quality factor Q by the relation $Q = \omega_c/\gamma_{cav}$. The quality factor of the empty cavity is set by the experimental conditions.

In Figure 6.12b we present a plot of the solid density of state and of the cavity density of states multiplied by the Boltzmann distribution at the photon bath temperature $T_{ph} = 300$ K.

Under stationary conditions, the thermal flow from the cold finger to the sample $Q_{ext\text{-}int}$ equals the cavity-mediated heat transfer between the sample and the photon bath $Q_{ph\text{-}int}(\omega_c, Q)$, that is $Q_{ext\text{-}int} + Q_{ph\text{-}int}(\omega_c, Q) = 0$. At equilibrium, we can subsequently calculate an effective sample temperature $T_{int}(\omega_c, Q)$, which takes the form:

$$T_{int}(\omega_c, Q) = \frac{K_{ph\text{-}int}(\omega_c, Q)T_{ph} + K_{ext\text{-}int}T_{ext}}{K_{ph\text{-}int}(\omega_c, Q) + K_{ext\text{-}int}} \tag{6.9}$$

The temperature ratio between the sample and the cold finger $T_{int}(\omega_c, Q)/T_{ext}$ as a function of the cavity fundamental frequency is plotted in Figure 6.12c for different cold-

finger temperatures. We stress that the renormalization of the sample effective temperature scales with the cavity-solid joint density of states $K_{ph-int}(\omega_c, Q)$, and hence with the total spectral weight within the solid absorption band $\alpha(0)$. A larger renormalization of the sample's temperature is hence expected for a larger oscillator strength of the solid's modes.

While the density of states of the electromagnetic field can be enhanced inside the optical cavity with respect to free space, potentially enhancing radiative transitions in materials in resonance with the cavity, shorter cavities move the electromagnetic modes to higher frequencies and could effectively decouple the optically active material's modes from the external field, analogously to the Purcell effect.

We note that, upon increasing the cavity frequency, i.e. by reducing the coupling of the EM active modes from the cavity fundamental mode, the model predicts a decrease of the temperature ratio $T_{int}(\omega_c, Q)/T_{ext}$ resulting in a decrease of the effective temperature of the sample. This trend is qualitatively consistent with what observed experimentally with THz spectroscopy (Fig 4A), i.e. an increase of the effective critical temperature (T_{eff}) upon increasing the cavity frequency.

Moreover, upon lowering the cavity frequency, the coupling between the active optical transitions in the material and light can be enhanced within a frequency range, and the cavity may effectively enhance the absorption of the external blackbody radiation from the sample [6], heating up the sample with respect to free space conditions. Our measurements indicate that the cavity frequency range explored in the experiments is at higher frequencies with respect to the relevant absorption modes in the solid.

As highlighted in Figure 6.12c, the cavity-mediated modification of the sample-photon bath dissipations is more efficient at lower cold-finger temperatures, i.e. when the difference between the temperature of the photon thermal bath (T_{ph}) and T_{ext} is larger. Since the phase transition upon cooling 1T-TaS_2 occurs at a lower temperature with respect to the phase transition upon heating it, we expect the Purcell-like effect to be more efficient in shifting the apparent cooling critical temperature with respect to the heating one. This prediction could justify the effective shrinking of the hysteresis observed by sweeping the cavity mode from lower towards higher frequencies.

In Figure 6.12d, we prove that the trend presented in Figure 6.12c is qualitatively independent on the thermal coupling constant between the sample and the cold finger $K_{ext-int}$. A change in $K_{ext-int}$ in the employed cavity frequency range acts only as a scaling factor of the cavity frequency trend. The results shown in Figure 6.12d has been calculated for a representative cold-finger temperature T_{ext} = 80 K. Lastly, we point out that the renormalization of the sample effective temperature induced by the cavity is more efficient when the thermal coupling between the sample and the cold finger is smaller. At very high thermal couplings $K_{ext-int}$ we expect indeed the contribution to the sample's temperature of the cavity-dependent interaction with the photon bath, and hence the renormalization of T_{int}, to be negligible. Further studies are needed to provide a quantitative estimate of the cavity dependent total radiative heat load experienced by the sample in the optical cavity. An increased sensitivity in this respect could be provided by cavity design featuring a better thermal isolation between the sample and the cold finger.

6.4 Temperature Measurements of the Sample within the Cavity

In order to understand if the effects are associated to free energy renormalization or cavity-mediated heating (cooling) of the sample, we conducted an independent measurement campaign to simultaneously measure sample temperature(T_{int}) and cold finger temperature(T_{ext}) under different cavity configurations. The sample temperature was measured using a micrometric Cr-Al junction.subsection 4.1.4.

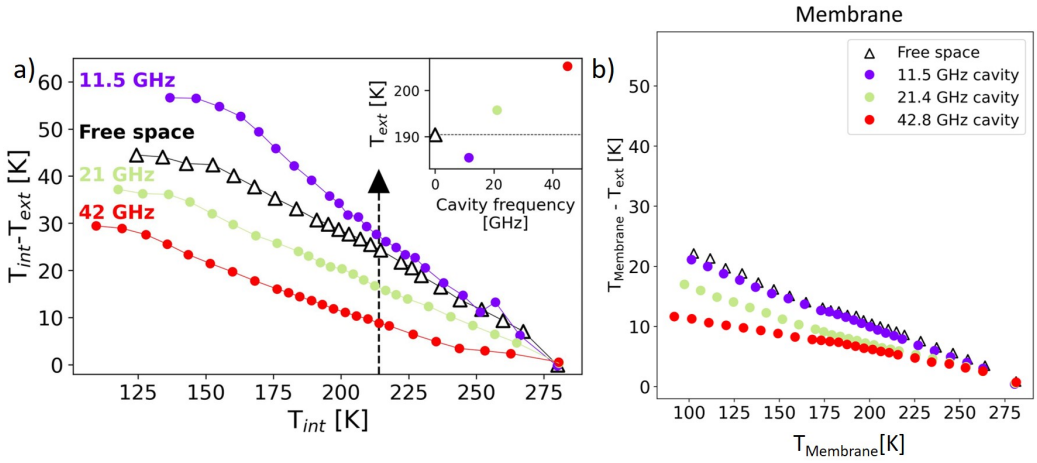

Fig. 6.13 **Temperature measurements within the cavity.** a) Difference between the temperature measured on the sample (T_{int}) and on the cold finger (T_{ext}) as a function of the sample temperature. Temperatures have been measured upon heating the sample from the C-CDW phase. b) Difference between the membrane's temperature and the cold-finger temperature when the thermocouple is held just between the two membranes. [134]

Figure 6.13a presents the temperature mismatch between the sample temperature (T_{int}) and cold finger temperature(T_{ext}) as a function of sample temperature at different cavity lengths and freespace. By increasing the frequency of the cavity, the sample temperature shows a non-monotonic behaviour with respect to the freespace configuration(black). It can be seen that the lower frequency cavities induce a coherent heating of the sample and the coupling with higher energy cavity modes decreases the temperature of the sample with respect to the free space conditions. Closing the cavity effectively corresponds to cooling down the sample that is thus driven to the insulating state. The effect is reversed when, starting from the insulating state. By tracking the T_{ext} at which T_{int} = 210 K (nominal critical temperature of 1T-TaS_2) we revealed a non-monotonic trend as a function of the cavity frequency(inset of Figure 6.13a) consistent with the trend of the effective critical temperature as function of the cavity fundamental mode revealed by THz spectroscopy (Figure 6.6).

Figure 6.13b shows the difference between the membrane temperature($T_{Membrane}$) and the cold finger(T_{ext}) for different cavity lengths. It can be seen that the temperature renormalization of the sample is significantly higher than the one of the membranes. In addition to this, the anomalous non-monotonic behaviour is not observed on the membranes,

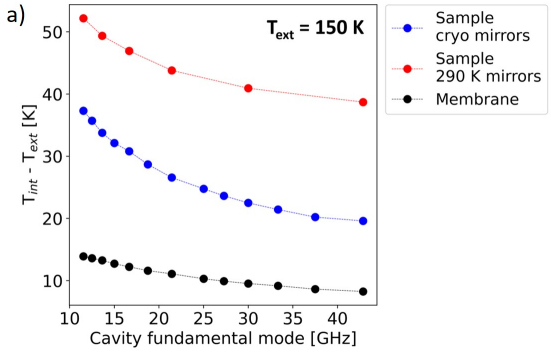

Fig. 6.14 **Temperature measurement within the cavity as a function of the mirrors' temperature.** a) Differential temperature $T_{int} - T_{ext}$ for a fixed cold-finger temperature (T_{ext} = 150 K) as a function of the cavity fundamental frequency. In blue the measurements performed within the cavity with cryogenic mirrors, while in red with 290 K mirrors. In black, for reference, the differential temperature measured within the membranes in the cryogenic mirrors configuration. [134]

where the membrane's temperature measured within the cavity is lower than the free space case for all the cavity frequencies. In particular, we observe that the membrane's temperature measured for the larger cavity length (11.5 GHz) approaches the one of the freespace.

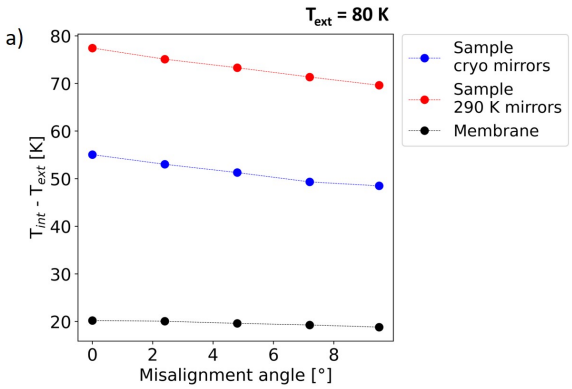

Fig. 6.15 **Temperature measurements within the cavity as a function of the cavity alignment for different mirror temperatures.** a) Differential temperature $T_{int} - T_{ext}$ as a function of the alignment measured for the sample held within cryogenic mirrors (blue) and 290 K mirrors (red). In black, for comparison, the differential temperature measured on the membranes. For the present measurements the cold finger has been set at T_{ext} = 80 K. [134]

Figure 6.14a shows the comparison between differential temperature between the cold finger and the sample when the latter is held between the cryogenic mirrors and 290 K mirrors. A cavity-independent shift of the sample's temperature was observed with 290 K mirrors due to the incoherent thermal load. However, the sample's temperature shows a trend which is crucially analogous for both 290 K mirrors and cryogenic mirrors case upon increasing the cavity frequency. This trend is not consistent with the one measured on the bare membranes, where a ~ 3 times smaller renormalization is observed moving the cavity mode from 11.5 GHz to 42.8 GHz at 150 K.

In order to further verify this effect, we performed the tests by misaligning the cavity similar to the one of terahertz measurements. Figure 6.15a presents a comparison of the differential temperature $T_{int} - T_{ext}$ as function of the cavity alignment in the cryo-cooled and in the 290 K mirrors case. We show that, despite a rigid shift due to the incoherent thermal load introduced by the 290 K mirrors, the renormalization of the sample's temperature due to the cavity alignment is ~ 3.5 times larger than the one measured on the bare membranes for both the configurations. This evidence further excludes that the observed effect is related to the mirror's incoherent heating and hints to a selective effect of the cavity electrodynamics on the sample's temperature.

The above mentioned evidences from the sample temperature measurements suggests that the Purcell-based mechanism may be the dominant effect in the cavity mediated renormalization of phase transition temperature in 1T-TaS_2. Nevertheless, it is interesting to note that both mechanisms predict the correct dependence of the effective critical temperature on the cavity frequency.

6.5 Conclusions

We have studied the impact of cavity electrodynamics on the first order metal insulator transition in a CDW material 1T-TaS_2. The experiment reveals that the effective critical temperature of the CDW phase transition can be controlled by changing the resonant frequency of the cavity and the alignment of the cavity mirrors. The influence of the cavity resonant frequency on the critical temperature has been studied by tuning the cavity frequency from 11.5 GHz to 570 GHz. In the frequency range employed in the experiment, an increase of 75 K has been reported in the effective phase transition temperature. Since the change in effective critical temperature overcomes the free space hysteresis, a reversible control of phase transition has been possible by tuning the fundamental mode of the cavity at a fixed temperature. We have put forward two mechanisms to explain the dependence of the effective critical temperature on the cavity frequency qualitatively. First one has been based on the cavity induced renormalization of the free energies of the metallic phase. The second scenario explores the possibility of modification in effective sample temperature due to a Purcell-based mechanism. The evidences from the experiments performed to measure the actual temperature of the sample along with cold finger temperature proved that the effect is dominated by the modification of effective sample temperature possibly mediated by cavity electrodynamics.

In summary, our approach provides a novel method to explore and manipulate the phase transitions in complex materials. The ability to switch between conductive and insulating states by simple mechanical adjustments opens up new possibilities for developing quantum materials with customizable properties for electronic applications.

7

Cavity Enhanced Nonlinear Responses in Para electric $SrTiO_3$

7.1 Motivation

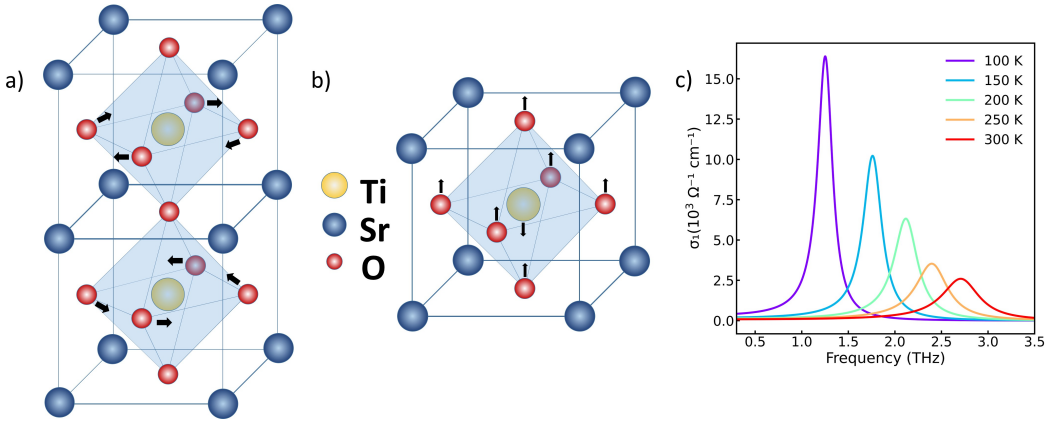

Fig. 7.1 **Atomic Structure of $SrTiO_3$(STO)** a) Anti-ferro distortive rotation in STO at 105 K. b) Soft phonon mode coordinate. c)Temperature dependent THz photoconductivity of the soft mode from ref [271]

The history of ferroelectricity dates back to 1920 when Joseph Valasek discovered ferroelectricity in Rochelle salt[82]. It includes a wide variety of materials including Barium Titanate ($BaTiO_3$) and lead zirconate titanate (PZT). Unlike paraelectric state, the materials in the ferroelectric state has a non-zero intrinsic polarization arising from their non-centrosymmetric structure that can be reversed by the application of an external electric field[272]. The properties of ferroelectrics like high dielectric permittivity makes them a good candidate for high density capacitors[83], for electromagnetical transduction in sensors and actuators[273] and infrared sensors[274]. The characteristics of ferroelectrics include the hysterisis behaviour and curie's temperature above which the material falls in to paraelectric state [83]. Above the phase transition temperature the dielectric permittivity falls of with temperature obeying Curie Weiss law.

The STO crystal belongs to perovskite family in which the materials undergo a ferroelectric transition at low temperatures due to the displacement of transition metal ions from the unit cell center inducing a macroscopic polarization inside the material. While cooling down, the dielectric function increases[275] and the infrared active TO_1 mode undergo softening[276][271]. STO has a cubic perovskite structure at room temperature and undergoes a structural transition to tetragonal symmetry at 105 K as shown in Figure 7.1a due to the rotation of oxygen octahedra with respect to the cubic cell. The term "antiferrodistortive" (AFD) is typically used to describe this transition since it prevents the formation of ferroelectricity in STO [277]. Below soft mode frequency, no dispersion is observed in the permittivity of STO crystal. This indicates that the dielectric properties of STO can be studied and controlled through soft mode dynamics[278]. The TO_1 mode of STO along the Ti-O coordinate is shown in Figure 7.1b which undergoes softening (Figure 7.1c) by lowering temperature following the Curie-Weiss form,

$$\omega_s = \sqrt{A * (T - T_c)} \tag{7.1}$$

The ferroelectric transition happens at 36 K in STO. In the case of STO, nuclear quantum fluctuations prevent long range FE ordering at low temperature and material goes into a quantum paraelectric (QPE) phase [279, 280, 132]. The pathway between different phases in STO is associated to the anharmonic soft mode with large oscillator strength at low temperature [281]. There have been various efforts to drive the soft mode in to anharmonic regime using intense terahertz pulses resulting in reported effects such as nonlinear coupling with high frequency phonon modes [249] and THz field induced ferroelectricity [132]. In addition, the ferroelectricity has been achieved in STO through isotope substitution ($16O \rightarrow 18O$; $Tc = 25$ K) [118] or Ca-substitution [Sr $\rightarrow$ Ca; Curie Temperature (Tc) = 37 K] [116], strain with ferroelectricity upto room temperature [282], [125] and by resonant excitation with intense terahertz pulses [132].

The theoretical frameworks proposed by Latini et al. [38] and Ashida et al. [37] has discussed the ferroelectricity of STO in a cavity environment. Latini et al. [38] investigates the effect of coupling between quantum vacuum fluctuations and matter in collective phase of STO and the resulting stabilization of ferroelectric ground state. Atomistic calculations shows that the off-resonant dressing of the lattice of STO with cavity photons suppresses nuclear quantum fluctuations, effectively leading to the enhancement of the effective mass of ions and a transition to ferroelectricity providing a revised phase diagram of $SrTiO_3$ inside the optical cavity. Ashida et al. [37] emphasizes on controlling many-body states of matter using quantum light without external pumping. The paper focuses on modifying the electromagnetic environment's quantum fluctuations in order to change the physical properties of materials. It explores the dipolar quantum many-body system embedded within a cavity and develops a theoretical model based on quantum light-matter interaction to control its equilibrium state.

In this chapter, we present a possible enhancement of the non-linear terahertz response of paraelectric $SrTiO_3$ bulk crystal when embedded within a Fabry-Perot optical cavity. We have performed THz field dependent study at different temperatures on a 100 μm thick $SrTiO_3$ (100) crystal with dimensions 10 mm X 10 mm embedded inside an optical cavity. The measurements have been performed using high intense terahertz pulses generated from

a $LiNbO_3$ crystal. Our transmission results inside the cavity exhibit a THz field dependence resembling the nonlinear response reported in Katayama et al. [281] at much lower electric field strengths.

7.2 Terahertz Response of Bulk $SrTiO_3$

7.2.1 Temperature Evolution of Soft Mode

We performed time-domain THz spectroscopy to understand the temperature dependent soft mode dynamics of STO. We present in Figure 7.2 THz transmission of STO in free space at different temperature capturing the softening of the TO_1 mode.

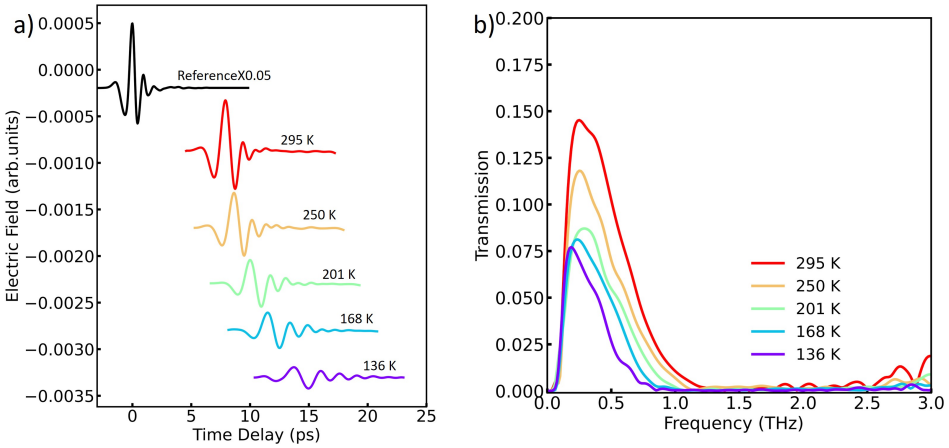

Fig. 7.2 **Temperature evolution of THz in Bulk $SrTiO_3$(STO)** a) Temperature dependent transmitted pulses from Bulk STO. b) Amplitude of the complex transmittance of STO calculated from data shown in Figure 7.2a.

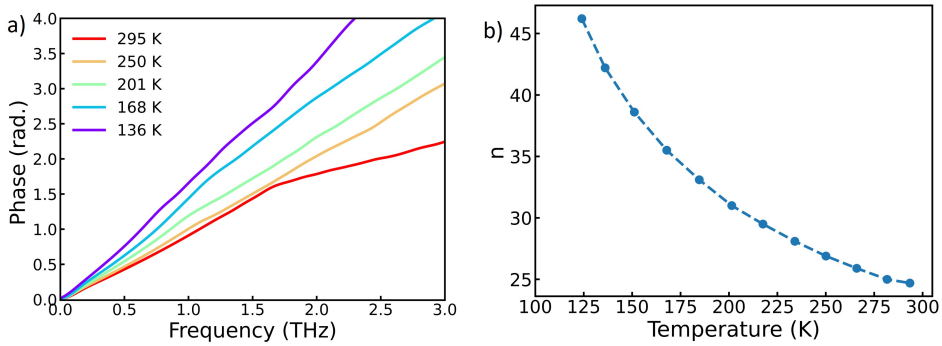

Fig. 7.3 **Terahertz Characterization of Bulk $SrTiO_3$(STO)** a) Phase of the complex transmittance of STO calculated from data shown in Figure 7.2a. b) Temperature dependent refractive index extracted from the THz delay.

The temperature dependent terahertz transmission spectrum of bulk STO for different temperatures is depicted in Figure 7.2b along with the corresponding terahertz waveform and reference in the Figure 7.2a. The terahertz field transmitted through the bulk STO

shows a decrease in the amplitude and an increase in the oscillation period indicating the temperature response of the soft mode. The terahertz pulse is delayed by 7.9 ps at room temperature and further delayed by 5.83 ps with respect to the reference waveform by cooling down from room temperature to 136 K. This corresponds to an estimated change in the refractive index of approximately 16.5. The refractive index estimated from the delay of terahertz pulse is plotted in Figure 7.3b which is in good agreement with the refractive index extracted from the temperature dependent THz- TDS measurements shown in Figure 7.4c. The complex THz transmittance of the STO in the frequency domain has been calculated as $T(\omega) = E(\omega)_{STO}/E(\omega)_{ref}$. The amplitude and phase of the terahertz transmittance is shown in Figure 7.2b and Figure 7.3a. The loss in the terahertz transmission spectra results from the high dielectric permittivity at low temperatures. The room temperature transmission drops to zero at 1.25 THz due to the presence of soft mode with large oscillator strength. However, this value doesn't correspond to the frequency of the soft mode. Due to the limitations arising from the incident terahertz spectral content above 1.5 THz and high dielectric strength of the soft mode the response of the TO_1 mode is observed as an absorption edge in the transmission spectra. This feature has been observed to be shifting to lower frequency which can be associated with the softening of TO_1 mode.

7.2.2 Estimation of Optical Constants

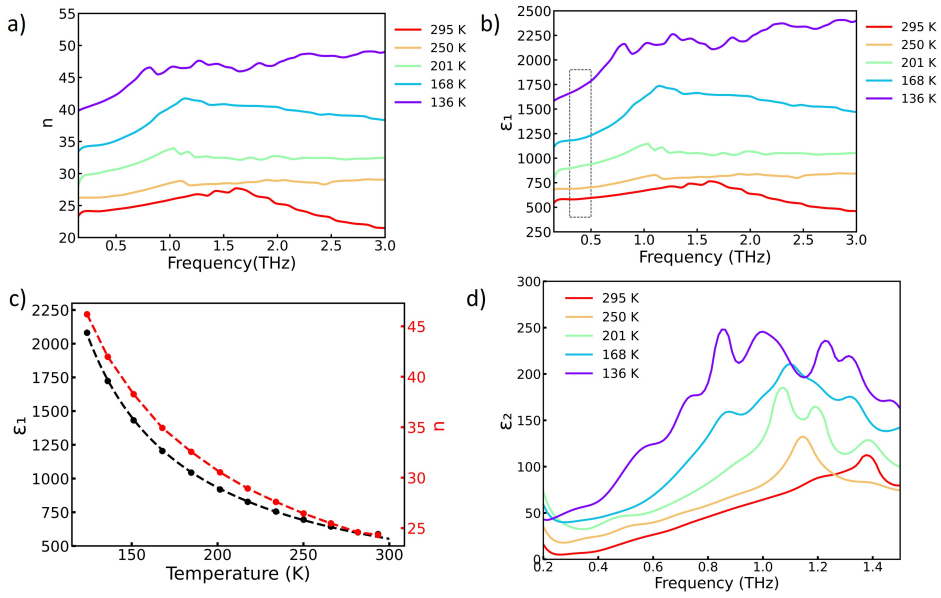

Fig. 7.4 **Optical constants of Bulk STO** a) Frequency dependent refractive index.b) Real part of the dielectric response function for the STO. c) Static dielectric constant(black) and refractive index(red) as a function of temperature (extracted from complex transmittance). d) Imaginary part of the dielectric response function for the STO.

The transfer function based on fresnel's equation has been used to estimate the frequency dependent refractive index [285] at different temperatures. Using the approximation for thick samples, Fabry-Perot effect can be ignored by separating the echoes and using just the first echosubsection 4.2.3. The frequency dependent refractive index in Figure 7.4a increases at low temperature. The bump moving to lower frequency at low temperature

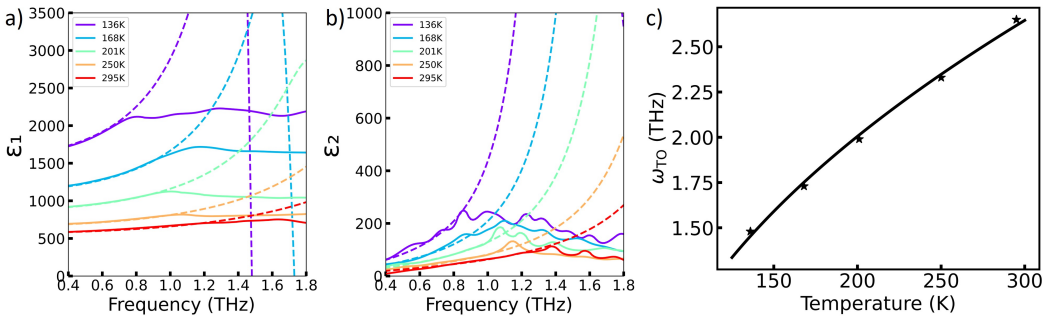

Fig. 7.5 **Soft mode frequency in Bulk STO** a) Real part and b) Imaginary part of dielectric function fitted with classical oscillator model[283, 284] (fits are shown as dotted plots). c) Temperature dependent soft mode frequency estimated from the dielectric response function.

T (K)	136 K	168 K	201 K	250 K	295 K
ω_{TO} (THz)	1.48	1.73	1.99	2.33	2.65
γ_{TO} (THz)	0.18	0.25	0.33	0.45	0.58
ϵ_0	1610	1130	880	670	572

Table 7.1 Parameters used for the fits of the frequency dependent dielectric response of STO

attributes to the softening of the low frequency IR active mode. The frequency-dependent complex dielectric function of $SrTiO_3$ is determined from the complex refractive index through the relationship $\epsilon(\omega) = (n + ik)^2$. Since there are no significant changes in refractive index and dielectric permittivity below soft mode frequency, the static refractive index and dielectric constants are determined from the low frequency response. The temperature dependence of these parameters is shown in Figure 7.4c. The static dielectric constant calculated from the measurements are in good agreement with the bulk STO values from Fedorov et al. [271] and temperature dependence follows Curie-Weiss law, $\epsilon_0 = C/(T - T_c)$ with Tc = 63 K. and C= 12.2 x 10^4 K. Figure 7.4d shows the complex part of dielectric constant which has a behavior that is consistent with that of a damped harmonic oscillator model at low frequencies.[283, 286, 287]. Using this model the complex dielectric function can be defined as[284],

$$\epsilon(\omega) = \epsilon_\infty + \frac{(\epsilon_0 - \epsilon_\infty)\omega_{T0}^2}{\omega_{T0}^2 - \omega^2 - i\gamma_{TO}\omega} = \epsilon_r + i\epsilon_i \tag{7.2}$$

where, ϵ_∞ is the dielectric constant at infinity, ϵ_0 is the static dielectric constant, ω_{TO} is the frequency of the soft phonon mode and γ_{TO} is the corresponding damping constant. The low frequency response of real and imaginary parts of dielectric constants fitted with this model (dotted lines) is shown in Figure 7.5a and Figure 7.5b. The $\epsilon_\infty = 5.6$ for bulk STO[271] has been used for the fitting. ω_{TO}, γ_{TO} and ϵ_0 values for different temperatures are shown in Table 7.1. The temperature dependent frequency of the phonon mode shown in Figure 7.5c can be fitted with the Equation 7.1 with a $T_c = 65$ K and $A = 2.98$ x 10^{22} $s^{-2}K^{-1}$.

7.3 THz Response of $SrTiO_3$ inside Optical Cavity

STO has very high dielectric constant, especially at low temperatures, which significantly influences its optical properties. The high dielectric constant leads to most of the incident terahertz radiation to be reflected rather than transmitted or absorbed. Figure 7.6a shows the reflectivity of the STO crystal at different temperatures obtained from the dielectric function shown in Table 7.1. It can be seen that, STO's exceptionally high reflectivity (~ 0.85 to 1) within the terahertz range employed in the measurements causes it to function similar to a mirror.

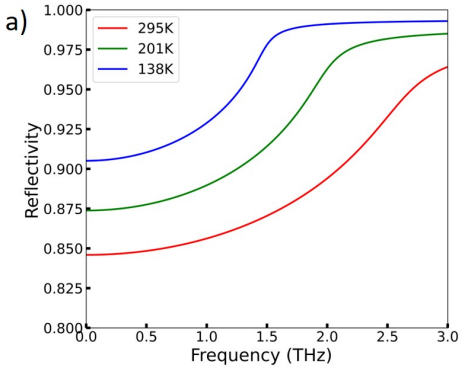

Fig. 7.6 **Reflectivity of STO Crystal obtained from the Dielectric Function.** a) Frequency dependent reflectivity of STO for different temperatures (Estimated from the data shown in Table 7.1)

In order to understand the effect of cavity electromagnetic environement on the STO, we embedded the sample inside an optical cavity. Due to the high transmission loss of STO, the interference effects of the two cavities formed between the sample and the respective mirrors will be more prominent in the terahertz response compared to the one of actual cavity in which the sample is embedded. The sample has been placed at center of the cavity resulting in a constructive interference of the reflections from the two cavities. So, the resonant frequency we refer to in this chapter corresponds to the cavity between the sample and the mirrors.

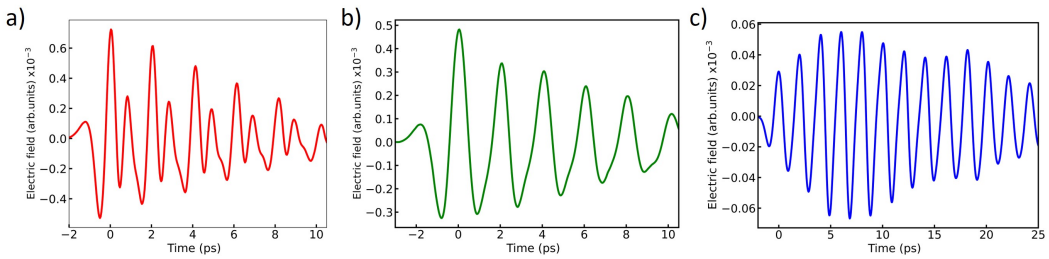

Fig. 7.7 **Transmitted Terahertz Field of STO inside the Fabry Perot Cavity.** Transmitted time domain terahertz field of a) an empty cavity(ω_c=500 GHz) b) First mirror and STO (T=295 K) c) STO (T=295 K) embedded at the middle of the optical cavity. The distance between the sample and mirrors are set in order to have a resonant frequency 500 GHz(cavity between the sample and the mirror)

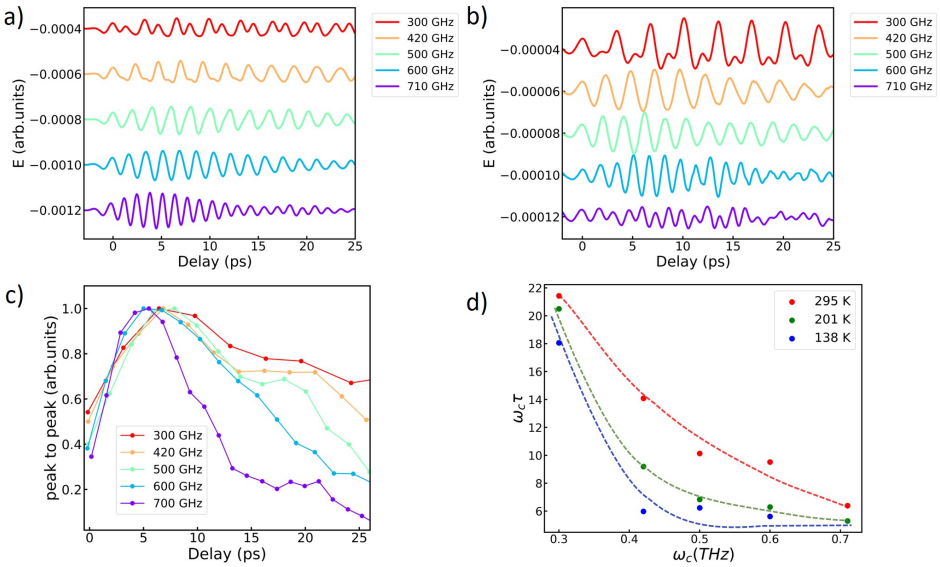

Fig. 7.8 **Temperature Dependent Terahertz Response of STO embedded inside an Optical Cavity** Transmitted terahertz time domain pulses at different cavity frequencies a) For T= 295 K b) For T= 138 K. c) The peak to peak amplitude of the Fabry Perot reflection of the terahertz waveform at 295 K as a function of time delay. d) Ratio between the cavity frequency and decay rate(estimated by fitting peak to peak amplitude by a exponentially decaying function) as a function of fundamental mode of the cavity at different temperatures providing a quantity closely similar to the quality factor.

Figure 7.7c depicts the time domain terahertz field transmitted from the STO inside the cavity for resonant frequency 500 GHz at sample temperature T= 295 K. The first few reflections of the Fabry Perot are more intense than the first transmitted pulse as they are emerging from the interference of two cavities and the Fabry Perot reflections are sustained for a longer duration. For comparison, we have plotted the transmitted terahertz field of an empty cavity(Figure 7.7a) and that of first mirror and the sample(Figure 7.7b)[1]. The Fabry-Perot reflections between the sample and the first mirror shows a similar decay as that of an empty cavity. Therefore, when STO is embedded in the middle of a cavity the interference of the two exponentially decaying fields from the two cavities should result in a field with same decay function, only its intensity will vary based on the amplitudes and phases of the individual fields. Hence, longer lifetime of the terahertz field in Figure 7.7c cannot be simply explained by the interference effects of the two cavities. However, the longer decay time of the terahertz electric field emitted from an STO placed inside the cavity can be possibly related to the spatial redistribution of density of states inside the cavity. The highly reflective surfaces of STO shape two cavities, one on each side of the sample. Similar to the way in which local density of states are reduced on the surface of a highly reflective cavity mirror, local density of states will be strongly suppressed at the sample position due to the developed cavities on both sides of the sample[288]. This would result in an average reduction in the emission and hence longer decay time.

Figure 7.8a and Figure 7.8b depicts the time domain terahertz field transmitted from the system at different resonant frequencies for sample temperature 295 K and 138 K respectively.

[1]Second mirror of the cavity is removed to disentangle the interference effects of two cavities.

The transmitted terahertz field is decaying faster at lower temperature and at high frequency cavities. The peak to peak amplitude of the terahertz field(T=295 K) at different cavity frequency is shown in Figure 7.8c as a function of delay which clearly demonstrates the faster decay of the cavity field at higher frequencies. We couldn't map the complete decay of the field due to the reflections emerging from the experimental setup after 25 ps. Due to this limitation the decay rate of the field has been estimated for each cavity frequency by fitting the THz peak to peak amplitude with an exponentially decaying function. The Figure 7.8d depicts the ratio between the cavity frequency and decay rate as a function of fundamental mode of the cavity at different temperatures providing a quantity closely similar to the quality factor. The data implies that cavity field dissipates faster in high frequency cavities. The increase in the dissipation of the cavity field at higher frequencies can be possibly mapped to the coupling between the cavity field and soft phonon mode. Therefore, at lower temperatures the decay rate is enhanced due to the softening of the phonon mode.

7.4 Nonlinear Terahertz Spectroscopy of $SrTiO_3$ in Optical Cavities

The anharmonicity of the soft mode in STO has been exploited for nonlinear coupling with high frequency phonon modes[249] and terahertz field induced ferroelectricity[132]. As an effort to attain the anharmonic regime of the soft mode the nonlinear responses of the soft mode inside the cavity has been studied by tracking a terahertz field dependent responses of the sample.

7.4.1 Intensity Dependence of Bulk STO

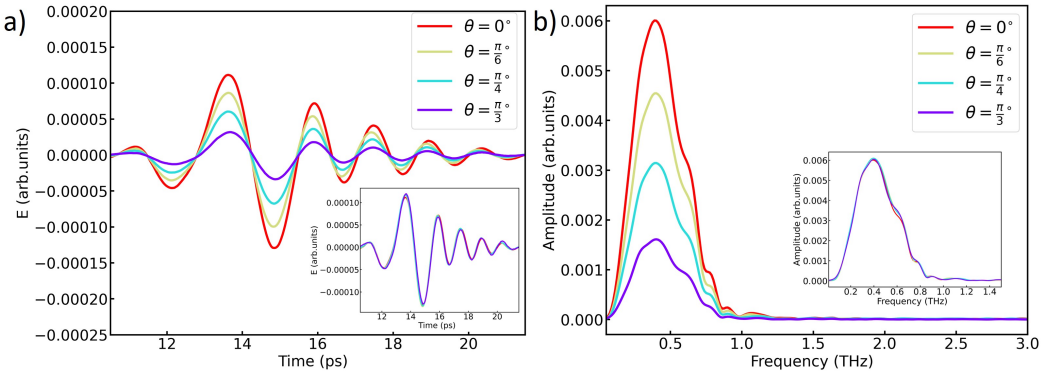

Fig. 7.9 **Terahertz field dependence of Bulk STO at T= 138 K** a) Terahertz waveform and b) Amplitude of the FFT of the transmitted terahertz field from STO (T=138 K) at different $\Delta\theta$ of the polarizers (Normalized with $\cos^2(\Delta\theta)$ is shown in the inset. $\Delta\theta$ refers to the rotation of the axis of the first polarizer with respect to the second one).

The response of the bulk STO towards THz electric field was studied by altering the incoming terahertz intensity as an effort to control and probe the anharmonicity of IR-active soft phonon mode. The experiments were performed by attenuating the terahertz amplitude

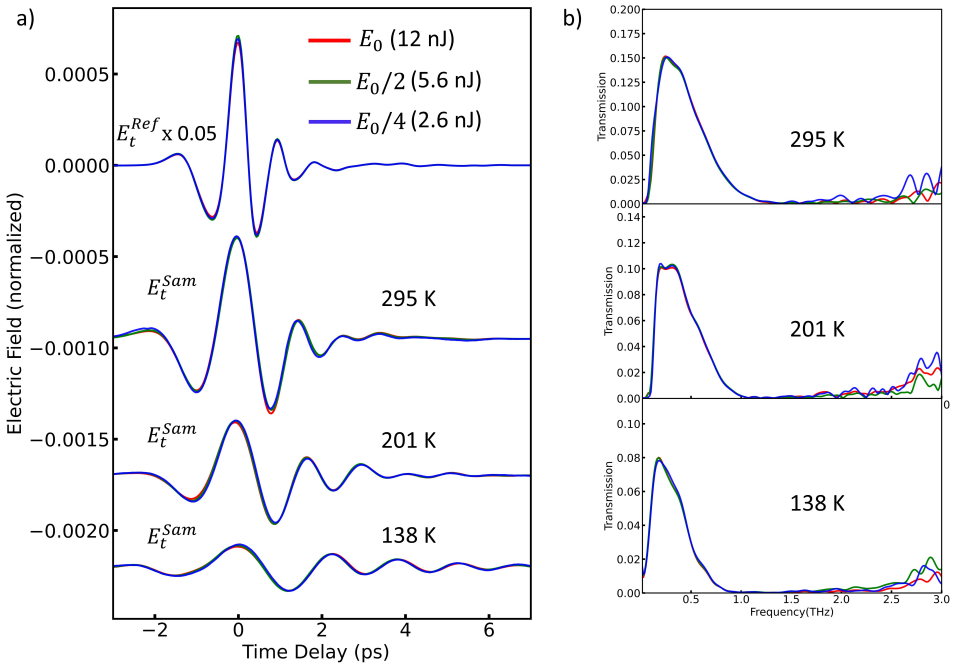

Fig. 7.10 **Nonlinear THz studies of Bulk STO.** a) THz waveforms at different electric field strengths (normalized with the THz peak of the reference). Reference (Top), STO at T= 295 K and STO at T= 201 K (Middle), STO at T= 138K (Bottom). b) Corresponding Transmission spectrum of the THz fields at different temperatures.

on the sample with a pair of wire grid polarizers. The THz beam was almost normal to the sample surface and set to vertical polarization throughout the experiment. Another pair of wire grid polarizers were placed after the sample to eliminate the nonlinearity on the detection crystal. The detailed description on elimination of nonlinearities from the detection crystal is shown in section 4.3. The incident terahertz electric fields on the sample (before the attenuation at the detection crystal) at different intensities are shown in Figure 4.14a. The peak terahertz field on the sample is 5.3 kV/cm when the axes of two polarizers are aligned parallel(section 4.3).

The transmitted terahertz field from a bare STO crystal at 138 K in the time and frequency domain for different angles of the first polarizer is shown in Figure 7.9a and Figure 7.9b. The $\Delta\theta$ mentioned in the labels are the rotation of the axis of first polariser with respect to the second polarizer. In the inset of Figure 7.9a and Figure 7.9b the terahertz pulses and the amplitude of FFT are normalized with the factor $\cos^2(\theta)$ according the Malus's law of polarization. Even at lower temperature the transmitted terahertz pulses overlaps which denotes that there are no nonlinearities associated to the sample or the detection crystal in this experimental configuration.

The response of the bulk STO sample towards different terahertz electric field (E_0= 5.3 kV/cm) is illustrated in Figure 7.10a and Figure 7.10b for sample temperature T=295 K, T=201 K and T= 138 K. The terahertz waveforms at different temperature are shifted horizonatally by the delay of the sample at respective temperatures. The transmitted THz waveform (Figure 7.10a) from STO at room temperature (295 K) and low temperatures (201 K and 138 K) is normalized with the quantities used to rescale the respective reference

amplitudes on the top. Figure Figure 7.10b shows the transmission spectra calculated from the frequency domain of the THz pulses in Figure Figure 7.10a. For all the three temperature settings transmission from STO shows very little change with an increase in the incident terahertz field. Hence, these observations indicate that the nonlinear regime of the soft mode in STO cannot be attained in the freespace with the terahertz field employed in the experiment.

7.4.2 Evolution of Nonlinearity inside Optical Cavity

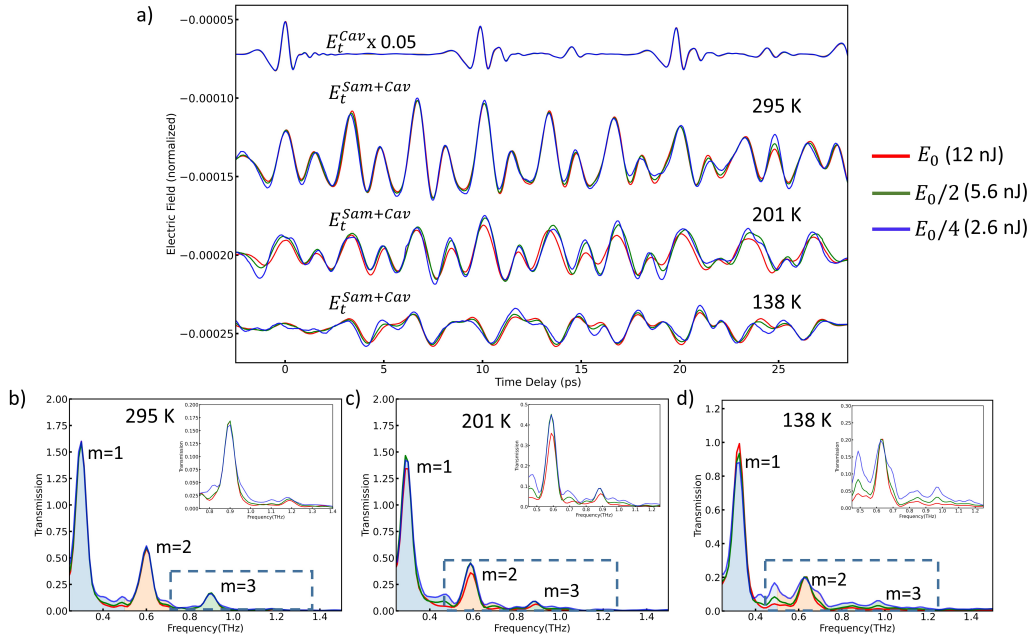

Fig. 7.11 **Nonlinear responses of STO inside the cavity (ω = 300 GHz).** a) THz waveforms transmitted from the cavity at different electric field strengths. The terahertz waves from the sample inside the cavity is normalized with the respective THz pulses from an empty cavity(top) with ω_c=200 GHz. Empty cavity (Top), STO in 300 GHz cavity at T= 295 K and T= 201 K (Middle), STO in 300 GHz cavity at T= 138K (Bottom). b) Corresponding Transmission spectrum of the THz fields at different temperatures T= 295 K, c)T= 201 K and d)T= 138 K. The colour shaded area corresponds to the respective harmonics(m=1(blue), m=2(orange) and m=3(green)) (Plots inside the rectangle are shown in the inset).

In order to study the influence of electromagnetic environment on the nonlinear soft phonon mode, STO was embedded at the center of an optical cavity with quality factor Q ~ 4.9 and the terahertz field on the sample has been controlled using a pair of wire grid polarizers. The pair of wiregrid polarizers before the detection crystal has been removed for the measurements inside the cavity in order to ensure good signal to noise ratio. This has been possible because the transmitted terahertz field from the bare cavity is already in the linear regime of the detection crystal. The details about the cavity characterization and the nonlinearities of the setup are given in section 4.3.

The Figure 7.11a shows the field dependence of transmitted terahertz field of an empty cavity (200 GHz) (top) and STO inside the cavity (300 GHz) at three different temperatures, T= 295 K, 201 K and 138 K (top to bottom). The reference fields from the empty cavity at

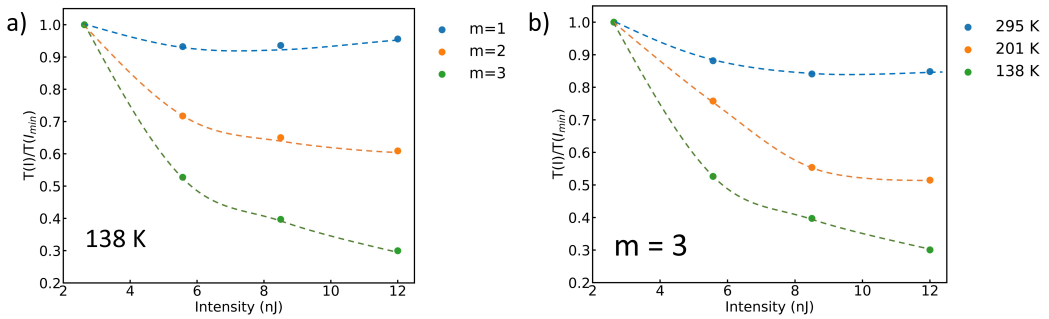

Fig. 7.12 **Evolution of non linearity in STO inside the cavity (ω = 300 GHz)** a) Integral of transmission in Figure 7.11 at different harmonics of the cavity as a function of THz intensity. The integral is calculated for the areas that are shaded with the corresponding legends. (Temperature of the sample=138 K). The transmission at each frequency is normalized by the integral of lowest electric field. b) Integral of transmission(normalized by the integral of lowest electric field) at higher harmonic(m=3) plotted as a function of THz intensity at different temperatures.

different intensities are normalized using Malus's law. From the figure, it is clear that the terahertz electric field doesn't have any influence on the empty cavity. As we mentioned before, STO is highly reflective in the terahertz range which results in the formation of a double cavity when the sample is placed in the middle of a cavity. The multiple reflections in the terahertz waveforms (cavity+sample) shown in Figure 7.11a emerges from the interference of two cavities of resonant frequency 300 GHz. This makes the intensity of the Fabry Perot reflections higher than the first pulse transmitted. So the resonant frequency we refer to correspond to the frequency of the cavity between sample and the mirrors. The transmitted terahertz pulses from the STO inside the cavity at different intensities have been normalized with respect to the corresponding reference amplitudes from an empty cavity at temperatures T=295 K, T=201 K and T=138 K. Contrary to measurements done in free space, the transmitted terahertz pulses doesn't overlap and shows a significant intensity dependence inside the cavity. In addition, this nonlinear response is higher at low temperatures. The terahertz waveform at low temperature shows clear changes in the intensity and shape of the terahertz pulse indicating the temperature dependence of the nonlinearity.

The nonlinear responses can be observed also in the amplitude of the transmittance shown in Figure 7.11b, c and d(295 K, 201 K and 138 K respectively) which are calculated from THz waveforms in Figure 7.11a. The peaks in the terahertz transmission corresponds to the fundamental and higher harmonic frequencies of the cavity between sample and the mirror. The area under each harmonics (m= 1, 2, and 3) is shaded with different colours(blue, orange and green). The results reveal that at lower THz amplitude the transmission is higher compared to the one at higher amplitudes. Moreover, the effect appears to be more pronounced at higher frequencies closer to the soft phonon mode. This can be observed in the insets of Figure 7.11b, c and d(the part inside the dashed box). The phenomenon is more evident at lower temperatures with more evident influence also at second and third harmonics of the spectrum.

For better understanding, the integral of terahertz transmission for each harmonics is plotted as a function of terahertz intensities in Figure 7.12a. The integral is calculated for the areas that are shaded with the corresponding legends. The integrated transmission

is normalized with respect to the one of lowest electric field for each harmonics. The sample transmission at different THz electric fields shows a response similar to nonlinear absorption and this feature is enhanced at higher frequencies(m=3). To ensure that the observed frequency dependence does not originate from the cavity in which sample is embedded we tracked the integral of the transmitted terahertz field from an empty cavity across various frequency ranges(Figure A.1).

Figure 7.12b displays the dependence of this nonlinear response of the third harmonic(m=3) on the temperature of the sample. The data reveals that the nonlinearity increases by reducing the temperature of the sample. In conclusion, the sample transmission at different THz electric fields shows a frequency dependent nonlinear response which is more evident at low temperatures. In addition to this, the field dependent response moves towards lower frequencies at low temperatures.

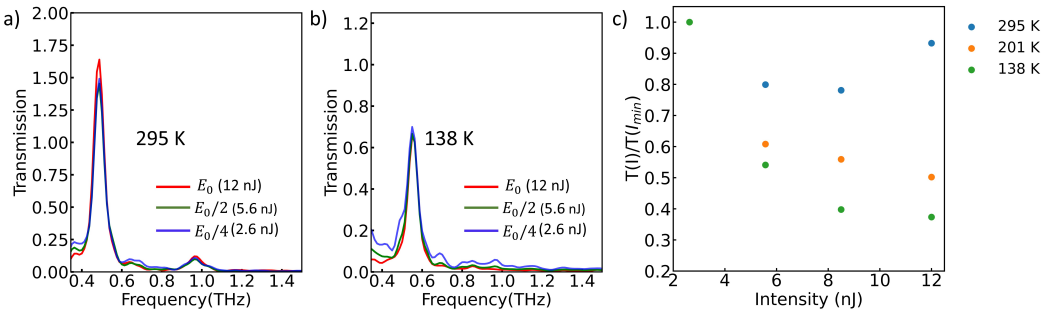

Fig. 7.13 **Nonlinear responses of STO inside shorter cavity (ω = 500 GHz).** THz transmission at different electric field strengths in 500 GHz cavity a) STO at T= 295 K b) STO at T= 138K. c) Integral of transmission at higher harmonics plotted as a function of THz intensity at different temperatures.

In order to confirm the nonlinear effect, the nonlinear feature was examined in shorter cavities with resonant frequency 500 GHz (cavity between sample and mirror). The transmission spectra at T=295 K and T=138 K are shown in Figure 7.13a and Figure 7.13b respectively. The sample shows a nonlinear response similar to the measurements in the longer cavity with an increase in the transmission of second harmonic for lower terahertz fields. The intensity dependence of the integrated terahertz transmission at ~ 1 THz is shown Figure 7.13c for different temperatures. The data shows that the spectral content near 1 THz is increasing by reducing the terahertz field strength. The dispersion in the transmission is also enhanced at low temperatures.

7.4.3 Discussion

The enhancement in the nonlinear responses at higher frequencies and lower temperatures can be possibly mapped to the soft phonon mode dynamics. Because, the nonlinear feature being evident also at lower frequencies by reducing the temperature of the sample can be attributed to the softening of the TO_1 mode in STO.

In our experiment, we are tuning the frequency of the soft phonon mode closer to the THz spectrum by reducing the temperature. This is shown in Figure 7.14a, b and c(T=295 K, 201 K and 138 K) by plotting the real part of the conductivity(red dashed line) for STO at

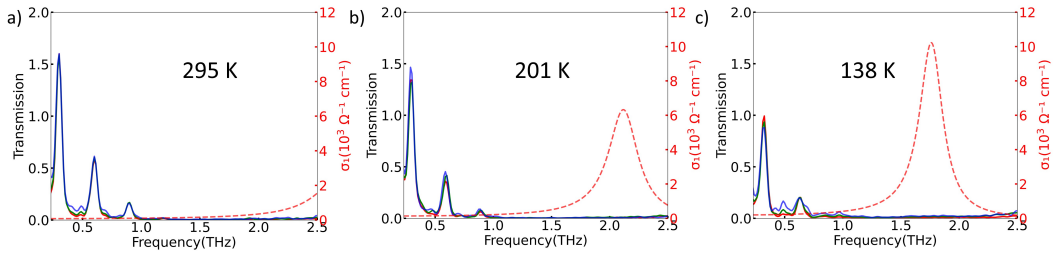

Fig. 7.14 **Soft Mode Evolution in Temperature.** The transmitted terahertz spectra of the hybrid cavity along with the real part of the STO terahertz conductivity(red dashed line) a) STO at T= 295 K b) STO at T= 201K c) STO at T= 138K

respective temperatures along with the transmitted terahertz spectra of the cavity. It can be seen that at low temperature, both the dielectric strength of the soft phonon mode and the overlap of the soft mode with the terahertz spectrum increases. This could possibly lead to the resonant excitation of soft mode to higher amplitudes by the electric field inside the cavity. The driving of the soft mode to larger displacements that are required to reach soft mode anharmonicity, leads to the decrease in the transmission at higher THz fields corresponding to the nonlinear response of the soft mode in this regime.

However, the soft mode anharmonicity has been attained only for terahertz fields above 50 kV/cm. [281, 249]. Moreover, we do not observe nonlinearities in the terahertz response of bulk STO measured outside the cavity. These findings suggest that the incoming terahertz field alone cannot fully explain the observed nonlinear effect.

We would like to put forward two possible scenarios in order to explain the THz field dependence inside the cavity. Firstly, there could be a cavity induced field enhancement of resonant frequencies at the sample position, thereby providing sufficient field strength at the resonant frequencies to drive the soft mode in to anharmonic regime. There are several publications in which they have reported a field enhancement for particular cavity geometries due to confinement of the photons[289]. More complex calculations have to be employed in our case since the material is highly dielectric and also because the incoming terahertz waves are pulsed with a repetition rate (50 KHz) that is negligible compared to the frequency of the terahertz cavity. The preliminary calculations to understand the field enhancement inside the cavity in our experimental settings are shown in Appendix B. Alternatively, the anharmonic soft mode potential has to be modified by the vacuum fluctuations inside the cavity facilitating the emergence of nonlinearity even at lower THz field strengths.

7.5 Conclusions

In conclusion, firstly we have studied the terahertz response of the soft mode of bulk STO reporting temperature evolution of the optical properties. The extracted static dielectric constant and soft mode frequency obey Curie Weiss law of ferroelectricity with a transition temperature of ~ 64 K.

The terahertz responses of the $SrTiO_3$ (STO) perovskite crystal has been studied inside the cavity to understand the influence of cavity electromagnetic environment on the sample. Specifically, we have conducted the terahertz field dependent studies on bulk STO in free space and inside the optical cavity. Contrary to measurements done in free space the transmission results inside the cavity exhibits a THz field dependence similar to nonlinear absorption. The effect has been more pronounced at higher frequencies and lower temperatures implying that the nonlinearity can be associated to the anharmonic soft phonon mode. Since the field is not enough to achieve anharmonic regime of STO the incoming terahertz field alone cannot fully explain the observed nonlinear response. So the effect can be explained only by cavity induced field enhancement of resonant frequencies at the sample position or the modification of anharmonic soft mode potential by the vacuum fluctuations inside the cavity facilitating the emergence of nonlinearity even at lower field strengths.

However, our findings suggest the possibility of driving the soft mode to anharmonic regime inside the cavity at much lower electric field strengths. The soft mode can be possibly driven in to higher amplitudes with the terahertz field if we go resonant to the soft mode. This can be achieved by using thinner STO samples, so that we reduce transmission loss from the soft mode. Our results also suggest that terahertz field induced ferroelectricity reported in STO [132] could be feasible without high intense terahertz pulses when the sample is embedded inside an optical cavity.

8

CONCLUSIONS

The aim of this doctoral thesis is to understand how the properties of the quantum materials are altered in a cavity electromagnetic environement. The experiments have provided insights into the properties and phases that emerge when these complex quantum materials are strongly coupled to confined electromagnetic fields.

The experimental demonstration of strong light-matter interaction in materials embedded inside the cavity has been achieved by implementing a tunable cryogenic cavity and terahertz spectrometers to characterize the light-matter hybrids. The terahertz cavity, developed in the laboratory, has proven to be efficient in tuning the fundamental cavity frequency in the terahertz range even at cryogenic temperatures. This capability enables the targeting of different low-energy excitations and facilitates the study of how their coupling with the cavity field may affect the material's macroscopic properties.

The efficiency of the setup was tested by coupling the fundamental mode of the cavity to the infrared(IR) active phonon mode in the $CuGeO_3$ sample. When the sample was embedded inside a resonant cavity, the transmission spectra revealed splitting, indicating the formation of light-matter hybrid states known as polaritons. The observed anti-crossing behavior in the polariton dispersion suggests that the system lies in the strong coupling regime. The temperature evolution of the Rabi splitting showed a larger splitting at higher temperatures, consistent with the temperature dependence of the phonon lifetime

In addition, we demonstrated signatures of multimode vibrational coupling in the dielectric phase of the charge density wave(CDW) material 1T-TaS_2. Polaritonic wave functions revealed that the multimode polaritons are formed through the simultaneous hybridization of multiple CDW phonon modes with the cavity's fundamental mode. The highly dispersive behavior of the upper and lower polaritons was attributed to the larger cavity components, while the cavity-mediated mixing of two non-degenerate phonons resulted in the less dispersive nature of the middle polaritons. Across the insulator-to-metal transition, we observed that the Rabi splitting gradually closes due to the onset of metallicity, reaching the weak-coupling limit near the phase transition temperature.

One of the key findings of the thesis was the ability to control the metal-insulator phase transition temperature in 1T-TaS_2 by tuning the cavity frequency and mirror alignment. By tuning the cavity frequency from 11.5 GHz to 570 GHz, an increase of 75 K has been reported

in the effective critical temperature of the sample. Since the change in effective critical temperature overcomes the free space hysteresis, we have demonstrated reversible cavity control of phase transition in 1T-TaS_2 at a fixed temperature. We proposed two theoretical scenarios to explain the cavity-mediated origin of the observed effects. The first scenario is based on the cavity-induced renormalization of the free energies of the metallic phase. The second scenario explores the possibility of modification in the effective sample temperature due to a Purcell-based mechanism. However, experimental evidence measuring the actual temperature of the sample, alongside the cold finger temperature, indicated that the effect is predominantly driven by the modification of the effective sample temperature through the filtering of the blackbody radiation mediated by the cavity.

Finally, we conducted temperature dependent terahertz transmission measurements on a paraelectric $SrTiO_3$(STO) crystal inside the cavity. Firstly, the temperature evolution of the terahertz responses of bulk STO revealed a mode softening with Curie's phase transition temperature at ~ 64 K. The terahertz field-dependent studies on the STO inside the cavity exhibited a nonlinear absorption-like feature, which was more pronounced at lower temperatures and near the soft mode frequency. This suggests that the nonlinearity is associated with the anharmonic soft phonon mode. However, the incoming terahertz electric field strength alone is insufficient to induce this nonlinear response in the material. Therefore, this nonlinearity must be attributed either to cavity-induced field enhancement of resonant frequencies at the sample position or to the modification of the anharmonic soft mode potential by vacuum fluctuations inside the cavity, facilitating the emergence of nonlinearity even at lower field strengths.

In summary, our findings highlight that the optical cavities are an efficient tool to engineer and control the phase transitions and non-linearities in quantum materials. Our work demonstrates that the cavity electrodynamics offers versatile platform to control light-matter interactions and hence the material properties in a wide range of complex quantum materials.

A

FIELD DEPENDENCE OF THE CAVITY

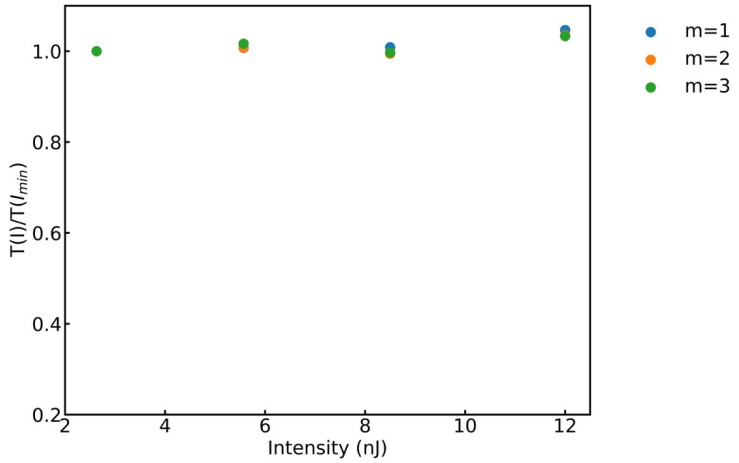

Fig. A.1 **Field Dependence of Empty Cavity.** a) Integral of the transmitted field in frequency domain (normalized by Malus's lawEquation 4.11) from an empty cavity at 138 K (Figure 4.15b) at different frequency ranges(same as the Figure 7.12a). The integral is calculated for the areas that are shaded with the corresponding legends in Figure 7.12a). The transmission at each frequency is normalized by the integral of lowest electric field.

B

CAVITY FIELD SIMULATIONS

B.1 Amplification of a Plane Wave inside Optical Cavity

The field entering the cavity through the first mirror undergoes multiple reflections before decaying completely. These reflections contribute to the field inside the cavity when they interfere constructively. Figure B.1 shows a plane wave incident on the first mirror(M_1) of the cavity reflecting multiple times inside the cavity. In each reflection, a fraction of the field is transmitted($t_{1,2}$) through the mirrors.

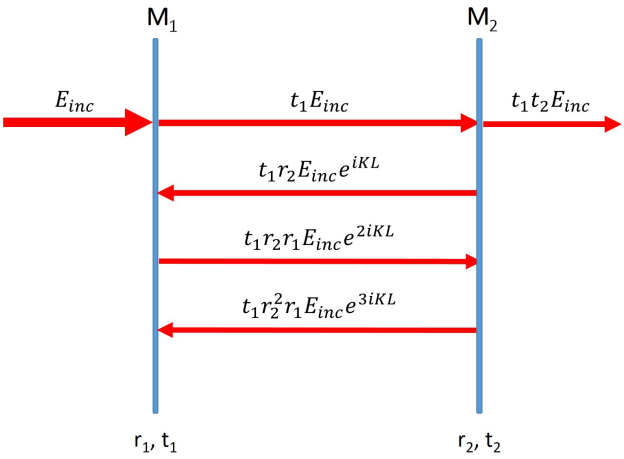

Fig. B.1 **Interferences inside an Optical Cavity.** a) Multiples reflections inside an optical cavity of length L. M_1 and M_2 are the cavity mirrors with reflectivity, $r_{1,2}$ and transmittivity, $t_{1,2}$. E_{inc} is the incident field.

The plane wave incident on the input mirror of the cavity can be written as,

$$E_{inc}(z,t) = E_{inc}e^{i(kz-\omega t)} \tag{B.1}$$

Considering that the input(output) mirror has a transmittivity,$t_1(t_2)$ and reflectivity, $r_1(r_2)$, the field entering the cavity can be written in terms of the transmission as,

$$E_{inc}(z,t) = E_{inc}t_1e^{i(kz-\omega t)} \tag{B.2}$$

where, z refers to the propagation inside the cavity. Considering that number of reflections contributing to the total field inside the cavity to be infinitely large, the total field inside a cavity of length L can be written by using an infinite geometric series in terms of reflectivity

and transmittivity of the mirrors.

$$\begin{aligned} E_{cav}(z,t) &= E_{inc}t_1 e^{i(kz-\omega t)} - E_{inc}t_1 r_2 e^{-i(kz+\omega t)} e^{2ikL} \\ &\quad + E_{inc}t_1 r_2^2 e^{2ikL} e^{i(kz-\omega t)} - E_{inc}t_1 r_1 r_2 e^{-i(kz+\omega t)} e^{4ikL} + \cdots \\ &= E_{inc}t_1 e^{i(kz-\omega t)} \left(1 + r_2^2 e^{2ikL} + r_2^4 e^{4ikL} + \cdots\right) \\ &\quad - E_{inc}t_1 r_2 e^{-i(kz+\omega t)} \left(1 + r_1 r_2 e^{2ikL} + r_1^2 r_2^2 e^{4ikL} + \cdots\right) \\ &= E_{inc}t_1 \left(\frac{e^{i(kz-\omega t)} - r_2 e^{2ikL} e^{-i(kz+\omega t)}}{1 - r_1 r_2 e^{2ikL}}\right) \end{aligned} \tag{B.3}$$

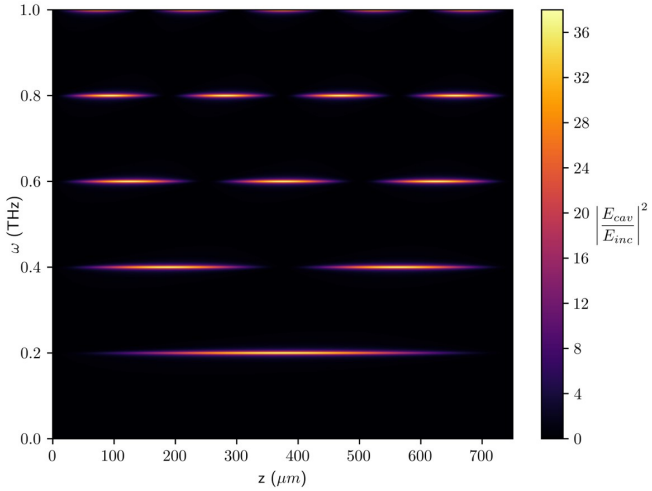

Fig. B.2 **Field Enhancement inside an Optical Cavity.** a) The intensity of the field inside the cavity with respect to the incident intensity obtained using Equation B.3. $r_1 = r_2 = 0.9$, L = 750μm (0.2 THz)

Figure B.2 presents the enhancement of the incident field(Equation B.3) along the cavity as a function of frequency for a cavity length L=750 μm(ω_c= 0.2 THz). It can be seen that the field inside the cavity is highly modulated spatially resulting in standing waves. The frequencies inside the cavity is constrained according to the boundary conditions and the field is largely enhanced at the harmonics of the cavity.

The calculations show that the intensity of the harmonics of the cavity is much higher (~ 30) than the incident field at the center of the cavity where the sample is placed. This amplification will be sufficient to explain the nonlinear response we observed for an STO inside the cavity(section 7.4). However, our experiments have been done using terahertz pulses with a repetition frequency, 50 KHz and the interference between the terahertz pulses would be negligible. So, this approach cannot be employed in our case to calculate the field.

B.2 Terahertz Pulse Propagation inside the Cavity

In order to understand field inside the cavity from a single terahertz pulse we simulated the propagation of a Gaussian pulse inside the cavity using COMSOL software(The Electromagnetic Waves, Transient User Interface).

We simulated the propagation of a single Gaussian pulse of the form,

$$E_{inc}(z,t) = E_0 e^{(-t^2/\tau^2)} \cos(\omega_0 t - kz) \tag{B.4}$$

with FWHM= 0.5 ps and ω_0=1.5 THz. The time domain pulse and the FFT in vacuum is shown in Figure B.3a and b respectively.

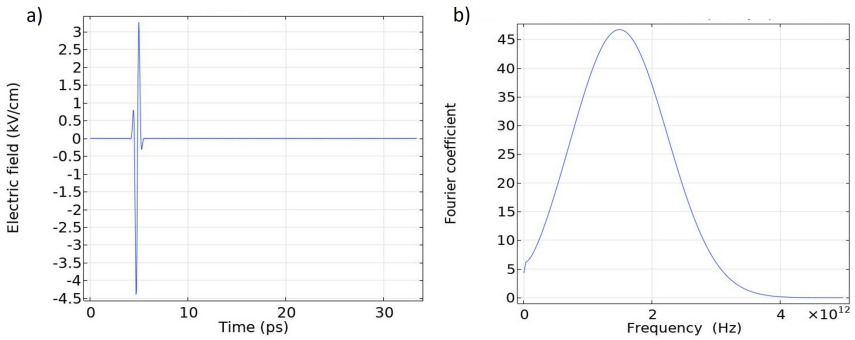

Fig. B.3 **Incident Field in Vacuum.** a) Gaussian pulse in vacuum and b) corresponding FFT. (FWHM=0.5 ps, ω_0= 1.5 THz)

To undestand the amplifcation of the field at the sample position, field at the center of a cavity of length, L_c=500 μm(ω_c=0.3 THz) has been simulated using the software for the pulse in Figure B.3. Thickness of the gold on the cavity mirrors was set at 10 nm.

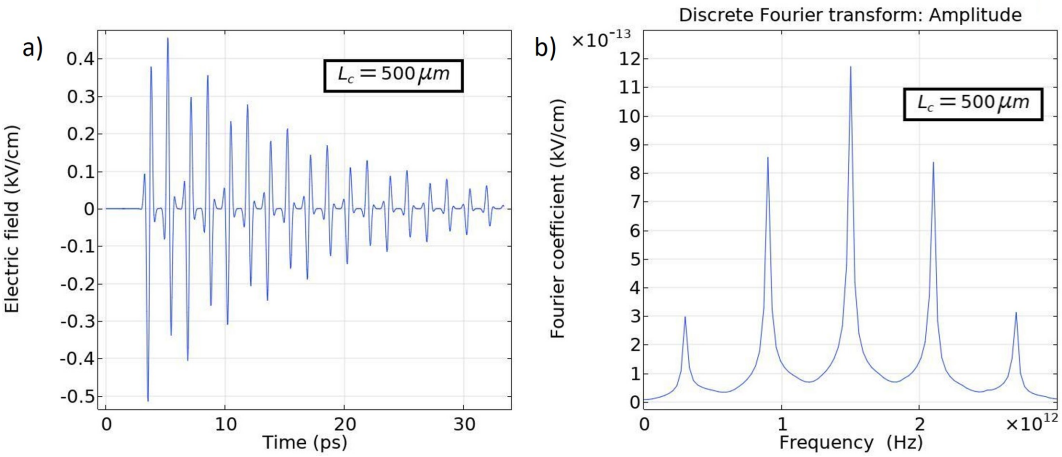

Fig. B.4 **Pulse Propagation inside an Empty Cavity.** a) Field at the middle of the cavity as function of time and b) corresponding discrete FFT. (L_c= 500μm,ω_c=0.3 THz)

Figure B.4a shows the field at the center of the cavity as a function of time. It can be seen that the field amplitude has reduced significantly inside the cavity with respect to the incoming field due to the transmission loss of the input mirror. The peaks in the FFT(Figure B.4b) is associated to the odd harmonics of the cavity and the even harmonics cannot be seen in the spectrum since there is a node at the middle of the cavity.

The field amplitude on the STO crystal inside the cavity can be obtained by simulating the field at the first surface of the sample(no transmission loss from the sample). Figure B.5a presents the simulated field at the first surface of an STO sample of thickness 100 μm at 138 K embedded inside an optical cavity. The distance between the sample and the mirrors were set at 500 μm.

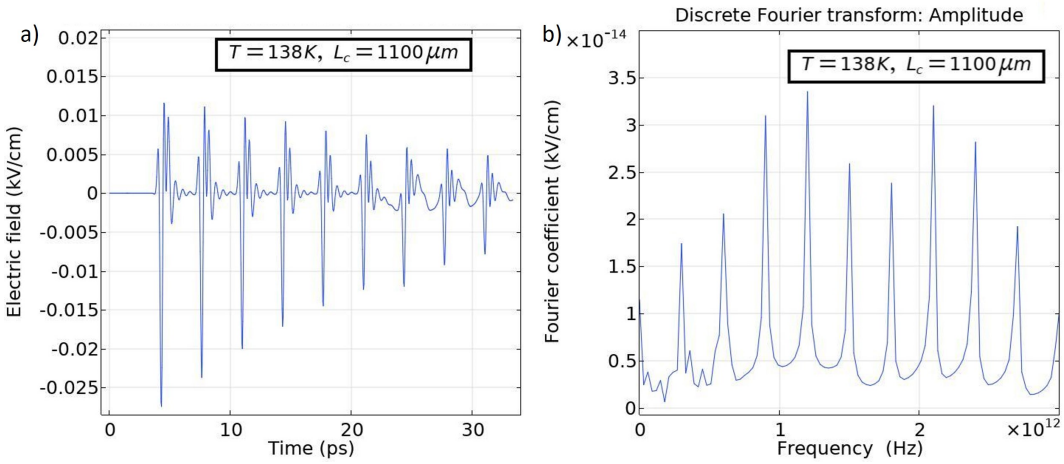

Fig. B.5 **Incident Field on STO Crystal.** a) Field at the surface of the STO crystal as a function of time and b) corresponding discrete FFT. (temperature= 138 K, thickness of the sample= 100 μm,)

Even though there is no transmission loss apart from the one of the input mirror on the surface of the STO, the field is significantly reduced because the sample and the input mirror form a cavity that has a node at the surface of the sample. However, the FFT(Figure B.5b) shows the peaks of the harmonics because the cavity does not have a perfect boundary.

From the COMSOL simulations, we couldn't obtain a field amplification at the sample position due to the pulsed nature of the laser. Hence, a future approach would be to assume in the simulations that the STO crystal is nonlinear. So that, the field confinement enhances the non linearity resulting in enhanced nonlinear responses inside the cavity.

BIBLIOGRAPHY

[1] Albert Einstein. über einen die Erzeugung und Verwandlung des lichtes betreffenden heuristischen Gesichtspunkt, 1905.

[2] Richard Phillips Feynman. QED: The strange theory of light and matter. 2006.

[3] WE Lamb and RC Retherford. LAMB 1947. *Phys. Rev*, 72:241, 1947.

[4] Peter Schwerdtfeger. Relativistic electronic structure theory: Part 2. applications. 2004.

[5] Edward M Purcell, Henry Cutler Torrey, and Robert V Pound. Resonance absorption by nuclear magnetic moments in a solid. *Physical review*, 69(1-2):37, 1946.

[6] Ph Goy, JM Raimond, M Gross, and S Haroche. Observation of cavity-enhanced single-atom spontaneous emission. *Physical review letters*, 50(24):1903, 1983.

[7] Randall G Hulet, Eric S Hilfer, and Daniel Kleppner. Inhibited spontaneous emission by a Rydberg atom. *Physical review letters*, 55(20):2137, 1985.

[8] Gerhard Rempe, Herbert Walther, and Norbert Klein. Observation of quantum collapse and revival in a one-atom maser. *Physical review letters*, 58(4):353, 1987.

[9] RJ Thompson, Gerhard Rempe, and HJ Kimble. Observation of normal-mode splitting for an atom in an optical cavity. *Physical review letters*, 68(8):1132, 1992.

[10] A Boca, R Miller, KM Birnbaum, AD Boozer, J McKeever, and HJ Kimble. Observation of the vacuum Rabi spectrum for one trapped atom. *Physical review letters*, 93(23): 233603, 2004.

[11] MG Raizen, RJ Thompson, RJ Brecha, HJ Kimble, and HJ Carmichael. Normal-mode splitting and linewidth averaging for two-state atoms in an optical cavity. *Physical review letters*, 63(3):240, 1989.

[12] Peter Maunz, Thomas Puppe, Ingrid Schuster, Niels Syassen, Pepijn WH Pinkse, and Gerhard Rempe. Normal-mode spectroscopy of a single-bound-atom–cavity system. *Physical review letters*, 94(3):033002, 2005.

[13] Gessler Hernandez, Jiepeng Zhang, and Yifu Zhu. Vacuum Rabi splitting and intracavity dark state in a cavity-atom system. *Physical Review A*, 76(5):053814, 2007.

[14] DI Schuster, Lev S Bishop, IL Chuang, D DeMille, and RJ Schoelkopf. Cavity QED in a molecular ion trap. *Physical Review A*, 83(1):012311, 2011.

[15] Anton Frisk Kockum, Adam Miranowicz, Simone De Liberato, Salvatore Savasta, and Franco Nori. Ultrastrong coupling between light and matter. *Nature Reviews Physics*, 1 (1):19–40, 2019.

[16] Thomas W Ebbesen. Hybrid light–matter states in a molecular and material science perspective. *Accounts of chemical research*, 49(11):2403–2412, 2016.

[17] Vladimir M Agranovich, M Litinskaia, and David G Lidzey. Cavity polaritons in microcavities containing disordered organic semiconductors. *Physical Review B*, 67(8): 085311, 2003.

[18] Galina Khitrova, HM Gibbs, M Kira, Stephan W Koch, and Axel Scherer. Vacuum rabi splitting in semiconductors. *Nature physics*, 2(2):81–90, 2006.

[19] Claude Weisbuch, Mr Nishioka, A Ishikawa, and Y Arakawa. Observation of the coupled exciton-photon mode splitting in a semiconductor quantum microcavity. *Physical review letters*, 69(23):3314, 1992.

[20] David J Shelton, Igal Brener, James C Ginn, Michael B Sinclair, David W Peters, Kevin R Coffey, and Glenn D Boreman. Strong coupling between nanoscale metamaterials and phonons. *Nano letters*, 11(5):2104–2108, 2011.

[21] Xin Jin, Andrea Cerea, Gabriele C Messina, Andrea Rovere, Riccardo Piccoli, Francesco De Donato, Francisco Palazon, Andrea Perucchi, Paola Di Pietro, Roberto Morandotti, et al. Reshaping the phonon energy landscape of nanocrystals inside a terahertz plasmonic nanocavity. *Nature communications*, 9(1):763, 2018.

[22] Ran Damari, Omri Weinberg, Daniel Krotkov, Natalia Demina, Katherine Akulov, Adina Golombek, Tal Schwartz, and Sharly Fleischer. Strong coupling of collective intermolecular vibrations in organic materials at terahertz frequencies. *Nature Communications*, 10(1):3248, 2019.

[23] Isaac John Luxmoore, Choon How Gan, Peter Qiang Liu, Federico Valmorra, Penglei Li, Jérôme Faist, and Geoffrey R Nash. Strong coupling in the far-infrared between graphene plasmons and the surface optical phonons of silicon dioxide. *ACS photonics*, 1(11):1151–1155, 2014.

[24] Robrecht MA Vergauwe, Jino George, Thibault Chervy, James A Hutchison, Atef Shalabney, Vladimir Y Torbeev, and Thomas W Ebbesen. Quantum strong coupling with protein vibrational modes. *The journal of physical chemistry letters*, 7(20):4159–4164, 2016.

[25] Jino George, Atef Shalabney, James A Hutchison, Cyriaque Genet, and Thomas W Ebbesen. Liquid-phase vibrational strong coupling. *The journal of physical chemistry letters*, 6(6):1027–1031, 2015.

[26] Javier del Pino, Johannes Feist, and Francisco J Garcia-Vidal. Quantum theory of collective strong coupling of molecular vibrations with a microcavity mode. *New Journal of Physics*, 17(5):053040, 2015.

[27] Giacomo Jarc, Shahla Yasmin Mathengattil, Francesca Giusti, Maurizio Barnaba, Abhishek Singh, Angela Montanaro, Filippo Glerean, Enrico Maria Rigoni, Simone Dal Zilio, Stephan Winnerl, et al. Tunable cryogenic terahertz cavity for strong light–matter coupling in complex materials. *Review of Scientific Instruments*, 93(3), 2022.

[28] Prasahnt Sivarajah, Andreas Steinbacher, Blake Dastrup, Jian Lu, Maolin Xiang, Wei Ren, Stanislav Kamba, Shixun Cao, and Keith A Nelson. THz-frequency magnon-phonon-polaritons in the collective strong-coupling regime. *Journal of Applied Physics*, 125(21), 2019.

[29] Frank Schlawin, Andrea Cavalleri, and Dieter Jaksch. Cavity-mediated electron-photon superconductivity. *Physical review letters*, 122(13):133602, 2019.

[30] Jonathan B Curtis, Zachary M Raines, Andrew A Allocca, Mohammad Hafezi, and Victor M Galitski. Cavity quantum Eliashberg enhancement of superconductivity. *Physical review letters*, 122(16):167002, 2019.

[31] Michael A Sentef, Michael Ruggenthaler, and Angel Rubio. Cavity quantum-electrodynamical polaritonically enhanced electron-phonon coupling and its influence on superconductivity. *Science advances*, 4(11):eaau6969, 2018.

[32] Andrew A Allocca, Zachary M Raines, Jonathan B Curtis, and Victor M Galitski. Cavity superconductor-polaritons. *Physical Review B*, 99(2):020504, 2019.

[33] Yannis Laplace, Stephanie Fernandez-Pena, Stefano Gariglio, Jean-Marc Triscone, and Andrea Cavalleri. Proposed cavity Josephson plasmonics with complex-oxide heterostructures. *Physical Review B*, 93(7):075152, 2016.

[34] Hongmin Gao, Frank Schlawin, Michele Buzzi, Andrea Cavalleri, and Dieter Jaksch. Photoinduced electron pairing in a driven cavity. *Physical Review Letters*, 125(5):053602, 2020.

[35] Jiajun Li and Martin Eckstein. Manipulating intertwined orders in solids with quantum light. *Physical Review Letters*, 125(21):217402, 2020.

[36] Simone Latini, Enrico Ronca, Umberto De Giovannini, Hannes Hübener, and Angel Rubio. Cavity control of excitons in two-dimensional materials. *Nano letters*, 19(6): 3473–3479, 2019.

[37] Yuto Ashida, Ataç İmamoğlu, Jérôme Faist, Dieter Jaksch, Andrea Cavalleri, and Eugene Demler. Quantum electrodynamic control of matter: Cavity-enhanced ferroelectric phase transition. *Physical Review X*, 10(4):041027, 2020.

[38] Simone Latini, Dongbin Shin, Shunsuke A Sato, Christian Schäfer, Umberto De Giovannini, Hannes Hübener, and Angel Rubio. The ferroelectric photo ground state of $SrTiO_3$: Cavity materials engineering. *Proceedings of the National Academy of Sciences*, 118(31):e2105618118, 2021.

[39] Jonathan B Curtis, Marios H Michael, and Eugene Demler. Local fluctuations in cavity control of ferroelectricity. *Physical Review Research*, 5(4):043118, 2023.

[40] Katharina Lenk, Jiajun Li, Philipp Werner, and Martin Eckstein. Dynamical mean-field study of a photon-mediated ferroelectric phase transition. *Physical Review B*, 106(24): 245124, 2022.

[41] Öney O Soykal and ME Flatté. Strong field interactions between a nanomagnet and a photonic cavity. *Physical review letters*, 104(7):077202, 2010.

[42] Gian L Paravicini-Bagliani, Felice Appugliese, Eli Richter, Federico Valmorra, Janine Keller, Mattias Beck, Nicola Bartolo, Clemens Rössler, Thomas Ihn, Klaus Ensslin, et al. Magneto-transport controlled by Landau polariton states. *Nature Physics*, 15(2): 186–190, 2019.

[43] Felice Appugliese, Josefine Enkner, Gian Lorenzo Paravicini-Bagliani, Mattias Beck, Christian Reichl, Werner Wegscheider, Giacomo Scalari, Cristiano Ciuti, and Jérôme Faist. Breakdown of topological protection by cavity vacuum fields in the integer quantum hall effect. *Science*, 375(6584):1030–1034, 2022.

[44] Anoop Thomas, Eloïse Devaux, Kalaivanan Nagarajan, Thibault Chervy, Marcus Seidel, David Hagenmüller, Stefan Schütz, Johannes Schachenmayer, Cyriaque Genet, Guido Pupillo, et al. Exploring superconductivity under strong coupling with the vacuum electromagnetic field. *arXiv preprint arXiv:1911.01459*, 2019.

[45] Anoop Thomas, Eloise Devaux, Kalaivanan Nagarajan, Guillaume Rogez, Marcus Seidel, Fanny Richard, Cyriaque Genet, Marc Drillon, and Thomas W Ebbesen. Large enhancement of ferromagnetism under a collective strong coupling of YBCO nanoparticles. *Nano letters*, 21(10):4365–4370, 2021.

[46] H Mabuchi and AC Doherty. Cavity quantum electrodynamics: coherence in context. *Science*, 298(5597):1372–1377, 2002.

[47] Serge Haroche. A short history of cavity quantum electrodynamics. page CTuF2. Optica Publishing Group, 2007.

[48] Kerry J Vahala. Optical microcavities. *nature*, 424(6950):839–846, 2003.

[49] Manuel Hertzog, Mao Wang, Jürgen Mony, and Karl Börjesson. Strong light–matter interactions: a new direction within chemistry. *Chemical Society Reviews*, 48(3):937–961, 2019.

[50] Andri M Gretarsson. A first course in laboratory optics. 2021.

[51] M Vaughan. The Fabry-Perot interferometer: history, theory, practice and applications. 2017.

[52] Garrett D Cole, Wei Zhang, Michael J Martin, Jun Ye, and Markus Aspelmeyer. Tenfold reduction of brownian noise in high-reflectivity optical coatings. *Nature Photonics*, 7 (8):644–650, 2013.

[53] DW Vernooy, Vladimir S Ilchenko, H Mabuchi, EW Streed, and HJ Kimble. High-q measurements of fused-silica microspheres in the near infrared. *Optics letters*, 23(4): 247–249, 1998.

[54] Valérie Lefèvre-Seguin and Serge Haroche. Towards cavity-qed experiments with silica microspheres. *Materials Science and Engineering: B*, 48(1-2):53–58, 1997.

[55] Serge Haroche and Daniel Kleppner. Cavity Quantum Electrodynamics: A new generation of experiments shows that spontaneous radiation from excited atoms can be greatly suppressed or enhanced by placing the atoms between mirrors or in cavities. pages 849–855. Springer, 1995.

[56] Edward Mills Purcell. Spontaneous emission probabilities at radio frequencies. pages 839–839. Springer, 1995.

[57] Claude Cohen-Tannoudji, Jacques Dupont-Roc, and Gilbert Grynberg. Photons and atoms-introduction to quantum electrodynamics. 1997.

[58] Manuel Hertzog, Per Rudquist, James A Hutchison, Jino George, Thomas W Ebbesen, and Karl Börjesson. Voltage-controlled switching of strong light–matter interactions using liquid crystals. *Chemistry–A European Journal*, 23(72):18166–18170, 2017.

[59] Weilu Gao, Xinwei Li, Motoaki Bamba, and Junichiro Kono. Continuous transition between weak and ultrastrong coupling through exceptional points in carbon nanotube microcavity exciton–polaritons. *Nature Photonics*, 12(6):362–367, 2018.

[60] DJ Heinzen, JJ Childs, JE Thomas, and MS Feld. Enhanced and inhibited visible spontaneous emission by atoms in a confocal resonator. *Physical review letters*, 58(13): 1320, 1987.

[61] Wen-Hao Chang, Wen-Yen Chen, Hsiang-Szu Chang, Tung-Po Hsieh, Jen-Inn Chyi, and Tzu-Min Hsu. Efficient single-photon sources based on low-density quantum dots in photonic-crystal nanocavities. *Physical review letters*, 96(11):117401, 2006.

[62] Rodney Loudon. The quantum theory of light. 2000.

[63] Lukas Novotny. Strong coupling, energy splitting, and level crossings: A classical perspective. *American Journal of Physics*, 78(11):1199–1202, 2010.

[64] VA Yakovlev, VG Nazin, and GN Zhizhin. The surface polariton splitting due to thin surface film LO vibrations. *Optics Communications*, 15(2):293–295, 1975.

[65] Edwin T Jaynes and Frederick W Cummings. Comparison of quantum and semiclassical radiation theories with application to the beam maser. *Proceedings of the IEEE*, 51 (1):89–109, 1963.

[66] Said Rahimzadeh-Kalaleh Rodriguez. Classical and quantum distinctions between weak and strong coupling. *European Journal of Physics*, 37(2):025802, 2016.

[67] Michael Tavis and Frederick W Cummings. Exact solution for an n-molecule—radiation-field hamiltonian. *Physical Review*, 170(2):379, 1968.

[68] Barry M Garraway. The dicke model in quantum optics: Dicke model revisited. *Philosophical Transactions of the Royal Society A: Mathematical, Physical and Engineering Sciences*, 369(1939):1137–1155, 2011.

[69] Theodore Holstein and Henry Primakoff. Field dependence of the intrinsic domain magnetization of a ferromagnet. *Physical Review*, 58(12):1098, 1940.

[70] JJ Hopfield. Theory of the contribution of excitons to the complex dielectric constant of crystals. *Physical Review*, 112(5):1555, 1958.

[71] VM Agranovich, Yu N Gartstein, and M Litinskaya. Hybrid resonant organic–inorganic nanostructures for optoelectronic applications. *Chemical reviews*, 111(9): 5179–5214, 2011.

[72] R Houdré, RP Stanley, and M Ilegems. Vacuum-field rabi splitting in the presence of inhomogeneous broadening: Resolution of a homogeneous linewidth in an inhomogeneously broadened system. *Physical Review A*, 53(4):2711, 1996.

[73] Perry R Rice and Robert J Brecha. Cavity induced transparency. *Optics communications*, 126(4-6):230–235, 1996.

[74] Haruka Tanji-Suzuki, Wenlan Chen, Renate Landig, Jonathan Simon, and Vladan Vuletić. Vacuum-induced transparency. *Science*, 333(6047):1266–1269, 2011.

[75] Andrey E Miroshnichenko, Sergej Flach, and Yuri S Kivshar. Fano resonances in nanoscale structures. *Reviews of Modern Physics*, 82(3):2257, 2010.

[76] Boris Luk'Yanchuk, Nikolay I Zheludev, Stefan A Maier, Naomi J Halas, Peter Nordlander, Harald Giessen, and Chong Tow Chong. The fano resonance in plasmonic nanostructures and metamaterials. *Nature materials*, 9(9):707–715, 2010.

[77] Naomi J Halas, Surbhi Lal, Wei-Shun Chang, Stephan Link, and Peter Nordlander. Plasmons in strongly coupled metallic nanostructures. *Chemical reviews*, 111(6):3913–3961, 2011.

[78] Robert H Dicke. Coherence in spontaneous radiation processes. *Physical review*, 93(1): 99, 1954.

[79] II Rabi. On the process of space quantization. *Physical Review*, 49(4):324, 1936.

[80] MS Skolnick, TA Fisher, and DM Whittaker. Strong coupling phenomena in quantum microcavity structures. *Semiconductor Science and Technology*, 13(7):645, 1998.

[81] Malcolm E Lines and Alastair M Glass. Principles and applications of ferroelectrics and related materials. 2001.

[82] Joseph Valasek. Piezo-electric and allied phenomena in rochelle salt. *Physical review*, 17(4):475, 1921.

[83] Dragan Damjanovic. Ferroelectric, dielectric and piezoelectric properties of ferroelectric thin films and ceramics. *Reports on progress in physics*, 61(9):1267, 1998.

[84] Sergey I Shkuratov and Christopher S Lynch. A review of ferroelectric materials for high power devices. *Journal of Materiomics*, 8(4):739–752, 2022.

[85] PC Lysne and CM Percival. Electric energy generation by shock compression of ferroelectric ceramics: Normal- mode response of PZT 95/5. *Journal of Applied Physics*, 46(4):1519–1525, 1975.

[86] Robert E Setchell. Shock wave compression of the ferroelectric ceramic Pb0. 99 (Zr0. 95Ti0. 05) 0.98 Nb0. 02O3: depoling currents. *Journal of applied physics*, 97(1), 2005.

[87] Sergey I Shkuratov, Jason Baird, Vladimir G Antipov, Evgueni F Talantsev, Hwan R Jo, Juan C Valadez, and Christopher S Lynch. Depolarization mechanisms of PbZr0. 52Ti0. 48O3 and PbZr0. 95Ti0. 05O3 poled ferroelectrics under high strain rate loading. *Applied Physics Letters*, 104(21), 2014.

[88] Ping Peng, Hengchang Nie, Genshui Wang, Zhen Liu, Fei Cao, and Xianlin Dong. Shock-driven depolarization behavior in bnt-based lead-free ceramics. *Applied Physics Letters*, 113(8), 2018.

[89] Zhipeng Gao, Wei Peng, Bin Chen, Simon AT Redfern, Ke Wang, Baojin Chu, Qiang He, Yi Sun, Xuefeng Chen, Hengchang Nie, et al. Giant power output in lead-free ferroelectrics by shock-induced phase transition. *Physical Review Materials*, 3(3):035401, 2019.

[90] Lei Zhao, Qing Liu, Jing Gao, Shujun Zhang, and Jing-Feng Li. Lead-free antiferroelectric silver niobate tantalate with high energy storage performance. *Advanced Materials*, 29(31):1701824, 2017.

[91] Seung-Eek Park and Thomas R Shrout. Characteristics of relaxor-based piezoelectric single crystals for ultrasonic transducers. *IEEE Transactions on Ultrasonics, Ferroelectrics, and Frequency Control*, 44(5):1140–1147, 1997.

[92] Anthony J Moulson and John M Herbert. Electroceramics: materials, properties, applications. 2003.

[93] Guangzu Zhang, Dingyang Zhu, Xiaoshan Zhang, Ling Zhang, Jinqiao Yi, Bing Xie, Yike Zeng, Qi Li, Qing Wang, and Shenglin Jiang. High-energy storage performance of (Pb0. 87Ba0. 1La0. 02)(Zr0. 68Sn0. 24Ti0. 08) O3 antiferroelectric ceramics fabricated by the hot-press sintering method. *Journal of the American Ceramic Society*, 98(4):1175–1181, 2015.

[94] Zhen Liu, Xuefeng Chen, Wei Peng, Chenhong Xu, Xianlin Dong, Fei Cao, and Genshui Wang. Temperature-dependent stability of energy storage properties of Pb0. 97La0. 02 (Zr0. 58Sn0. 335Ti0. 085) O3 antiferroelectric ceramics for pulse power capacitors. *Applied Physics Letters*, 106(26), 2015.

[95] Jinglei Li, Fei Li, Zhuo Xu, and Shujun Zhang. Multilayer lead-free ceramic capacitors with ultrahigh energy density and efficiency. *Advanced Materials*, 30(32):1802155, 2018.

[96] Ge Wang, Zhilun Lu, Yong Li, Linhao Li, Hongfen Ji, Antonio Feteira, Di Zhou, Dawei Wang, Shujun Zhang, and Ian M Reaney. Electroceramics for high-energy density capacitors: current status and future perspectives. *Chemical Reviews*, 121(10):6124–6172, 2021.

[97] George A Samara. Ferroelectricity revisited—advances in materials and physics. volume 56, pages 239–458. Elsevier, 2001.

[98] Vladimir Fridkin, Stephen Ducharme, Vladimir Fridkin, and Stephen Ducharme. Ferroelectricity and ferroelectric phase transition. *Ferroelectricity at the Nanoscale: Basics and Applications*, pages 1–9, 2014.

[99] Francesco Barantani. Phonons in a ferroelectric superconductor: optical spectroscopy on $Ca_xSr_{1-x}TiO_3 - d$. 2018.

[100] Lev Davidovich Landau and Evgenii Mikhailovich Lifshitz. Statistical physics: Volume 5. 5, 2013.

[101] Ronald E Cohen. Origin of ferroelectricity in perovskite oxides. *Nature*, 358(6382): 136–138, 1992.

[102] A Scalabrin, AS Chaves, DS Shim, and SPS Porto. Temperature dependence of the A1 and E optical phonons in $BaTiO_3$. *physica status solidi (b)*, 79(2):731–742, 1977.

[103] Y Luspin, JL Servoin, and F Gervais. Soft mode spectroscopy in barium titanate. *Journal of Physics C: Solid State Physics*, 13(19):3761, 1980.

[104] G Venkataraman. Soft modes and structural phase transitions. *Bulletin of Materials Science*, 1:129–170, 1979.

[105] GA Samara and PS Peercy. The study of soft-mode transitions at high pressure. *Solid State Physics*, 36:1–118, 1982.

[106] Ganesan Venkataraman, Lee A Feldkamp, and Vinod C Sahni. Dynamics of perfect crystals. *(No Title)*, 1975.

[107] Robert Blinc and B Zeks. Soft modes in Ferroelectrics and Antiferroelectrics. 1974.

[108] D Schmeltzer. Quantum ferroelectrics: A renormalization-group study. *Physical Review B*, 28(1):459, 1983.

[109] R Oppermann and H Thomas. Critical behaviour at the displacive limit of structural phase transitions. *Zeitschrift für Physik B Condensed Matter*, 22(4):387–396, 1975.

[110] UT Höchli and LA Boatner. Quantum ferroelectricity in $K_{1-x}Na_xTaO_3$ and $KTa_{1-y}Nb_yO_3$. *Physical Review B*, 20(1):266, 1979.

[111] K Alex Müller and H Burkard. $SrTiO_3$: An intrinsic quantum paraelectric below 4 k. *Physical Review B*, 19(7):3593, 1979.

[112] K Alex Müller. Quantum para-, ferro-, and random electric behaviors in oxide perovskites. *Japanese Journal of Applied Physics*, 24(S2):89, 1985.

[113] HARRISON H Barrett. Acoustic properties of materials of the perovskite structure. *Physical acoustics*, 6:65–108, 2012.

[114] W. R. Abel. *Physical Review B*, 4(3697), 1971.

[115] Grégory Geneste and Jean-Michel Kiat. Ground state of Ca-doped strontium titanate: Ferroelectricity versus polar nanoregions. *Physical Review B*, 77(17):174101, 2008.

[116] JG Bednorz and KA Müller. $Sr_{1-x}Ca_xTiO_3$: an xy quantum ferroelectric with transition to randomness. *Physical Review Letters*, 52(25):2289, 1984.

[117] YG Wang, W Kleemann, WL Zhong, and L Zhang. Impurity-induced phase transition in quantum paraelectrics. *Physical Review B*, 57(21):13343, 1998.

[118] M Itoh, R Wang, Y Inaguma, T Yamaguchi, YJ Shan, and T Nakamura. Ferroelectricity induced by oxygen isotope exchange in strontium titanate perovskite. *Physical Review Letters*, 82(17):3540, 1999.

[119] Mitsuru Itoh and Ruiping Wang. Quantum ferroelectricity in $SrTiO_3$ induced by oxygen isotope exchange. *Applied Physics Letters*, 76(2):221–223, 2000.

[120] Hai-Yao Deng, Chi-Hang Lam, and HT Huang. On the origin of oxygen isotope exchange induced ferroelectricity in strontium titanate. *The European Physical Journal B*, 85:1–6, 2012.

[121] Ruiping Wang and Mitsuru Itoh. Suppression of the quantum fluctuation in 18 O-enriched strontium titanate. *Physical Review B*, 64(17):174104, 2001.

[122] Yilin Wang, Hanqing Zhao, Linxing Zhang, Jun Chen, and Xianran Xing. $PbTiO_3$-based perovskite ferroelectric and multiferroic thin films. *Physical Chemistry Chemical Physics*, 19(27):17493–17515, 2017.

[123] I Ponomareva and L Bellaiche. Nature of dynamical coupling between polarization and strain in nanoscale ferroelectrics from first principles. *Physical review letters*, 101 (19):197602, 2008.

[124] Shan Li, Yilin Wang, Mingdi Yang, Jun Miao, Kun Lin, Qiang Li, Xin Chen, Jinxia Deng, and Xianran Xing. Ferroelectric thin films: performance modulation and application. *Materials Advances*, 3(14):5735–5752, 2022.

[125] JH Haeni, P Irvin, W Chang, Reinhard Uecker, P Reiche, YL Li, S Choudhury, Wei Tian, ME Hawley, B Craigo, et al. Room-temperature ferroelectricity in strained $SrTiO_3$. *Nature*, 430(7001):758–761, 2004.

[126] Wu Hua, Zhan Yage, and Zhang Rong. Soft mode behavior in strained $SrTiO_3$ thin film. pages 1–4. IEEE, 2011.

[127] WD Nix and BM Clemens. Crystallite coalescence: mechanism for intrinsic tensile stresses in thin films. *Journal of materials research*, 14(8):3467–3473, 1999.

[128] JS Speck, AC Daykin, A Seifert, AE Romanov, and W Pompe. Domain configurations due to multiple misfit relaxation mechanisms in epitaxial ferroelectric thin films. iii. interfacial defects and domain misorientations. *Journal of applied physics*, 78(3): 1696–1706, 1995.

[129] Sophie A Harrington, Junyi Zhai, Sava Denev, Venkatraman Gopalan, Haiyan Wang, Zhenxing Bi, Simon AT Redfern, Seung-Hyub Baek, Chung W Bark, Chang-Beom Eom, et al. Thick lead-free ferroelectric films with high Curie temperatures through nanocomposite-induced strain. *Nature nanotechnology*, 6(8):491–495, 2011.

[130] MD Biegalski, Y Jia, DG Schlom, S Trolier-McKinstry, SK Streiffer, V Sherman, R Uecker, and P Reiche. Relaxor ferroelectricity in strained epitaxial $SrTiO_3$ thin films on $DyScO_3$ substrates. *Applied physics letters*, 88(19), 2006.

[131] R Wördenweber, E Hollmann, R Kutzner, and J Schubert. Induced ferroelectricity in strained epitaxial $SrTiO_3$ films on various substrates. *Journal of applied physics*, 102(4), 2007.

[132] Xian Li, Tian Qiu, Jiahao Zhang, Edoardo Baldini, Jian Lu, Andrew M Rappe, and Keith A Nelson. Terahertz field–induced ferroelectricity in quantum paraelectric $SrTiO_3$. *Science*, 364(6445):1079–1082, 2019.

[133] Dongbin Shin, Simone Latini, C Schafer, Shunsuke A Sato, Edoardo Baldini, Umberto De Giovannini, H Hubener, and Angel Rubio. Simulating terahertz field-induced transient ferroeletricity in quantum paraelectric $SrTiO_3$. *arXiv preprint arXiv:2106.03957*, 2021.

[134] Giacomo Jarc, Shahla Yasmin Mathengattil, Angela Montanaro, Francesca Giusti, Enrico Maria Rigoni, Rudi Sergo, Francesca Fassioli, Stephan Winnerl, Simone Dal Zilio, Dragan Mihailovic, et al. Cavity-mediated thermal control of metal-to-insulator transition in $1T - TaS_2$. *Nature*, 622(7983):487–492, 2023.

[135] Peter Salén, Martina Basini, Stefano Bonetti, János Hebling, Mikhail Krasilnikov, Alexey Y Nikitin, Georgii Shamuilov, Zoltán Tibai, Vitali Zhaunerchyk, and Vitaliy Goryashko. Matter manipulation with extreme terahertz light: Progress in the enabling THz technology. *Physics reports*, 836:1–74, 2019.

[136] Masayoshi Tonouchi. Cutting-edge terahertz technology. *Nature photonics*, 1(2):97–105, 2007.

[137] Susan L Dexheimer. Terahertz spectroscopy: principles and applications. 2017.

[138] Xi-Cheng Zhang, Jingzhou Xu, et al. Introduction to THz wave photonics. 29, 2010.

[139] Nathan M Burford and Magda O El-Shenawee. Review of terahertz photoconductive antenna technology. *Optical Engineering*, 56(1):010901–010901, 2017.

[140] Yejun He, Yaling Chen, Long Zhang, Sai-Wai Wong, and Zhi Ning Chen. An overview of terahertz antennas. *China Communications*, 17(7):124–165, 2020.

[141] T Löffler, T Hahn, M Thomson, F Jacob, and HG Roskos. Large-area electro-optic ZnTe terahertz emitters. *Optics express*, 13(14):5353–5362, 2005.

[142] F Blanchard, Luca Razzari, H-C Bandulet, G Sharma, R Morandotti, J-C Kieffer, T Ozaki, M Reid, HF Tiedje, HK Haugen, et al. Generation of 1.5 μj single-cycle terahertz pulses by optical rectification from a large aperture ZnTe crystal. *Optics Express*, 15(20):13212–13220, 2007.

[143] Friederike Junginger, Alexander Sell, Olaf Schubert, Bernhard Mayer, Daniele Brida, M Marangoni, Giulio Cerullo, Alfred Leitenstorfer, and Rupert Huber. Single-cycle multiterahertz transients with peak fields above 10 MV/cm. *Optics Letters*, 35(15): 2645–2647, 2010.

[144] JA Fülöp, L Pálfalvi, S Klingebiel, G Almási, F Krausz, S Karsch, and J Hebling. Generation of sub-mj terahertz pulses by optical rectification. *Optics letters*, 37(4): 557–559, 2012.

[145] H Hirori, F Blanchard, KJAPL Tanaka, et al. Single-cycle terahertz pulses with amplitudes exceeding 1 MV/cm generated by optical rectification in $LiNbO_3$. *Applied Physics Letters*, 98(9), 2011.

[146] F Blanchard, X Ropagnol, H Hafez, H Razavipour, M Bolduc, R Morandotti, T Ozaki, and DG Cooke. Effect of extreme pump pulse reshaping on intense terahertz emission in lithium niobate at multimillijoule pump energies. *Optics letters*, 39(15):4333–4336, 2014.

[147] Arno Schneider, Max Neis, Marcel Stillhart, Blanca Ruiz, Rizwan UA Khan, and Peter Günter. Generation of terahertz pulses through optical rectification in organic DAST crystals: theory and experiment. *JOSA B*, 23(9):1822–1835, 2006.

[148] Fabian DJ Brunner, Seung-Heon Lee, O-Pil Kwon, and Thomas Feurer. THz generation by optical rectification of near-infrared laser pulses in the organic nonlinear optical crystal HMQ-TMS. *Optical Materials Express*, 4(8):1586–1592, 2014.

[149] Mojca Jazbinsek, Uros Puc, Andreja Abina, and Aleksander Zidansek. Organic crystals for THz photonics. *Applied Sciences*, 9(5):882, 2019.

[150] Jianming Dai, Jingle Liu, and Xi-Cheng Zhang. Terahertz wave air photonics: terahertz wave generation and detection with laser-induced gas plasma. *IEEE Journal of selected topics in Quantum Electronics*, 17(1):183–190, 2010.

[151] Mark D Thomson, Volker Blank, and Hartmut G Roskos. Terahertz white-light pulses from an air plasma photo-induced by incommensurate two-color optical fields. *Optics Express*, 18(22):23173–23182, 2010.

[152] Benjamin S Williams. Terahertz quantum-cascade lasers. *Nature photonics*, 1(9):517–525, 2007.

[153] M Gensch, L Bittner, A Chesnov, H Delsim-Hashemi, M Drescher, B Faatz, J Feldhaus, U Fruehling, GA Geloni, Ch Gerth, et al. New infrared undulator beamline at FLASH. *Infrared Physics & Technology*, 51(5):423–425, 2008.

[154] Dan Daranciang, John Goodfellow, Matthias Fuchs, Haidan Wen, Shambhu Ghimire, David A Reis, Henrik Loos, Alan S Fisher, and Aaron M Lindenberg. Single-cycle terahertz pulses with> 0.2 v/å field amplitudes via coherent transition radiation. *Applied Physics Letters*, 99(14), 2011.

[155] Ziran Wu, Alan S Fisher, John Goodfellow, Matthias Fuchs, Dan Daranciang, Mark Hogan, Henrik Loos, and Aaron Lindenberg. Intense terahertz pulses from SLAC electron beams using coherent transition radiation. *Review of Scientific Instruments*, 84 (2), 2013.

[156] P Uhd Jepsen, Rune Hylsberg Jacobsen, and SR Keiding. Generation and detection of terahertz pulses from biased semiconductor antennas. *JOSA B*, 13(11):2424–2436, 1996.

[157] Q Wu and X-C Zhang. Ultrafast electro-optic field sensors. *Applied physics letters*, 68 (12):1604–1606, 1996.

[158] Jianming Dai, Xu Xie, and X-C Zhang. Detection of broadband terahertz waves with a laser-induced plasma in gases. *Physical review letters*, 97(10):103903, 2006.

[159] David H Auston. Picosecond optoelectronic switching and gating in silicon. *Applied Physics Letters*, 26(3):101–103, 1975.

[160] H Nemec, A Pashkin, P Kuzel, M Khazan, S Schnull, and I Wilke. Carrier dynamics in low-temperature grown GaAs studied by terahertz emission spectroscopy. *Journal of Applied Physics*, 90(3):1303–1306, 2001.

[161] Enrique Moreno, Mario Fernández Fernández Pantoja, Salvador G Garcia, Amelia Rubio Bretones, and Rafael Gómez Gómez Martin. Time-domain numerical modeling of THz photoconductive antennas. *IEEE Transactions on Terahertz Science and Technology*, 4(4):490–500, 2014.

[162] Stephan Winnerl, Falk Peter, Sven Nitsche, Andre Dreyhaupt, Burkhard Zimmermann, Martin Wagner, Harald Schneider, Manfred Helm, and Klaus Kohler. Generation and detection of THz radiation with scalable antennas based on GaAs substrates with different carrier lifetimes. *IEEE Journal of Selected Topics in Quantum Electronics*, 14(2): 449–457, 2008.

[163] Michael R Stone, Mira Naftaly, Robert E Miles, John R Fletcher, and David Paul Steenson. Electrical and radiation characteristics of semilarge photoconductive terahertz emitters. *IEEE Transactions on Microwave Theory and Techniques*, 52(10):2420–2429, 2004.

[164] PK Benicewicz, JP Roberts, and AJ Taylor. Scaling of terahertz radiation from large-aperture biased photoconductors. *JOSA B*, 11(12):2533–2546, 1994.

[165] AS Weling, BB Hu, NM Froberg, and DH Auston. Generation of tunable narrow-band THz radiation from large aperture photoconducting antennas. *Applied physics letters*, 64(2):137–139, 1994.

[166] Masahiko Tani, Shuji Matsuura, Kiyomi Sakai, and Shin-ichi Nakashima. Emission characteristics of photoconductive antennas based on low-temperature-grown GaAs and semi-insulating GaAs. *Applied optics*, 36(30):7853–7859, 1997.

[167] Shantanu Gupta, MY Frankel, JA Valdmanis, John F Whitaker, Gerard A Mourou, FW Smith, and AR Calawa. Subpicosecond carrier lifetime in GaAs grown by molecular beam epitaxy at low temperatures. *Applied Physics Letters*, 59(25):3276–3278, 1991.

[168] ES Harmon, MR Melloch, JM Woodall, DD Nolte, N Otsuka, and CL Chang. Carrier lifetime versus anneal in low temperature growth GaAs. *Applied physics letters*, 63(16): 2248–2250, 1993.

[169] Masahiko Tani, Kiyomi Sakai, Hajime Abe, Shin-ichi Nakashima, Hiroshi Harima, Masanori Hangyo, Yasunori Tokuda, Kyozo Kanamoto, Yuji Abe, and Noriaki Tsukada. Spectroscopic characterization of low-temperature grown GaAs epitaxial films. *Japanese journal of applied physics*, 33(9R):4807, 1994.

[170] Hitoki Yoneda, Kazutatsu Tokuyama, Ken-ichi Ueda, Hironori Yamamoto, and Kazuhiro Baba. High-power terahertz radiation emitter with a diamond photoconductive switch array. *Applied Optics*, 40(36):6733–6736, 2001.

[171] Shingo Ono, Hidetoshi Murakami, Alex Quema, Gilbert Diwa, Nobuhiko Sarukura, Ryujiro Nagasaka, Yo Ichikawa, Hiraku Ogino, Eriko Ohshima, Akira Yoshikawa, et al. Generation of terahertz radiation using zinc oxide as photoconductive material excited by ultraviolet pulses. *Applied Physics Letters*, 87(26), 2005.

[172] Xavier Ropagnol, Roberto Morandotti, Tsuneyuki Ozaki, and Matt Reid. Toward high-power terahertz emitters using large aperture ZnSe photoconductive antennas. *IEEE Photonics Journal*, 3(2):174–186, 2011.

[173] JF Holzman and AY Elezzabi. Two-photon photoconductive terahertz generation in ZnSe. *Applied physics letters*, 83(14):2967–2969, 2003.

[174] Osamu Imafuji, Brahm Pal Singh, Yutaka Hirose, Yasuyuki Fukushima, and Shinichi Takigawa. High power subterahertz electromagnetic wave radiation from GaN photoconductive switch. *Applied Physics Letters*, 91(7), 2007.

[175] C Winnewisser, P Uhd Jepsen, M Schall, V Schyja, and H Helm. Electro-optic detection of THz radiation in $LiTaO_3$, $LiNbO_3$ and $ZnTe$. *Applied Physics Letters*, 70(23):3069–3071, 1997.

[176] Q Wu and X-C Zhang. 7 terahertz broadband GaP electro-optic sensor. *Applied Physics Letters*, 70(14):1784–1786, 1997.

[177] Robert W Boyd, Alexander L Gaeta, and Enno Giese. Nonlinear optics. pages 1097–1110. Springer, 2008.

[178] Nick CJ van der Valk, Tom Wenckebach, and Paul CM Planken. Full mathematical description of electro-optic detection in optically isotropic crystals. *JOSA B*, 21(3): 622–631, 2004.

[179] Sang-Gyu Park, Michael R Melloch, and Andrew M Weiner. Analysis of terahertz waveforms measured by photoconductive and electrooptic sampling. *IEEE Journal of Quantum Electronics*, 35(5):810–819, 1999.

[180] David H Auston and KP Cheung. Coherent time-domain far-infrared spectroscopy. *JOSA B*, 2(4):606–612, 1985.

[181] Bahaa EA Saleh and Malvin Carl Teich. Fundamentals of photonics. 2019.

[182] Ajay Nahata, Aniruddha S Weling, and Tony F Heinz. A wideband coherent terahertz spectroscopy system using optical rectification and electro-optic sampling. *Applied physics letters*, 69(16):2321–2323, 1996.

[183] Rupert Huber, A Brodschelm, F Tauser, and A Leitenstorfer. Generation and field-resolved detection of femtosecond electromagnetic pulses tunable up to 41 THz. *Applied Physics Letters*, 76(22):3191–3193, 2000.

[184] Jinjun Liu, Hansjürg Schmutz, and Frédéric Merkt. Generation of widely tunable fourier-transform-limited terahertz pulses using narrowband near-infrared laser radiation. *Journal of Molecular Spectroscopy*, 256(1):111–118, 2009.

[185] J Hebling, AG Stepanov, G Almási, B Bartal, and J Kuhl. Tunable THz pulse generation by optical rectification of ultrashort laser pulses with tilted pulse fronts. *Applied Physics B*, 78:593–599, 2004.

[186] Matthias C Hoffmann and József András Fülöp. Intense ultrashort terahertz pulses: generation and applications. *Journal of Physics D: Applied Physics*, 44(8):083001, 2011.

[187] János Hebling, Ka-Lo Yeh, Matthias C Hoffmann, Balázs Bartal, and Keith A Nelson. Generation of high-power terahertz pulses by tilted-pulse-front excitation and their application possibilities. *JOSA B*, 25(7):B6–B19, 2008.

[188] Koustuban Ravi, Wenqian Ronny Huang, Sergio Carbajo, Emilio A Nanni, Damian N Schimpf, Erich P Ippen, and Franz X Kärtner. Theory of terahertz generation by optical rectification using tilted-pulse-fronts. *Optics express*, 23(4):5253–5276, 2015.

[189] Janos Hebling, Gabor Almasi, Ida Z Kozma, and Jürgen Kuhl. Velocity matching by pulse front tilting for large-area THz-pulse generation. *Optics express*, 10(21):1161–1166, 2002.

[190] David H Auston, KP Cheung, JA Valdmanis, and DA Kleinman. Cherenkov radiation from femtosecond optical pulses in electro-optic media. *Physical Review Letters*, 53(16): 1555, 1984.

[191] L Pálfalvi, J Hebling, J Kuhl, A Peter, and K Polgár. Temperature dependence of the absorption and refraction of Mg-doped congruent and stoichiometric $LiNbO_3$ in the THz range. *Journal of applied physics*, 97(12), 2005.

[192] JA Fülöp, L Pálfalvi, G Almási, and J Hebling. Design of high-energy terahertz sources based on optical rectification. *Optics express*, 18(12):12311–12327, 2010.

[193] François Blanchard, Gargi Sharma, Luca Razzari, Xavier Ropagnol, Heidi-Christina Bandulet, François Vidal, Roberto Morandotti, Jean-Claude Kieffer, Tsuneyuki Ozaki, Henry Tiedje, et al. Generation of intense terahertz radiation via optical methods. *IEEE Journal of Selected Topics in Quantum Electronics*, 17(1):5–16, 2010.

[194] József A Fülöp, Zoltán Ollmann, Cs Lombosi, Christoph Skrobol, Sandro Klingebiel, László Pálfalvi, Ferenc Krausz, Stefan Karsch, and JJOE Hebling. Efficient generation of THz pulses with 0.4 mJ energy. *Optics express*, 22(17):20155–20163, 2014.

[195] Shu-Wei Huang, Eduardo Granados, Wenqian Ronny Huang, Kyung-Han Hong, Luis E Zapata, and Franz X Kärtner. High conversion efficiency, high energy terahertz pulses by optical rectification in cryogenically cooled lithium niobate. *Optics letters*, 38 (5):796–798, 2013.

[196] F Blanchard, BE Schmidt, X Ropagnol, N Thiré, T Ozaki, R Morandotti, DG Cooke, and F Légaré. Terahertz pulse generation from bulk GaAs by a tilted-pulse-front excitation at 1.8 μm. *Applied Physics Letters*, 105(24), 2014.

[197] Cho Yen Ho and Richard Erwin Taylor. Thermal expansion of solids. 4, 1998.

[198] Xiaoshu Chen, Shan He, Zhen Shen, Fu Li Zhao, KY Xu, Gang Wang, Reng Wang, and Ning Dai. Influence of nonlinear effects in ZnTe on generation and detection of terahertz waves. *Journal of applied physics*, 105(2), 2009.

[199] SA Ku, CM Tu, W-C Chu, Chih-Wei Luo, Kaung-Hsiung Wu, A Yabushita, CC Chi, and T Kobayashi. Saturation of the free carrier absorption in ZnTe crystals. *Optics express*, 21(12):13930–13937, 2013.

[200] Marion Cornet, Jérôme Degert, Emmanuel Abraham, and Eric Freysz. Terahertz-field-induced second harmonic generation through pockels effect in zinc telluride crystal. *Optics letters*, 39(20):5921–5924, 2014.

[201] Pernille Klarskov and Peter Uhd Jepsen. THz induced nonlinear absorption in ZnTe. pages 1–1. IEEE, 2015.

[202] Joel Yuen-Zhou and Vinod M Menon. Polariton chemistry: Thinking inside the (photon) box. *Proceedings of the National Academy of Sciences*, 116(12):5214–5216, 2019.

[203] Päivi Törmä and William L Barnes. Strong coupling between surface plasmon polaritons and emitters: a review. *Reports on Progress in Physics*, 78(1):013901, 2014.

[204] Anoop Thomas, Jino George, Atef Shalabney, Marian Dryzhakov, Sreejith J Varma, Joseph Moran, Thibault Chervy, Xiaolan Zhong, Eloïse Devaux, Cyriaque Genet, et al. Ground-state chemical reactivity under vibrational coupling to the vacuum electromagnetic field. *Angewandte Chemie*, 128(38):11634–11638, 2016.

[205] E Orgiu, J George, JA Hutchison, E Devaux, JF Dayen, B Doudin, F Stellacci, C Genet, J Schachenmayer, Claudiu Genes, et al. Conductivity in organic semiconductors hybridized with the vacuum field. *Nature Materials*, 14(11):1123–1129, 2015.

[206] Atef Shalabney, Jino George, J a Hutchison, Guido Pupillo, Cyriaque Genet, and Thomas W Ebbesen. Coherent coupling of molecular resonators with a microcavity mode. *Nature communications*, 6(1):5981, 2015.

[207] Thibault Chervy, Jialiang Xu, Yulong Duan, Chunliang Wang, Loïc Mager, Maurice Frerejean, Joris AW Munninghoff, Paul Tinnemans, James A Hutchison, Cyriaque Genet, et al. High-efficiency second-harmonic generation from hybrid light-matter states. *Nano letters*, 16(12):7352–7356, 2016.

[208] Fábio Barachati, Janos Simon, Yulia A Getmanenko, Stephen Barlow, Seth R Marder, and Stéphane Kéna-Cohen. Tunable third-harmonic generation from polaritons in the ultrastrong coupling regime. *Acs Photonics*, 5(1):119–125, 2018.

[209] A Damascelli, D Van der Marel, Fulvio Parmigiani, G Dhalenne, and A Revcolevschi. Infrared reflectivity of pure and doped $CuGeO_3$. *Physica B: Condensed Matter*, 244: 114–120, 1998.

[210] Masashi Hase, Ichiro Terasaki, and Kunimitsu Uchinokura. Observation of the spin-peierls transition in linear Cu 2+(spin-1/2) chains in an inorganic compound $CuGeO_3$. *Physical Review Letters*, 70(23):3651, 1993.

[211] M Nishi, O Fujita, and J Akimitsu. Neutron-scattering study on the spin-peierls transition in a quasi-one-dimensional magnet $CuGeO_3$. *Physical Review B*, 50(9):6508, 1994.

[212] JP Pouget, LP Regnault, M Ain, B Hennion, JP Renard, P Veillet, G Dhalenne, and A Revcolevschi. Structural evidence for a spin peierls ground state in the quasi-one-dimensional compound $CuGeO_3$. *Physical review letters*, 72(25):4037, 1994.

[213] M Arai, M Fujita, M Motokawa, Jun Akimitsu, and SM Bennington. Quantum spin excitations in the spin-peierls system $CuGeO_3$. *Physical review letters*, 77(17):3649, 1996.

[214] A Damascelli, D Van der Marel, Fulvio Parmigiani, G Dhalenne, and A Revcolevschi. Infrared signatures of the spin-peierls transition in $CuGeO_3$. *Physical Review B*, 56(18): R11373, 1997.

[215] DS Dovzhenko, SV Ryabchuk, Yu P Rakovich, and IR Nabiev. Light–matter interaction in the strong coupling regime: configurations, conditions, and applications. *Nanoscale*, 10(8):3589–3605, 2018.

[216] Iacopo Carusotto and Cristiano Ciuti. Quantum fluids of light. *Reviews of Modern Physics*, 85(1):299, 2013.

[217] A Damascelli, D van der Marel, G Dhalenne, and A Revcolevschi. Optical spectroscopy of pure and doped $CuGeO_3$. *Physical Review B*, 61(18):12063, 2000.

[218] Masaro Yoshida, Ryuji Suzuki, Yijin Zhang, Masaki Nakano, and Yoshihiro Iwasa. Memristive phase switching in two-dimensional $1T - TaS_2$ crystals. *Science advances*, 1(9):e1500606, 2015.

[219] JA Wilson, FJ Di Salvo, and S Mahajan. Charge-density waves in metallic, layered, transition-metal dichalcogenides. *Physical review letters*, 32(16):882, 1974.

[220] George Grüner. The dynamics of charge-density waves. *Reviews of modern physics*, 60 (4):1129, 1988.

[221] George Gruner. Density waves in solids. 2018.

[222] Rudolf Ernst Peierls. Quantum theory of solids. 1996.

[223] Masaro Yoshida, Yijin Zhang, Jianting Ye, Ryuji Suzuki, Yasuhiko Imai, Shigeru Kimura, Akihiko Fujiwara, and Yoshihiro Iwasa. Controlling charge-density-wave states in nano-thick crystals of $1T - TaS_2$. *Scientific reports*, 4(1):7302, 2014.

[224] P Fazekas and E Tosatti. Electrical, structural and magnetic properties of pure and doped $1T - TaS_2$. *Philosophical Magazine B*, 39(3):229–244, 1979.

[225] Florian Clerc, Corsin Battaglia, M Bovet, Laurent Despont, Claude Monney, Hervé Cercellier, MG Garnier, Philipp Aebi, Helmuth Berger, and László Forró. Lattice-distortion-enhanced electron-phonon coupling and fermi surface nesting in $1T - TaS_2$. *Physical Review B*, 74(15):155114, 2006.

[226] AH Thompson, RF Gamble, and JF Revelli. Transitions between semiconducting and metallic phases in $1 - TTaS_2$. *Solid State Communications*, 9(13):981–985, 1971.

[227] Jl A Wilson, FJ Di Salvo, and S Mahajan. Charge-density waves and superlattices in the metallic layered transition metal dichalcogenides. *Advances in Physics*, 24(2): 117–201, 1975.

[228] S Sugai, K Murase, S Uchida, and S Tanaka. Comparison of the soft modes in tantalum dichalcogenides. *Physica B+ C*, 105(1-3):405–409, 1981.

[229] RE Thomson, B Burk, A Zettl, and John Clarke. Scanning tunneling microscopy of the charge-density-wave structure in $1T - TaS_2$. *Physical Review B*, 49(24):16899, 1994.

[230] Th Pillo, J Hayoz, H Berger, M Grioni, Louis Schlapbach, and Philipp Aebi. Remnant fermi surface in the presence of an underlying instability in layered $1T - TaS_2$. *Physical review letters*, 83(17):3494, 1999.

[231] NV Smith, SD Kevan, and FJ DiSalvo. Band structures of the layer compounds $1T-TaS_2$ and $2H-TaSe_2$ in the presence of commensurate charge-density waves. *Journal of Physics C: Solid State Physics*, 18(16):3175, 1985.

[232] K Rossnagel and NV Smith. Spin-orbit coupling in the band structure of reconstructed $1T-TaS_2$. *Physical Review B*, 73(7):073106, 2006.

[233] B Dardel, M Grioni, D Malterre, P Weibel, Y Baer, and F Lévy. Spectroscopic signatures of phase transitions in a charge-density-wave system: $1T-TaS_2$. *Physical Review B*, 46(12):7407, 1992.

[234] B Dardel, M Grioni, D Malterre, P Weibel, Y Baer, and F Lévy. Temperature-dependent pseudogap and electron localization in $1T-TaS_2$. *Physical Review B*, 45(3):1462, 1992.

[235] Ju-Jin Kim, W Yamaguchi, T Hasegawa, and K Kitazawa. Observation of mott localization gap using low temperature scanning tunneling spectroscopy in commensurate $1T-TaS_2$. *Physical review letters*, 73(15):2103, 1994.

[236] Nicky Dean, Jesse C Petersen, Daniele Fausti, Ra'anan I Tobey, Stefan Kaiser, LV Gasparov, Helmuth Berger, and Andrea Cavalleri. Polaronic conductivity in the photoinduced phase of $1T-TaS_2$. *Physical review letters*, 106(1):016401, 2011.

[237] LV Gasparov, KG Brown, AC Wint, DB Tanner, H Berger, G Margaritondo, R Gaál, and L Forró. Phonon anomaly at the charge ordering transition in $1T-TaS_2$. *Physical Review B*, 66(9):094301, 2002.

[238] YD Wang, WL Yao, ZM Xin, TT Han, ZG Wang, L Chen, C Cai, Yuan Li, and Y Zhang. Band insulator to mott insulator transition in $1T-TaS_2$. *Nature communications*, 11(1): 4215, 2020.

[239] Giacomo Jarc, Shahla Yasmin Mathengattil, Angela Montanaro, Enrico Maria Rigoni, Stephan Winnerl, Simone Dal Zilio, Dragan Mihailovic, and Daniele Fausti. Multimode vibrational coupling across the metal-to-insulator transition in 1T-TaS_2. May 2024. Unpublished, manuscript in preparation.

[240] Haiyan Zheng, Yating Bai, Qiang Zhang, and Shaoding Liu. Multi-mode strong coupling in Fabry-Pérot cavity- WS_2 photonic crystal hybrid structures. *Optics Express*, 31(15):24976–24987, 2023.

[241] Khalil As' ham, Ibrahim Al-Ani, Lujun Huang, Andrey E Miroshnichenko, and Haroldo T Hattori. Boosting strong coupling in a hybrid WSe_2 monolayer–anapole–plasmon system. *ACS Photonics*, 8(2):489–496, 2021.

[242] Yi-Pu Wang and Can-Ming Hu. Dissipative couplings in cavity magnonics. *Journal of Applied Physics*, 127(13), 2020.

[243] Alexey V Kavokin, Jeremy J Baumberg, Guillaume Malpuech, and Fabrice P Laussy. Microcavities. 21, 2017.

[244] Johannes Flick, Michael Ruggenthaler, Heiko Appel, and Angel Rubio. Atoms and molecules in cavities, from weak to strong coupling in quantum-electrodynamics (QED) chemistry. *Proceedings of the National Academy of Sciences*, 114(12):3026–3034, 2017.

[245] MM Glazov, EL Ivchenko, AN Poddubny, and G Khitrova. Purcell factor in small metallic cavities. *Physics of the Solid State*, 53:1753–1760, 2011.

[246] Dongxing Zhao, Rui EF Silva, Clàudia Climent, Johannes Feist, Antonio I Fernández-Domínguez, and Francisco J García-Vidal. Impact of vibrational modes in the plasmonic purcell effect of organic molecules. *ACS photonics*, 7(12):3369–3375, 2020.

[247] Michael Knap, Mehrtash Babadi, Gil Refael, Ivar Martin, and Eugene Demler. Dynamical Cooper pairing in nonequilibrium electron-phonon systems. *Physical Review B*, 94 (21):214504, 2016.

[248] Dongbin Shin, Nicolas Tancogne-Dejean, Jin Zhang, Mahmut Sait Okyay, Angel Rubio, and Noejung Park. Identification of the mott insulating charge density wave state in $1T - TaS_2$. *Physical Review Letters*, 126(19):196406, 2021.

[249] Michael Kozina, Michael Fechner, Premysl Marsik, Tim van Driel, James M Glownia, Christian Bernhard, Milan Radovic, Diling Zhu, Stefano Bonetti, Urs Staub, et al. Terahertz-driven phonon upconversion in $SrTiO_3$. *Nature Physics*, 15(4):387–392, 2019.

[250] Elisabeth M Bothschafter, Alexander Paarmann, Eeuwe S Zijlstra, Nicholas Karpowicz, Martin E Garcia, Reinhard Kienberger, and Ralph Ernstorfer. Ultrafast evolution of the excited-state potential energy surface of TiO_2 single crystals induced by carrier cooling. *Physical Review Letters*, 110(6):067402, 2013.

[251] Hannes Hübener, Michael A Sentef, Umberto De Giovannini, Alexander F Kemper, and Angel Rubio. Creating stable Floquet–Weyl semimetals by laser-driving of 3D Dirac materials. *Nature communications*, 8(1):13940, 2017.

[252] Netanel H Lindner, Gil Refael, and Victor Galitski. Floquet topological insulator in semiconductor quantum wells. *Nature Physics*, 7(6):490–495, 2011.

[253] Daniele Fausti, RI Tobey, Nicky Dean, Stefan Kaiser, A Dienst, Matthias C Hoffmann, S Pyon, T Takayama, H Takagi, and Andrea Cavalleri. Light-induced superconductivity in a stripe-ordered cuprate. *science*, 331(6014):189–191, 2011.

[254] Matteo Mitrano, Alice Cantaluppi, Daniele Nicoletti, Stefan Kaiser, A Perucchi, Stefano Lupi, P Di Pietro, Daniele Pontiroli, Mauro Riccò, Stephen R Clark, et al. Possible light-induced superconductivity in K_3C_{60} at high temperature. *Nature*, 530(7591): 461–464, 2016.

[255] M Buzzi, D Nicoletti, M Fechner, N Tancogne-Dejean, MA Sentef, A Georges, T Biesner, E Uykur, M Dressel, A Henderson, et al. Photomolecular high-temperature superconductivity. *Physical Review X*, 10(3):031028, 2020.

[256] Chirag Vaswani, L-L Wang, Dinusha Herath Mudiyanselage, Q Li, PM Lozano, GD Gu, Di Cheng, Boqun Song, Liang Luo, Richard HJ Kim, et al. Light-driven raman coherence as a nonthermal route to ultrafast topology switching in a Dirac semimetal. *Physical Review X*, 10(2):021013, 2020.

[257] Edbert J Sie, Clara M Nyby, CD Pemmaraju, Su Ji Park, Xiaozhe Shen, Jie Yang, Matthias C Hoffmann, BK Ofori-Okai, Renkai Li, Alexander H Reid, et al. An ultrafast symmetry switch in a Weyl semimetal. *Nature*, 565(7737):61–66, 2019.

[258] Ankit S Disa, Michael Fechner, Tobia F Nova, Biaolong Liu, Michael Först, Dharmalingam Prabhakaran, Paolo G Radaelli, and Andrea Cavalleri. Polarizing an antiferromagnet by optical engineering of the crystal field. *Nature Physics*, 16(9):937–941, 2020.

[259] Dongbin Shin, Hannes Hübener, Umberto De Giovannini, Hosub Jin, Angel Rubio, and Noejung Park. Phonon-driven spin-Floquet magneto-valleytronics in MoS_2. *Nature communications*, 9(1):638, 2018.

[260] Julian Maklar, Jit Sarkar, Shuo Dong, Yaroslav A Gerasimenko, Tommaso Pincelli, Samuel Beaulieu, Patrick S Kirchmann, Jonathan A Sobota, Shuolong Yang, Dominik Leuenberger, et al. Coherent light control of a metastable hidden state. *Science Advances*, 9(47):eadi4661, 2023.

[261] Sheikh Rubaiat Ul Haque, Marios H Michael, Junbo Zhu, Yuan Zhang, Lukas Windgätter, Simone Latini, Joshua P Wakefield, Gu-Feng Zhang, Jingdi Zhang, Angel Rubio, et al. Terahertz parametric amplification as a reporter of exciton condensate dynamics. *Nature Materials*, pages 1–7, 2024.

[262] Frank Schlawin, Dante M Kennes, and Michael A Sentef. Cavity quantum materials. *Applied Physics Reviews*, 9(1), 2022.

[263] Alessio Chiocchetta, Dominik Kiese, Carl Philipp Zelle, Francesco Piazza, and Sebastian Diehl. Cavity-induced quantum spin liquids. *Nature Communications*, 12(1):5901, 2021.

[264] LV Abdurakhimov, S Khan, NA Panjwani, JD Breeze, M Mochizuki, S Seki, Y Tokura, JJL Morton, and H Kurebayashi. Magnon-photon coupling in the noncollinear magnetic insulator Cu_2OSeO_3. *Physical Review B*, 99(14):140401, 2019.

[265] Emil Viñas Boström, Adithya Sriram, Martin Claassen, and Angel Rubio. Controlling the magnetic state of the proximate quantum spin liquid α-$RuCl_3$ with an optical cavity. *npj Computational Materials*, 9(1):202, 2023.

[266] Jonathan B Curtis, Andrey Grankin, Nicholas R Poniatowski, Victor M Galitski, Prineha Narang, and Eugene Demler. Cavity magnon-polaritons in cuprate parent compounds. *Physical Review Research*, 4(1):013101, 2022.

[267] Michela F Picardi, Kartika N Nimje, and Georgia T Papadakis. Dynamic modulation of thermal emission—a tutorial. *Journal of Applied Physics*, 133(11), 2023.

[268] Yongchang Ma, Yanhui Hou, Cuimin Lu, Lijun Li, and Cedomir Petrovic. Possible origin of nonlinear conductivity and large dielectric constant in the commensurate charge-density-wave phase of 1 t- tas 2. *Physical Review B*, 97(19):195117, 2018.

[269] Yongchang Ma, Dong Wu, and Zequn Wang. The evidence of stacking disorder from dielectric response along the c-axis in the commensurate cdw phase in bulk $1T - TaS_2$. *Solid State Communications*, 316:113946, 2020.

[270] DRP Guy, AM Ghorayeb, SC Bayliss, and RH Friend. High pressure investigation of the CDW phase diagram of $1T - TaS_2$. pages 80–83. Springer, 2005.

[271] I Fedorov, V Železn, J Petzelt, V Trepakov, M Jelínek, V Trtík, M Čer&ňansk, and V Studnička. Far-infrared spectroscopy of a $SrTiO_3$ thin film. *Ferroelectrics*, 208(1): 413–427, 1998.

[272] Gene H Haertling. Ferroelectric ceramics: history and technology. *Journal of the American Ceramic Society*, 82(4):797–818, 1999.

[273] Wenjing Jie and Jianhua Hao. Graphene-based hybrid structures combined with functional materials of ferroelectrics and semiconductors. *Nanoscale*, 6(12):6346–6362, 2014.

[274] Alexander I McIntosh, Bin Yang, Stephen M Goldup, Michael Watkinson, and Robert S Donnan. Terahertz spectroscopy: a powerful new tool for the chemical sciences? *Chemical Society Reviews*, 41(6):2072–2082, 2012.

[275] T Sakudo and H Unoki. Dielectric properties of $SrTiO_3$ at low temperatures. *Physical review letters*, 26(14):851, 1971.

[276] A Yamanaka, M Kataoka, Y Inaba, K Inoue, B Hehlen, and E Courtens. Evidence for competing orderings in strontium titanate from hyper-raman scattering spectroscopy. *Europhysics letters*, 50(5):688, 2000.

[277] Ulrich Aschauer and Nicola A Spaldin. Competition and cooperation between antiferrodistortive and ferroelectric instabilities in the model perovskite $SrTiO_3$. *Journal of Physics: Condensed Matter*, 26(12):122203, 2014.

[278] GA Komandin, VM Mukhortov, OE Porodinkov, and IE Spektor. Dielectric response of $(Ba, Sr)TiO_3$ thin films in a terahertz and ir ranges. *Physics of the Solid State*, 55: 288–292, 2013.

[279] H Vogt. Refined treatment of the model of linearly coupled anharmonic oscillators and its application to the temperature dependence of the zone-center soft-mode frequencies of $KTaO_3$ and $SrTiO_3$. *Physical Review B*, 51(13):8046, 1995.

[280] Dongbin Shin, Simone Latini, Christian Schäfer, Shunsuke A Sato, Umberto De Giovannini, Hannes Hübener, and Angel Rubio. Quantum paraelectric phase of $SrTiO_3$ from first principles. *Physical Review B*, 104(6):L060103, 2021.

[281] I Katayama, H Aoki, J Takeda, H Shimosato, M Ashida, R Kinjo, I Kawayama, M Tonouchi, M Nagai, and K Tanaka. Ferroelectric soft mode in a $SrTiO_3$ thin film impulsively driven to the anharmonic regime using intense picosecond terahertz pulses. *Physical review letters*, 108(9):097401, 2012.

[282] YL Li, S Choudhury, JH Haeni, MD Biegalski, A Vasudevarao, A Sharan, HZ Ma, J Levy, Venkatraman Gopalan, S Trolier-McKinstry, et al. Phase transitions and domain structures in strained pseudocubic (100) $SrTiO_3$ thin films. *Physical Review B*, 73(18): 184112, 2006.

[283] Jiaguang Han, Fan Wan, Zhiyuan Zhu, and Weili Zhang. Dielectric response of soft mode in ferroelectric $SrTiO_3$. *Applied Physics Letters*, 90(3), 2007.

[284] RE Kroon. The classical oscillator model and dielectric constants extracted from infrared reflectivity measurements. *Infrared physics & technology*, 51(1):31–43, 2007.

[285] Lionel Duvillaret, Frederic Garet, and J-L Coutaz. A reliable method for extraction of material parameters in terahertz time-domain spectroscopy. *IEEE Journal of selected topics in quantum electronics*, 2(3):739–746, 1996.

[286] Tatsuya Mori, Hikaru Igawa, and Seiji Kojima. Progress of ultrafast terahertz time-domain spectroscopy: Raman inactive soft mode in quantum paraelectric $SrTiO_3$. volume 54, page 012006. IOP Publishing, 2014.

[287] Minko Balkanski. Optical properties of solids. *(No Title)*, 1980.

[288] William L Barnes, Simon AR Horsley, and Willem L Vos. Classical antennas, quantum emitters, and densities of optical states. *Journal of Optics*, 22(7):073501, 2020.

[289] Elena Mavrona, Shima Rajabali, Felice Appugliese, Johan Andberger, Mattias Beck, Giacomo Scalari, and Jerome Faist. THz ultrastrong coupling in an engineered Fabry-Perot cavity. *ACS Photonics*, 8(9):2692–2698, 2021.

List of figures

LIST OF TABLES

PUBLICATIONS

- **S. Y. Mathengattil** et al. *Cavity enhanced nonlinear responses in para electric* $SrTiO_3$. Article in preparation (May 2024).
- G. Jarc, **S. Y. Mathengattil**, F. Giusti, M. Barnaba, S. Dal Zilio, S. Winnerl, A. Singh, A. Montanaro, F. Glerean, E. M. Rigoni, S. Dal Zilio, S. Winnerl, and D. Fausti. *Tunable cryogenic terahertz cavity for strong light-matter coupling in complex materials*. Review of Scientific Instruments, 93, 033102 (2022).
- G. Jarc, **S. Y. Mathengattil**, A. Montanaro, F. Giusti, E. M. Rigoni, F. Fassioi, S. Winnerl, S. Dal Zilio, D. Mihailovic, P. Prelovsek, M. Eckstein, and D. Fausti. *Cavity mediated thermal control of metal-to-insulator transition in 1T-*TaS_2. Nature volume 622, pages487–492 (2023).
- A. Montanaro, F. Giusti, M. Zanforgnini, D. Di Pietro, F. Glerean, G. Jarc, E. M. Rigoni, **S. Y. Mathengattil**, D. Varsano, M. Ronchi, A. Perucchi, E. Molinari, and D. Fausti. *Anomalous non-equilibrium response in black phosphorus to sub-gap mid-infrared excitation*. Nature Communications 13, 2667 (2022).
- G. Jarc, **S. Y. Mathengattil**, A. Montanaro, E. M. Rigoni, S. Winnerl, S. Dal Zilio, D. Mihailovic, and D. Fausti. *Multimode vibrational coupling across the metal-to-insulator transition in 1T-*TaS_2. Article in preparation (May 2024).

ACKNOWLEDGEMENTS

As I reach the end of my PhD journey, I am filled with a deep sense of gratitude and accomplishment. This journey, marked by rigorous challenges and tireless effort, has been profoundly enlightening.

First and foremost, I would like to express my deepest gratitude to my supervisor, Daniele. Your constant motivation and enthusiasm have been beneficial in shaping my PhD journey. Beyond academic guidance, you have been a source of solace and encouragement during some of the most challenging times. Your guidance and unwavering support have been invaluable, and I am profoundly grateful for the opportunities you have provided me.

I would not have completed my Ph.D. without the people who supported me in the q4q laboratory. Firstly, I would like to extend my deepest gratitude to Giacomo for his exceptional support and collaboration throughout my work in the lab. His expertise and willingness to share his knowledge were instrumental in overcoming the challenges we faced in the lab. Together, we navigated numerous difficulties and persevered through the complexities of the measurements with the cavity.

I would also like to extend my heartfelt thanks to Angela, who joined me in the lab during the final days of this project. Her patience, expertise and the clarity with which she explained complex concepts were incredibly valuable. I truly enjoyed working with Angela, and her contributions were essential to the successful completion of this work.

I would also like to thank Enrico who has been a friend and peer support throughout my PhD journey. Being in the same year, we shared many of the same deadlines and pressures of the PhD. As a Triestino, he continuously helped with various aspects of life in Trieste, making living there much easier.

Additionally, I am grateful to Francesca and Filippo who were in the lab during the initial days of my PhD. Their guidance and support as senior members were valuable in helping me settle in and understand the lab environment. I would like to thank Antonio for his excellent collaboration on the theoretical aspects of the project in its final days.

My biggest thanks belongs to the people of Elettra, who has provided help and support during my PhD. I am especially thankful to Rudi and Gabriele from the electronics group for their extensive assistance and expert advice, which were crucial in the experiments.

Next, I want to express my appreciation to Manil, Ankur, Yukti, Irshad, Kirthana and especially my housemate Smriti for remaining interested and supportive, and for giving me many, many things to enjoy outside of the PhD. Your friendship and encouragement have been a source of strength and comfort throughout this journey, making the experience more memorable.

I express my thanks to my friends Anjaly, Sid, Jithu, Appu, Anoop, Aji, Joyal, Sreehari and Hari for their love, support and inspiration. Despite the miles between us, your encouragement and understanding have been a source of great comfort and inspiration in the difficult times.

I want to extend my deepest gratitude to my parents, whose unwavering love and pride have been a constant source of strength and motivation throughout this journey. Your belief in me and your encouragement during the most challenging times have been incredibly comforting and inspiring. I also want to thank my brother and sister for their

support and companionship. I extend my thanks to all the family members for making every accomplishment even more meaningful through their support.

Thank you all for making this journey an unforgettable and rewarding experience.

With deepest gratitude,
Shahla